ABSTRACT

Title of Dissertation: ANALYSIS OF RELIABILITY AND CONDUCTION MECHANISMS IN EMBEDDED PLANAR CAPACITORS

Mohammed Aftab Alam,
Doctor of Philosophy, 2012

Dissertation directed by: Professor Michael G. Pecht,
Department of Mechanical Engineering

An embedded planar capacitor is a thin laminate embedded in a multilayered printed wiring board (PWB) that functions both as a power-ground plane and as a parallel plate capacitor. The capacitor laminate consists of a dielectric material (epoxy-$BaTiO_3$ composite dielectric is widely used) sandwiched between two Cu layers. These capacitors have gained importance with an increase in the operating frequency and a decrease in the supply voltage in electronic circuits since it can lead to PWB miniaturization. Further, the use of embedded planar capacitor leads to better electrical performance of the PWB. Although embedded planar capacitors have various advantages there are some issues such as lack of reliability information and a high leakage current in the epoxy-$BaTiO_3$ composite dielectric. This dissertation aims in investigating these issues that needs to be investigated for wide scale commercialization of these capacitors.

The reliability of embedded planar capacitors is critical since these capacitors are not reworkable and its failure can lead to PWB failure. In this work the reliability of an embedded planar capacitor (with epoxy-$BaTiO_3$ composite dielectric) is investigated under environmental stress conditions in the presence of an applied bias. Temperature-humidity-bias (THB) tests and highly accelerated life tests were performed at multiple stress levels to investigate the reliability under these conditions. The failure modes and mechanisms during these tests are investigated. Further, during highly accelerated life testing the life time is also modeled using the Prokopowicz model and regression of the in-situ capacitor data.

The loading of $BaTiO_3$ in the epoxy-$BaTiO_3$ composite dielectric should be as high as possible (until the theoretical maximum packing density is achieved) to maximize the effective dielectric constant of the composite. But as the loading of $BaTiO_3$ in the composite dielectric increases, the undesirable leakage current also increases. The mechanism of current conduction in this composite dielectric is investigated in this work. The effect of various factors such as $BaTiO_3$ loading, $BaTiO_3$ particle diameter, temperature, and voltage on the resulting leakage current has been modeled. Measurements of leakage current were performed on embedded capacitors with varying $BaTiO_3$ loading and varying particle diameters over a range of temperature and voltage. The consistence of the leakage current data with standard conduction models is compared to investigate the conduction mechanism.

# ANALYSIS OF RELIABILITY AND CONDUCTION MECHANISMS IN EMBEDDED PLANAR CAPACITORS

by

Mohammed Aftab Alam

Dissertation submitted to the Faculty of the Graduate School of the
University of Maryland, College Park in partial fulfillment
of the requirements for the degree of
Doctor of Philosophy
2012

Advisory Committee:
Professor Michael Pecht (Chair/Advisor)
Dr. Michael Azarian (Co-chair/advisor)
Professor Abhijit Dasgupta
Professor Peter Sandborn
Professor John Melngailis

*this thesis is dedicated to my parents*

# ACKNOWLEDGMENTS

With a deep sense of gratitude, I wish to express my sincere thanks to my advisor, Prof. Michael Pecht, for allowing me to work on this interesting topic. He has been a constant source of inspiration during my stay in the graduate school. I thank Dr. Michael Azarian, my co-advisor, for his guidance, motivation, and research inputs throughout the course of this research. I earnestly thank my committee members, Prof. Peter Sandborn, Prof. Abhijit Dasgupta, and Prof. John Melngailis for their valuable time and inputs.

I wish to express my sincere gratitude to the CALCE research faculty for providing me feedback, notably Dr. Michael Osterman, Dr. Diganta Das, and Bhanu Sood. I am thankful to Mark Zimmerman at CALCE for his help in improving my writing skills and for reviewing my technical papers. I gratefully acknowledge the financial support of the CALCE EPS Consortium for my research. I am thankful to Joel Peiffer from 3M Electronic Solutions Division for his help throughout this project.

I thank all my research group members at CALCE including Anshul, Elviz, Hyunseok, Nishad, Ranjith, Sachin, Sandeep, Thomas, Vikram, and Xiaofei for creating a motivating work environment, for their constant inputs on my research and above all, for their friendship. I thank Bikash, Chandradeep, Debo, Gaurav, Rishi, Rubyca, Suvajyoti, Sapna, and Snehanshu whose friendship and presence in life during graduate school provided me with a familiar environment away from home and helped me grow personally and professionally. Last but not least, I thank all the members of the Mechanical Engineering department and the University of Maryland who create a wonderful environment to be a part of.

## Table of contents

Table of contents ..... iv
Index of figures ..... vi
1. Introduction ..... 1
1.1 Background ..... 1
1.2 Motivation ..... 5
1.2.1 Temperature-humidity-bias tests ..... 6
1.2.2 Lifetime modeling ..... 7
1.2.3 Conduction mechanisms ..... 8
1.3 Dissertation objectives ..... 9
2. Literature Review ..... 10
2.1 Reliability under elevated temperature and humid conditions ..... 10
2.2 Reliability under elevated temperature and voltage conditions ..... 11
2.3 Conduction mechanisms ..... 14
2.4 Manufacturing of capacitors with composite dielectric ..... 17
2.4.1 Preparation of the dielectric paste ..... 17
2.4.2 Manufacturing of the capacitor ..... 20
3. Test vehicle ..... 22
3.1 Test vehicle with multiple embedded capacitors ..... 22
3.2 Test vehicle with a single embedded capacitor ..... 24
4. Electrical characterization of the test vehicle ..... 33
4.1 Test vehicle with multiple embedded capacitors ..... 33
4.2 Test vehicle with a single embedded capacitor ..... 34
5. Temperature-humidity-bias (THB) test ..... 39
5.1 Experimental setup ..... 39
5.2 Observations during THB test ..... 42
5.2.1 Behavior of capacitance ..... 42
5.2.2 Behavior of dissipation factor ..... 43
5.2.3 Behavior of insulation resistance ..... 45
5.3 Observations during baking the board ..... 47
5.4 Hypothesis of insulation resistance failures ..... 50
5.5 Modeling the drift in electrical parameters ..... 52
5.5.1 Assumptions and boundary conditions (B.C) ..... 53
5.5.2 Methodology ..... 55
5.6 Verification of the methodology ..... 59
6. Lifetime modeling ..... 61
6.1 Experimental setup ..... 61
6.2 Stress levels ..... 61
6.3 Observations ..... 63
6.3.1 Rapid monitoring of insulation resistance ..... 65
6.4 Modeling the avalanche breakdown failures ..... 65
6.4.1 Activation energy of the Prokopowicz model ..... 69
6.4.2 Voltage exponent of the Prokopowicz model ..... 72
6.4.3 Effect of area on avalanche breakdown failures ..... 74
6.4.4 Applicability of the Prokopowicz model ..... 75

6.5 Modeling the capacitance failures ..... 75
6.5.1 Effect of area on capacitance failures ..... 76
6.6 Investigation of the failure/degradation mechanisms ..... 77
6.6.1 Avalanche breakdown ..... 77
6.6.2 Decrease in capacitance ..... 79
6.7 Comparison with other commercially available embedded capacitor ..... 80
7. Conduction mechanisms in a commercially available capacitor ..... 84
7.1 Measurement of leakage current ..... 84
7.2 Evaluation of Ohmic conduction ..... 86
7.3 Evaluation of Arrhenius behavior ..... 88
7.4 Evaluation of Schottky, Poole-Frenkel and Hopping ..... 89
8. Conduction mechanisms in a fabricated capacitor ..... 95
8.1 Measurement of leakage current ..... 95
8.2 Evaluation of Ohmic behavior ..... 101
8.3 Evaluation of Schottky and Poole-Frenkel mechanism ..... 104
8.4 Evaluation of hopping mechanism ..... 110
8.4.1 Activation energy of hopping ..... 113
8.5 Calculating the theoretical trend of activation energy ..... 115
8.5.1 As a function of ceramic loading ..... 115
8.5.2 As a function of ceramic particle diameter ..... 121
8.6 Application of the Lichtenecker equation ..... 125
9. Conclusions ..... 129
9.1 Temperature humidity bias (THB) tests ..... 129
9.2 Lifetime modeling ..... 130
9.3 Conduction mechanisms in epoxy-$BaTiO_3$ composite dielectric ..... 130
10. Contributions ..... 132
10.1 Temperature humidity bias (THB) tests ..... 132
10.2 Lifetime modeling ..... 133
10.3 Conduction mechanisms in epoxy-$BaTiO_3$ composite dielectric ..... 133
11. Limitations of this Research and Future work ..... 135
11.1 Temperature humidity bias (THB) tests ..... 135
11.2 Lifetime modeling ..... 136
11.3 Conduction mechanisms in epoxy-$BaTiO_3$ composite dielectric ..... 137
12. References ..... 138

## Index of figures

Figure 1-1. Sectional view of a multilayered printed wiring board (PWB) with an embedded planar capacitor laminate. 2
Figure 1-2. Polymer ceramic composites combining the advantages of using both polymer and ceramic. 4
Figure 1-3. Increase in leakage current with an increase in the ceramic loading. 8
Figure 2-1. Charge carriers hopping an array of potential barriers leading to hopping conduction. 16
Figure 2-2. Process steps for the preparation of the dielectric paste. 18
Figure 2-3. Electrostatic stabilization mechanism in barium titanate. 19
Figure 2-4. Steric stabilization mechanism in barium titanate. 19
Figure 2-5. Manufacturing of embedded capacitors using spin coating. 20
Figure 2-6. Manufacturing of embedded capacitors using meniscus coating. 21
Figure 2-7. Manufacturing of embedded capacitors using roll coating. 21
Figure 3-1. Test vehicle with capacitors of group A (small) and group B (large) for THB test and highly accelerated life tests 22
Figure 3-2. Schematic of sectional view of the test vehicle with embedded planar capacitor laminate as layer 2 and 3. 23
Figure 3-3. Sectional view of the test vehicle as observed through a scanning electron microscope (SEM). 23
Figure 3-4. Magnified view of the epoxy-$BaTiO_3$ composite dielectric as observed through a scanning electron microscope. 24
Figure 3-5. Cole-Parmer 8890 ultrasonic cleaning equipment. 26
Figure 3-6. Rock tumbler with Zirconia ($ZrO_2$) grinding media (spherical balls of 10 mm diameter) used for ball milling. 26
Figure 3-7. Process steps for the fabrication of Cu/dielectric/Cu structures. 27
Figure 3-8. Isothermal differential scanning calorimetry (DSC) scans of the polymer (only with curing agent) at various temperatures. 28
Figure 3-9. The fabricated Cu/dielectric/Cu structure. 29
Figure 3-10. Cross sectional view of the capacitor (at 0% and 60% loading of $BaTiO_3$). 29
Figure 3-11. SEM view of the composite dielectric for $BaTiO_3$ particles of different diameter (at a loading of 40% by volume). 30
Figure 3-12. SEM view of the composite dielectric at different loading of $BaTiO_3$ particles (of diameter 500 nm). 31
Figure 3-13. Measurements of dielectric thickness 32
Figure 4-1. Effect of temperature on capacitance (of TV-1 with 8 μm dielectric thickness). 33
Figure 4-2. Effect of temperature on dissipation factor (of TV-1 with 8 μm dielectric thickness). 34
Figure 4-3. Effective dielectric constant versus $BaTiO_3$ loading: experimental data and Lichtenecker equation (for $BaTiO_3$ particles of 500 nm diameter). 35
Figure 4-4. Effective dielectric constant of the composite versus diameter of $BaTiO_3$ particles (for 40% loading by volume of $BaTiO_3$ particles). 35
Figure 4-5. Effect of temperature on capacitance at different loading conditions (vol. %) of $BaTiO_3$ in the composite (for $BaTiO_3$ particles of 500 nm diameter). 36

Figure 4-6. Effect of temperature on capacitance for $BaTiO_3$ particles of different diameters in the composite (at 40% loading by volume of $BaTiO_3$ particles)..... 36
Figure 4-7. Temperature coefficient of capacitance (TCC) at different loading conditions (vol. %) of $BaTiO_3$ in the composite (for $BaTiO_3$ particles of 500 nm diameter). ..... 37
Figure 4-8. Temperature coefficient of capacitance (TCC) for $BaTiO_3$ particles of different diameter in the composite (at 40% loading by volume of $BaTiO_3$ particles)..... 37
Figure 4-9. Effect of temperature on dissipation factor at different loading conditions (vol. %) of $BaTiO_3$ in the composite (for $BaTiO_3$ particles of 500 nm diameter). ..... 38
Figure 4-10. Effect of temperature on dissipation factor for $BaTiO_3$ particles of different diameter in the composite (at 40% loading by volume of $BaTiO_3$ particles). ..... 38
Figure 5-1. Weight of one PWB while baking at 105 $^oC$. ..... 40
Figure 5-2. Dissipation factor while baking at 105 $^oC$..... 40
Figure 5-3. Schematic of the test vehicle with resistors of resistance 1.1 MΩ added in series to each capacitor..... 41
Figure 5-4. Schematic of the experimental setup used for the temperature-humidity-bias (THB) tests..... 41
Figure 5-5. Capacitance of small (group A) capacitors at 85 $^oC$ and 85% RH..... 43
Figure 5-6. Capacitance of large (group B) capacitors at 85 $^oC$ and 85% RH..... 43
Figure 5-7. Dissipation factor of small (group A) capacitors at 85 $^oC$ and 85% RH..... 44
Figure 5-8. Dissipation factor of large (group A) capacitors at 85$^oC$ and 85% RH..... 44
Figure 5-9. Q-Q plot between capacitance and dissipation factor for one small (group A) capacitor at 85 $^oC$ and 85% RH. ..... 45
Figure 5-10. Failures as a result of a drop in the insulation resistance observed at 85 $^oC$, 85% RH, and 5 V (for one small capacitor)..... 46
Figure 5-11. Unreliability versus time plot for small (group A) capacitors at 85 $^oC$, 85% RH, and 5 V..... 46
Figure 5-12. Relative capacitance of one small (group A) and large (group B) capacitor during baking at 125 $^oC$. ..... 47
Figure 5-13. Relative dissipation factor of one small (group A) and large (group B) capacitor during baking at 125 $^oC$..... 48
Figure 5-14. Q-Q plot between capacitance and dissipation factor for one small (group A) capacitor during baking at 125 $^oC$..... 49
Figure 5-15. Disappearance of the insulation resistance failures during baking at 125 $^oC$ (for one small capacitor). ..... 50
Figure 5-16. Possible low resistance path formed under THB conditions. ..... 51
Figure 5-17. Path of moisture ingress in the capacitor dielectric. ..... 52
Figure 5-18. Dirichlet boundary condition on the five edges. ..... 53
Figure 5-19. FEM model of group A capacitor. ..... 57
Figure 5-20. Methodology of modeling diffusion of moisture inside the embedded capacitor dielectric. ..... 58
Figure 5-21. Optimizing the values of D and A (for small capacitors)..... 58
Figure 5-22. Theoretical versus experimental capacitance for small capacitors ..... 59
Figure 5-23. Optimizing the values of D and A (for large capacitors)..... 60
Figure 5-24. Theoretical versus experimental capacitance for large capacitors. ..... 60
Figure 5-25. Concentration of moisture in large capacitors at 2000 hrs. ..... 60

Figure 6-1. Effect of temperature on the breakdown voltage ($V_{BD}$) of small (group A) capacitors. ..... 62
Figure 6-2. Insulation resistance of one small (group A) capacitor at ..... 63
Figure 6-3. Dissipation factor of one small (group A) capacitor at 125 $^{o}$C and 285 V. .... 64
Figure 6-4. Capacitance of one large (group B) capacitor at 125 $^{o}$C and 285 V. ..... 64
Figure 6-5. Rapid monitoring of insulation resistance at 125 $^{o}$C and 285 V for one large (group B) capacitor. ..... 65
Figure 6-6. Probability density function of the time-to-failure at 125 $^{o}$C and 285 V for small (group A) capacitors. ..... 67
Figure 6-7. Probability density function of the time-to-failure at 125 $^{o}$C and 250 V for small (group A) capacitors. ..... 67
Figure 6-8. Probability density function of the time-to-failure at 115 $^{o}$C and 285 V for small (group A) capacitors. ..... 68
Figure 6-9. Probability density function of the time-to-failure at 105 $^{o}$C and 285 V for small (group A) capacitors. ..... 68
Figure 6-10. Probability density function of the time-to-failure at 125$^{o}$C and 225 V for small (group A) capacitors. ..... 69
Figure 6-11. Unreliability versus time plot at different temperatures (at a constant voltage of 285 V) for small (group A) capacitors. ..... 70
Figure 6-12. The effect of temperature on the mean time to failure (MTTF) of small (group A) capacitors at 285 V. ..... 72
Figure 6-13. Unreliability versus time plot at different voltages (at a constant temperature of 125 $^{o}$C) for small (group A) capacitors. ..... 72
Figure 6-14. The effect of voltage on the mean time to failure (MTTF) of small (group A) capacitors at 125 $^{o}$C. ..... 74
Figure 6-15. Percentage change in capacitance at different stress levels for small (group A) and large (group B) capacitors. ..... 76
Figure 6-16. Sample preparation steps to investigate the site of avalanche breakdown... 78
Figure 6-17. The site of avalanche breakdown, seen as the dark region in the dielectric. 79
Figure 6-18. Capacitance of one small (group A) capacitor during heating at 130 $^{o}$C. .... 80
Figure 6-19. Insulation resistance of one small (group A) capacitor from TV-2 (14 μm dielectric thickness) at 125 $^{o}$C and 285 V. ..... 81
Figure 6-20. Dissipation factor of one small (group A) capacitor from TV-2 (14 μm dielectric thickness) at 125 $^{o}$C and 285 V. ..... 81
Figure 6-21. Capacitance of one large (group B) capacitor from TV-2 (14 μm dielectric thickness) at 125 $^{o}$C and 285 V. ..... 82
Figure 6-22. Unreliability versus time plot for small (group A) capacitors at 125 $^{o}$C and 285 V. ..... 83
Figure 7-1. Agilent 4155C semiconductor parameter analyzer. ..... 85
Figure 7-2. Thermostream (air stream temperature forcing system from Temptronic Corporation). ..... 85
Figure 7-3. Leakage current versus temperature at various voltages in one capacitor. .... 86
Figure 7-4. Logarithm of current density versus logarithm of electric field at various temperatures. ..... 87
Figure 7-5. Electric field exponent (p) at various temperatures. ..... 87

Figure 7-6. Logarithm of current density versus reciprocal of absolute temperature at various voltages. ..... 88
Figure 7-7. Validation of ionic hopping and Schottky emission. ..... 91
Figure 7-8. Logarithm of current density versus square root of electric field at various temperatures. ..... 92
Figure 7-9. Dielectric constant calculated from the leakage current data assuming Schottky emission at various temperatures. ..... 93
Figure 7-10. 3D regression of the leakage current data to calculate the constants of Schottky emission. ..... 93
Figure 8-1. Leakage current as a function of temperature and voltage for one capacitor with 0% loading of $BaTiO_3$. ..... 96
Figure 8-2. Current versus voltage plots (at 25$^oC$ ) at various $BaTiO_3$ loading conditions (vol. %) for one capacitor. ..... 97
Figure 8-3. Current versus voltage plots (at 125$^oC$) at various $BaTiO_3$ loading conditions (vol %) for one capacitor. ..... 97
Figure 8-4. Current versus voltage plots (at 25$^oC$) for various diameters of $BaTiO_3$ particles for one capacitor. ..... 98
Figure 8-5. Current versus voltage plots (at 125$^oC$) for various diameters of $BaTiO_3$ particles for one capacitor. ..... 98
Figure 8-6. Current versus temperature plots (at 1V) at various $BaTiO_3$ loading conditions (vol %) for one capacitor. ..... 99
Figure 8-7. Current versus temperature plots (at 50V) at various $BaTiO_3$ loading conditions (vol %) for one capacitor. ..... 99
Figure 8-8. Current versus temperature plots (at 1V) for various diameters of $BaTiO_3$ particles for one capacitor. ..... 100
Figure 8-9. Current versus temperature plots (at 50 V) for various diameters of $BaTiO_3$ particles for one capacitor. ..... 100
Figure 8-10. Logarithm of current density versus logarithm of electric field (at 25 $^oC$) at various $BaTiO_3$ loading conditions (vol. %) for one capacitor. ..... 101
Figure 8-11. Logarithm of current density versus logarithm of electric field (at 125 $^oC$) at various $BaTiO_3$ loading conditions (vol. %) for one capacitor. ..... 102
Figure 8-12. Logarithm of current density versus logarithm of electric field (at 25 $^oC$) for various diameters of $BaTiO_3$ particles for one capacitor. ..... 102
Figure 8-13. Logarithm of current density versus logarithm of electric field (at 125 $^oC$) for various diameters of $BaTiO_3$ particles for one capacitor. ..... 103
Figure 8-14. Mean value of the electric field exponent (p) at various loading conditions of $BaTiO_3$ (vol. %) at different temperatures. ..... 103
Figure 8-15. Mean value of the electric field exponent (p) for various diameters of $BaTiO_3$ particles at different temperatures. ..... 104
Figure 8-16. Logarithm of current density versus square root of electric field (at 25 $^oC$) at various $BaTiO_3$ loading conditions (vol. %) for one capacitor. ..... 105
Figure 8-17. Logarithm of current density versus square root of electric field (at 125 $^oC$) at various $BaTiO_3$ loading conditions (vol. %) for one capacitor. ..... 106
Figure 8-18. Logarithm of current density versus square root of electric field (at 25 $^oC$) for various diameters of $BaTiO_3$ particles for one capacitor. ..... 106

Figure 8-19. Logarithm of current density versus square root of electric field (at 125 $^{o}$C) for various diameters of $BaTiO_3$ particles for one capacitor. ..... 107
Figure 8-20. Calculated mean dielectric constant assuming Schottky emission for various loading conditions of $BaTiO_3$. ..... 108
Figure 8-21. Calculated mean dielectric constant assuming Poole-Frenkel emission for various loading conditions of $BaTiO_3$. ..... 108
Figure 8-22. Calculated mean dielectric constant assuming Schottky emission for various diameters of $BaTiO_3$ particles. ..... 109
Figure 8-23. Calculated mean dielectric constant assuming Poole-Frenkel emission for various diameters of $BaTiO_3$ particles. ..... 109
Figure 8-24. Log JT versus (1/T) at 1V for various loading conditions of $BaTiO_3$ (vol. %) for one capacitor. ..... 111
Figure 8-25. Log JT versus (1/T) at 50 V for various loading conditions of $BaTiO_3$ (vol. %) for one capacitor. ..... 111
Figure 8-26. Log JT versus (1/T) at 1 V for various diameters of $BaTiO_3$ particles for one capacitor. ..... 112
Figure 8-27. Log JT versus (1/T) at 50 V for various diameters of $BaTiO_3$ particles for one capacitor. ..... 112
Figure 8-28. 3D regression of the leakage current data to calculate the activation energy of the hopping mechanism for one capacitor with 0% loading. ..... 113
Figure 8-29. Mean activation energy of hopping as a function of $BaTiO_3$ loading (for diameter of $BaTiO_3$ particles equal to 500 nm). ..... 114
Figure 8-30. Mean activation energy of hopping as a function of diameter of $BaTiO_3$ particles (at 40% loading of $BaTiO_3$ particles by volume). ..... 114
Figure 8-31. Applicability of Lichtenecker model at 25$^{o}$C and 1 V. ..... 116
Figure 8-32. Applicability of Lichtenecker model at 25$^{o}$C and 50 V. ..... 117
Figure 8-33. Applicability of Lichtenecker model at 125 $^{o}$C and 1 V. ..... 117
Figure 8-34. Applicability of Lichtenecker model at 125 $^{o}$C and 50 V. ..... 117
Figure 8-35. Trend of activation energy as a function of ceramic loading ..... 119
Figure 8-36. Increase in the number of contacts with a decrease in the particle size (at a constant loading). ..... 121
Figure 8-37. Conductivity of the composite as a function of ceramic diameter (1 V and 25$^{o}$C) ..... 122
Figure 8-38. Conductivity of the composite as a function of ceramic diameter (50 V and 25$^{o}$C) ..... 122
Figure 8-39. Conductivity of the composite as a function of ceramic diameter (1 V and 125$^{o}$C) ..... 123
Figure 8-40. Conductivity of the composite as a function of ceramic diameter (50 V and 125$^{o}$C) ..... 123
Figure 8-41. Trend of activation energy as a function of ceramic particle diameter ..... 125
Figure 8-42. Mean conductivity of epoxy and $BaTiO_3$ (particle diameter=500 nm) as a function of temperature at 1 V. ..... 126
Figure 8-43. Mean conductivity of epoxy and $BaTiO_3$ (particle diameter=500 nm) as a function of temperature at 50 V. ..... 126
Figure 8-44. Mean conductivity of epoxy and $BaTiO_3$ (particle diameter=500 nm) as a function of voltage at 25$^{o}$C. ..... 127

Figure 8-45. Mean conductivity of epoxy and $BaTiO_3$ (particle diameter=500 nm) as a function of voltage at 125$^{o}$C. ..... 127
Figure 8-46. Deviations from Ohmic behavior in the composite. ..... 128

# 1. Introduction

## *1.1 Background*

The basic building blocks of an electronic circuit consist of active and passive components on a printed wiring board (PWB). These passive components consist of capacitors, resistors and inductors that result in no power gain in the circuit. In a typical electronic product such as a cell phone, the ratio of passive to active components is about 20:1, and about 80% of the board is occupied by these passive components [1]. Among all passives, capacitors are of particular interest since capacitors are used in various applications such as decoupling, filtering, and noise suppression, and are used in large numbers on PWBs. In a typical hand held product such as a cell phone the number of passive components is about 300-400, most of which are capacitors [2]. The component density due to these passives is increasing due to increasing demands in telecommunication, computer, automotive, and consumer sectors while PWB designers simultaneously strive for product miniaturization.

It has been found that the use of thin laminates known as embedded planar capacitor can reduce the number of surface mount capacitors and aid in product miniaturization [3]. These capacitors have also been found to improve the electrical performance (such as lower electromagnetic interference) [4][5]of PWBs. An embedded planar capacitor (Figure 1-1) consists of a thin laminate (≈ 10-50 μm dielectric thickness) embedded in a PWB that functions both as a power-ground plane and as a parallel plate capacitor [6].

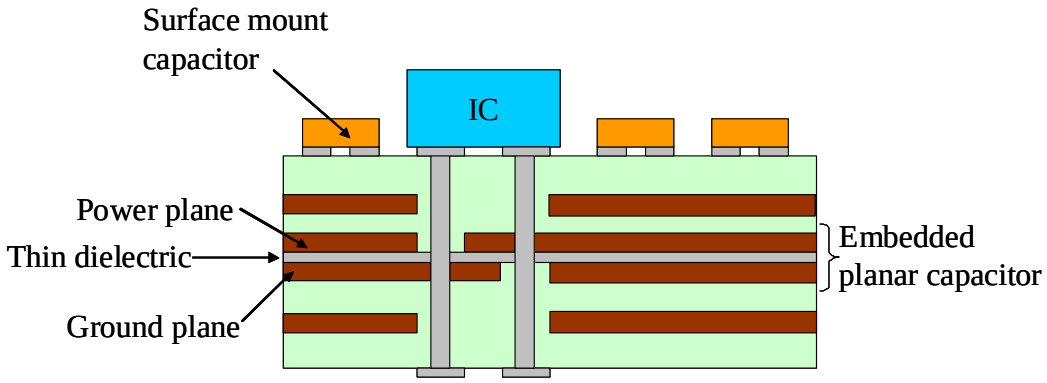


***Figure 1-1.*** *Sectional view of a multilayered printed wiring board (PWB) with an embedded planar capacitor laminate.*

Embedded planar capacitors are widely used in decoupling applications, which involves maintaining a constant voltage difference between the power and the ground plane in a multilayered PWB. Due to the brief pulses of current drawn by the IC, a voltage fluctuation appears between the power and the ground planes [7], which is known as power-ground plane noise, delta-I noise, or simultaneous switching noise (SSN). This noise is due to parasitic inductance in the power-ground plane path. The voltage drop ($\Delta V$) is given by:

$$\Delta V = IR + L\frac{dI}{dt} \tag{1}$$

where $I$ is the current, $R$ is the resistance, $L$ is the inductance, $I$ is the current drawn by the switching device, and $t$ is the time. The second term of the equation becomes dominant at high frequencies, and the voltage drop is governed by the parasitic inductance ($L$). The traditional solution to eliminate this voltage fluctuation is to add discrete surface mount capacitors between the power and the ground plane that act as charge reservoirs.

Due to steadily increasing operating frequencies and the lowering of supply voltage in digital systems, SSN is a serious concern since it can affect the performance of

high speed systems. Surface mount capacitors provide decoupling from the kHz range up to several MHz [6], but they become ineffective above 100 MHz because of the increased effect of inductance associated with these devices. For a capacitor to function properly in a decoupling operation over a wide range of frequencies it should satisfy the following requirements. First, the capacitance should be high to enable proper functioning at low frequency when the impedance is capacitive. Second, the inductance should be low to enable proper functioning at high frequency when the impedance is inductive. Achieving a high capacitance (on the order of μF) is easy using electrolytic capacitors, but achieving a low value of inductance (≈ pH) is difficult when using surface mount capacitors.

A low value of parasitic inductance (due to elimination of leads and traces) associated with embedded planar capacitor leads to proper functioning in the high frequency range. The parasitic inductance of an embedded planar capacitor further decreases with a decrease in the dielectric thickness, so a thin dielectric is preferred. Due to a lower parasitic inductance ($L$) in embedded capacitors [8], the voltage drop ($\Delta V$) is also low, which leads to a reduction in the required number of surface mount capacitors, thus leading to board miniaturization.

The laminate of an embedded planar capacitor consists of a thin dielectric material sandwiched between copper layers. Polymers such as epoxy and polyimide are used as dielectric material in some applications but they have a low value of dielectric constant. Ceramics such as $BaTiO_3$ have a high dielectric constant (~15,000) [9] but their processing temperature is high (~ $850^oC$) [10] and not compatible with the regular PWB manufacturing process. To overcome the above limitations, a composite of polymer and ceramic is used. The advantage of using a polymer-ceramic composite is that it combines

(Figure 1-2) the low temperature processability of polymers with the high dielectric constant of ceramics [11].

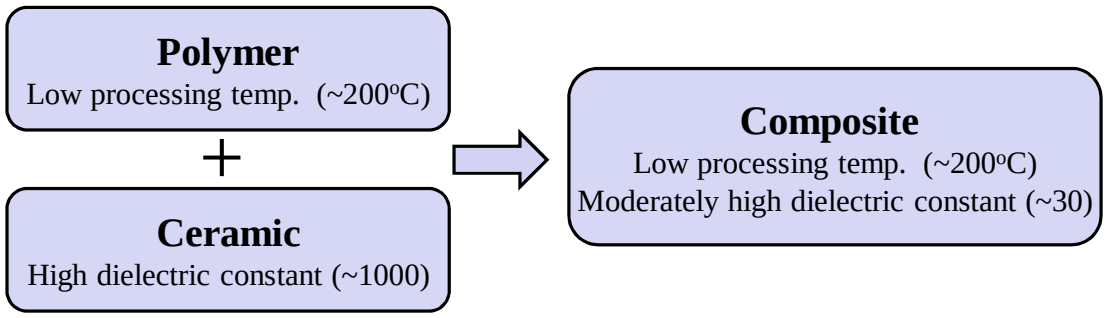


***Figure 1-2.*** *Polymer ceramic composites combining the advantages of using both polymer and ceramic.*

The most widely used composite material is the epoxy-$BaTiO_3$ composite. The dielectric constant of $BaTiO_3$ is size-dependent and exhibits a peak value when the particle size is close to 140 nm [12] so nanoparticles of $BaTiO_3$ are preferred in the composite. Further the dielectric constant of $BaTiO_3$ also depends on the processing conditions, nature of dopants, and the frequency and temperature of measurements [13]. With an increase in the ceramic loading the effective dielectric constant of the composite increases and various models has been proposed to describe this behavior [14]-[17]. It was observed that an increase in the $BaTiO_3$ loading beyond 55-60% by volume decreased the capacitance [18]. This was attributed to an increase in the number of voids and pores in the composite when the theoretical maximum packing density approached or exceeded. Typically, for reliability reasons the maximum $BaTiO_3$ loading should be lower than 50% by volume, which limits the maximum dielectric constant of this (epoxy-$BaTiO_3$) composite to about 30 in commercially available dielectrics.

The concept of the embedded planar capacitor for use in PWBs dates back to the 1960s (U.S. Pat. No. 3,519,959) by the use of very thin epoxy glass between copper

power and ground planes in a multilayered PWB [19]. The clock frequency in digital systems is increasing, and the thrust in embedded capacitors is to decrease the dielectric thickness (which reduces the parasitic inductance and increases the capacitance density) and increase the dielectric constant of the dielectric material (which increases the capacitance density). The use of embedded capacitors in hand-held RF devices has already been demonstrated [20][21]. A reduction of at least 14% in PWB area was observed by the use of embedded capacitors in a Blue-tooth module [22]. High volume production of embedded passives in PWBs was initiated by Murata (1997), which was followed by Hitachi (1999), Kyocera (1999), TDK (1999), and NGK (2000) [23].

## *1.2 Motivation*

Advances in the fabrication of embedded planar capacitors have occurred in response to miniaturization of the PWB size and an improvement in the electrical properties. Although embedded planar capacitors have many advantages there are some gaps in the existing research that needs to be filled for wider commercialization of these capacitors.

The reliability of these capacitors should be understood better since these capacitors are not reworkable and the entire PWB will have to be changed in case of a failure. Further, a drift in the electrical parameters (such as capacitance, dissipation factor, and insulation resistance) of an embedded planar capacitor can affect the performance of the circuit where these capacitors are used. In this work the reliability of these capacitors is investigated under temperature-humidity-bias (THB) tests and highly accelerated life tests.

Polymer-ceramic composites are widely commercialized as the dielectric material, but these materials still have some shortcomings. One of these is an increase in the leakage current with an increase in the ceramic loading. In this work the conduction of leakage current in a composite of epoxy and $BaTiO_3$ is investigated.

### 1.2.1 Temperature-humidity-bias tests

Under humid conditions the dielectric constant (and hence capacitance and dissipation factor) of these composites increases due to water absorption. The level of moisture absorbed in polymer-ceramic nanocomposites is higher compared to pure polymer or micron-filled polymer [24]. It was observed that nanocomposites absorb up to 60% more water than unfilled and micron-filled epoxies [25]. The main site of water absorbed is the interface of epoxy and $BaTiO_3$, and under humid conditions the ceramic particles are surrounded by a shell of water. A possible explanation for this increased water absorption is that some capillaries might be formed at the interfaces between nanoparticles and the polymer matrix, which could pump the water into the bulk of the polymer matrix.

Previous studies on the reliability of embedded capacitors with epoxy-$BaTiO_3$ composite dielectric have not investigated the effect of an applied bias under humid conditions. The presence of an applied bias under humid conditions is expected to reduce the insulation resistance of this material. The leakage current path is expected to be formed by the overlap of consecutive water shells.

### 1.2.2 Lifetime modeling

When a nanocomposite dielectric is made by mixing a material of high dielectric constant ($BaTiO_3$) with a material of low dielectric constant (epoxy), the electric field is not uniform throughout the material [26]. The electric field is higher in the epoxy resin than in $BaTiO_3$. This electric field can be further disrupted by manufacturing defects such as formation of $BaTiO_3$ agglomerates due to attractive Vander Walls forces [27] and due to voids in the dielectric. These defects have the highest magnitude of electric field and can lead to breakdown of the dielectric. A standard industrially acceptable test to precipitate manufacturing defect-related failures in embedded planar capacitors is the hi-pot test [28]. The hi-pot test is a go/no-go test in which a potential of up to 500 V is applied across the embedded capacitor laminate for a period of time. One shortcoming of hi-pot test is that it does not precipitate wear-out time dependant failures, the analysis of which is necessary for the improvement of dielectric material of these capacitors.

To precipitate wear-out failures a combined temperature and voltage aging test can to be conducted for a longer duration of time. These tests are known as highly accelerated life tests and are common in multilayer ceramic capacitors (MLCCs) with pure $BaTiO_3$ dielectric. Further, a time-to-failure model as a function of the temperature and voltage stress during highly accelerated life testing can also be developed using the Prokopowicz model [29]:

$$\frac{t_1}{t_2} = \left(\frac{V_2}{V_1}\right)^n \exp\left(\frac{E_a}{k}\left(\frac{1}{T_1} - \frac{1}{T_2}\right)\right) \tag{2}$$

where $t$ is the time-to-failure as a result of an increase in the leakage current , $T$ is the temperature and $V$ is the voltage, $n$ is the voltage exponent, $E_a$ is the activation energy, $k$

is the Boltzmann constant, and the subscripts 1 and 2 refer to the two stress conditions. The applicability of this model for a composite of epoxy and $BaTiO_3$ has not been investigated. This model can be used for the qualification tests of embedded planar capacitors, for the development of new composite dielectric materials, and to improve the manufacturing processes of these capacitors.

### 1.2.3 Conduction mechanisms

In order to increase the effective dielectric constant ($\varepsilon_c$) of the epoxy-$BaTiO_3$ composite, the ceramic loading is increased in the composite. But it has been found that with an increase in the ceramic ($BaTiO_3$) loading, the value of the undesirable leakage current across the dielectric material also increases [30] as shown in Figure 1-3.

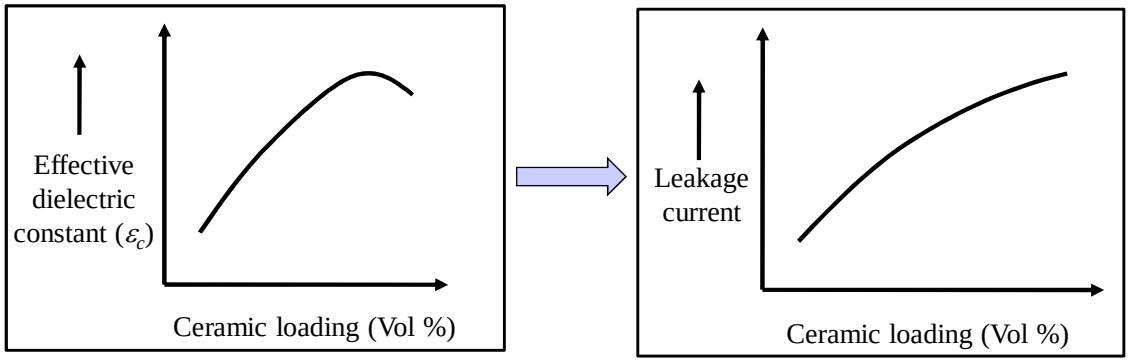


***Figure 1-3.*** *Increase in leakage current with an increase in the ceramic loading.*

An increase in the leakage current across the dielectric material can lead to higher power losses in the dielectric. The conduction mechanism of this leakage current is not well understood. There are some unanswered questions regarding the conduction mechanism such as:

- What is the mechanism of charge carrier transport (such as hopping, Schottky emission, Poole–Frenkel, or tunneling)?

- What is the path of the charge carriers: epoxy, $BaTiO_3$ or the interface of epoxy and $BaTiO_3$?
- Does the mechanism of charge carrier transport change with $BaTiO_3$ loading and particle size?

## *1.3 Dissertation objectives*

The problems identified in the previous section needs to be investigated for wider commercialization of embedded planar capacitors. Since failure of an embedded planar capacitor can lead to board failure, the reliability of these capacitors needs to be investigated. Further, to improve the epoxy-$BaTiO_3$ composite dielectric for use as dielectric material the mechanism of leakage current needs to be identified. The main objectives of this dissertation can be summarized as:

- Investigate the reliability of embedded planar capacitors during temperature-humidity-bias (THB) tests.
- Investigate the reliability of embedded planar capacitors during highly accelerated life tests.
- Model the time-to-failure of embedded planar capacitors during highly accelerated life tests using the Prokopowicz model.
- Investigate the mechanism of conduction in an epoxy-$BaTiO_3$ composite dielectric.

# 2. Literature Review

## *2.1 Reliability under elevated temperature and humid conditions*

The reliability of embedded capacitors with polymer ceramic composite dielectric during elevated temperature and humidity conditions (85$^{o}$C/85% RH) was investigated [31]. After 100 hrs of elevated temperature and humidity test, the capacitance was found to increase by about 4%. In another work, the reliability of embedded capacitors was investigated during pressure cooker test (121$^{o}$C/100% RH) for 4 hrs, and an increase in capacitance by about 10% was observed [32].

Even though moisture absorption is a reversible process, conducting the solder reflow process after moisture absorption can lead to delamination and cracks in the dielectric. Embedded capacitors stored at 60$^{o}$C/65%RH for 168 hrs were subjected to a reflow cycle that led to a decrease in capacitance by 40% [33]. Delamination was observed at the interface of Cu and the dielectric. This delamination was explained by the rapid evaporation of absorbed moisture, and it is well known that the adhesion between polymers and other substrates is weakened when aged in humid conditions [34]. In another work, embedded capacitors were aged at 85$^{o}$C/85%RH for 24 hrs and reflowed three times at 260$^{o}$C for 60 seconds. The capacitance was observed to decrease by 30% [35] due to delamination. The effects of material formulations such as filler loading, dispersant, and curing agent were investigated to reduce the phenomenon of delamination. It was confirmed using scanning acoustic microscope that delaminations

can be reduced but not eliminated by decreasing the ceramic loading (which reduces the adhesion between the dielectric and the Cu plates).

The effect of ceramic ($BaTiO_3$) loading on the reliability of embedded capacitors during temperature and humidity conditions ($85^oC$/85% RH) was investigated for 1000 hrs [36]. Three types of composites with 50, 60, and 70 vol% of ceramic were selected. It was observed that with an increase in the ceramic loading (from 50 vol% to 60 vol% ) the capacitance after 1000 hr of test also increased. This behavior was explained due to an increase in the interfacial area between the polymer and the ceramic, leading to increased moisture absorption and, hence, increased capacitance. However, a further increase in the ceramic from 60 vol% to 70 vol% decreased the capacitance. This was explained due to a reduction in the interfacial area in the 70 vol% composite due to an increase in porosity of the dielectric.

There are various published works on the reliability of embedded capacitors under elevated temperature and humidity conditions. But the effect of an applied bias under these conditions has not been investigated. Under these conditions, the insulation resistance of the dielectric is expected to reduce due to the overlap of water shells around the ceramic particles providing a low resistance conduction path.

## *2.2 Reliability under elevated temperature and voltage conditions*

Under elevated temperature and voltage condition, failures or parametric drifts such as changes in capacitance, dissipation factor, and insulation resistance can take place. These degradation mechanisms are due to temperature alone or due to combined

temperature and voltage conditions. Due to elevated temperature the capacitance of the embedded planar capacitor can decrease. Due to combined temperature and voltage the insulation resistance of the dielectric can decrease or the dissipation factor of the dielectric can increase (in addition to a decrease in the value of capacitance).

At elevated temperatures, the capacitance can decrease due to an increase in the spacing between the plates due to thermal deformation and delamination in the capacitor laminate [37]. These phenomena are driven by the thermo-mechanical stresses developed at the dielectric-Cu plane interface. Stress arises due to the difference in the coefficient of thermal expansion (CTE) of the dielectric and the Cu plane. Possible sources of thermal stresses can be variations in the ambient temperature, self-heating due to power dissipation, and manufacturing processes such as solder reflow. The thermal stress due to CTE mismatch can be expressed by the following equation [38]:

$$\sigma = c\int_{T_1}^{T_2}\left[\frac{\alpha_p - \alpha_i}{\frac{1}{E_p} - \frac{1}{E_i}}\right]dT \tag{3}$$

where $c$ is a geometry-dependent constant, $\alpha$ is the coefficient of thermal expansion (CTE), $E$ is the modulus of elasticity, and the subscripts $p$ and $i$ denote the dielectric and the Cu plane, respectively. The addition of ceramic fillers in the polymer matrix brings down the effective CTE of the composite dielectric close to Cu (17 ppm/$^{o}$C), but the modulus of elasticity increases, which can still lead to an increase in the thermal stress. The modulus of elasticity can also be reduced by modifying the epoxy resin. One way of modifying the epoxy resin is by the use of a rubberized polymer (carbonyl terminated

butadiene-acrylonitrile epoxy) in which a reduction in the modulus by about 29% was achieved [39].

Another possible thermally activated mechanism that can lead to a decrease in the capacitance is aging in $BaTiO_3$ [40]. It has long been known that the dielectric constant of ceramics suffers a loss of 15-20% in the course of a year. Aging can be described by the well known equation [41]:

$$C = C_o - k\left[\log(t)\right] \tag{4}$$

where $C$ is the capacitance after time $t$, $C_o$ is the initial capacitance, $k$ is the dielectric aging rate, and $t$ is the time. The aging rate $k$ is a material property and increases with an increase in the temperature [42]. Aging is a gradual process in dielectrics made of barium titanate and begins after the capacitor's last excursion beyond the Curie temperature (~130$^o$C in $BaTiO_3$). Capacitors can be restored to their original capacitance (or dielectric constant) by heating them above their Curie point for a period of time [43]. Another possible mechanism of decrease in the dielectric constant is due to residual stress relaxation in the polymer matrix [44]. The residual stresses in the polymer matrix generated during the curing process can be relaxed by exposure to temperatures above the glass transition temperature ($T_g$). Polymer chains can freely move above $T_g$, at which point their total volume increases. An increase in free volume leads to a decrease in the dielectric constant since the dielectric constant of free volume is equal to 1.0.

Under combined temperature and voltage aging the leakage current across the dielectric can also increase with time (observed in pure $BaTiO_3$ dielectric in a MLCC [45]). Typically, there are two modes for an increase in the leakage current [46]. In the first mode, there is an abrupt increase in leakage current, which is known as avalanche

breakdown (ABD). In the second mode, known as thermal runaway (TRA), the increase in leakage current is more gradual, which increases the self-heating and results in failure. A higher voltage normally favors the occurrence of an ABD-type of failure mode, while a higher temperature normally favors the TRA-type of failure mode.

Tests with these aging conditions are also known as highly accelerated life tests and are used to precipitate dielectric failures. Highly accelerated life tests of MLCCs with pure $BaTiO_3$ dielectric are common in industry, and the results have been documented in the literature. An empirical model that is used in MLCCs with a pure $BaTiO_3$ dielectric is known as the Prokopowicz model. There are many published studies on the computation of Prokopowicz model constants for pure $BaTiO_3$ dielectric used in MLCCs [47]-[50]. In a pure $BaTiO_3$ dielectric, both TRA and ABD have been observed. TRA has been attributed to the migration of oxygen vacancies. These oxygen vacancies are created due to the firing of $BaTiO_3$ in a reducing atmosphere [51] to prevent the oxidation of the MLCC electrodes (Cu/Ni). ABD has been attributed to manufacturing defects in the dielectric such as porosity and voids. Defects have a higher concentration of electric field, leading to the initiation of dielectric breakdown.

Highly accelerated life tests of embedded planar capacitors with a polymer-ceramic nanocomposite dielectric are not common. In these nanocomposites, ABD is expected due to non-uniform electric field distribution throughout the material.

## *2.3 Conduction mechanisms*

The mechanism of current conduction in $BaTiO_3$ [52][53] and polymer dielectric [54] have been reported. But the electrical conduction in a composite of polymer and

$BaTiO_3$ is not well understood. There are some literature on current conduction in polymer-ceramic composites that investigates the effect of temperature on conductivity (in PVC–$BaTiO_3$ composite) [55] and ceramic loading on the magnitude of leakage current (in PPO–$TiO_2$ composite) [56]. But the mechanism of charge carrier transport (such as hopping, Schottky emission, Poole–Frenkel, or tunneling) has not been investigated for epoxy-$BaTiO_3$ composites.

To investigate the mechanism of electrical conduction across a dielectric, various models of electrical conduction have to be evaluated. Among these mechanisms one or more mechanisms can be dominant depending on the material, applied temperature, or electric field. In this work, the conduction of current across the dielectric is evaluated for consistency with Schottky emission (SE), the Poole-Frenkel (PF) mechanism, and ionic hopping (IH). Another conduction mechanism known as tunneling is not probable in the current case since tunneling is a dominant conduction mechanism at an electric field higher than $10^8$ $Vm^{-1}$ [54].

Schottky emission is due to the thermionic effect that is caused by electron transport across the potential energy barrier by field-assisted lowering at the interface between the metal electrode and the dielectric material. The Schottky emission dominated current density can be expressed as:

$$J = AT^2 \exp\left(\frac{\beta_{SE} E^{1/2} - \phi_{SE}}{kT}\right) \tag{5}$$

where $\beta_{SE} = (e^3/4\pi\varepsilon_o\varepsilon)^{1/2}$, $e$ is the charge on an electron, $\varepsilon_o$ is the permittivity of free space, $\varepsilon$ is the relative dielectric constant of the composite, $A$ is the Richardson constant,

$T$ is the absolute temperature, $\phi_{SE}$ is the contact potential energy barrier, $E$ is the electric field, and $k$ is the Boltzmann constant. Poole-Frenkel emission is caused by the field-enhanced thermal excitation of trapped electrons in the dielectric into the conduction band. The Poole-Frenkel dominated current density can be defined as:

$$J = J_o \exp\left(\frac{\beta_{PF} E^{1/2} - \phi_{PF}}{kT}\right) \tag{6}$$

where $\beta_{PF} = (e^3/\pi\varepsilon_o\varepsilon)^{1/2}$, and $\phi_{PF}$ is the height of the trap potential energy well. In ionic hopping the charge carriers jump an array of potential barriers as shown in Figure 2-1 and may lead to Ohmic conduction. The ionic hopping mechanism was originally formulated for ionic crystals, but it is equally applicable to other materials. The current density as a result of ionic hopping may be expressed as:

$$J = 2nd\nu \exp\left(-\frac{E_a}{kT}\right)\sinh\left(\frac{eEd}{2kT}\right) \tag{7}$$

where $n$ is the number of charge carriers, $d$ is the hopping distance, $\nu$ is the attempt-to-escape frequency, $E_a$ is the activation energy, and $e$ is the charge on an electron.

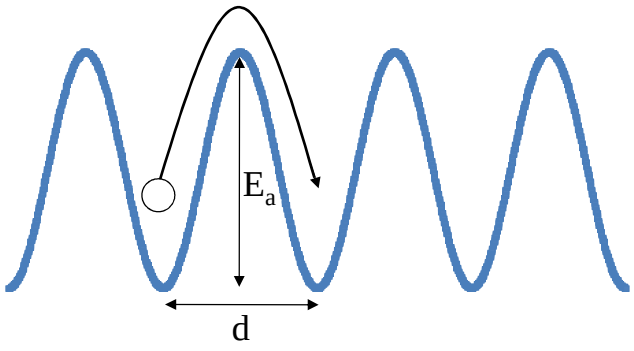


***Figure 2-1.*** *Charge carriers hopping an array of potential barriers leading to hopping conduction.*

## *2.4 Manufacturing of capacitors with composite dielectric*

The manufacturing of embedded capacitors with an epoxy-$BaTiO_3$ composite dielectric involves two steps. The first step is preparation of the dielectric paste using colloidal process and the second step is the manufacturing of the capacitor.

### 2.4.1 Preparation of the dielectric paste

In the preparation of the dielectric paste other materials such as dispersant, solvent, and curing agent are also added [57]. Dispersant is added to prevent agglomeration of ceramic particles due to the attractive van der Waals forces. Solvent is added that acts as a medium in which the ceramic particles are de-agglomerated. Another advantage of the solvent is that it is used to control the viscosity of the dielectric paste. A curing agent is added to cure the polymer. The entire step for the preparation of the dielectric paste is shown in Figure 2-2. First the dispersant and then the ceramic particles are added to the solvent which is followed by Ultrasonification (for ~ 120 mins). Then the polymer and the curing agent are added and the slurry is ball milled (for ~ 2 days). The purpose of Ultrasonification is to break the agglomerates of the ceramic particles and ball milling is performed to prevent settling down of ceramic particles in the dielectric paste.

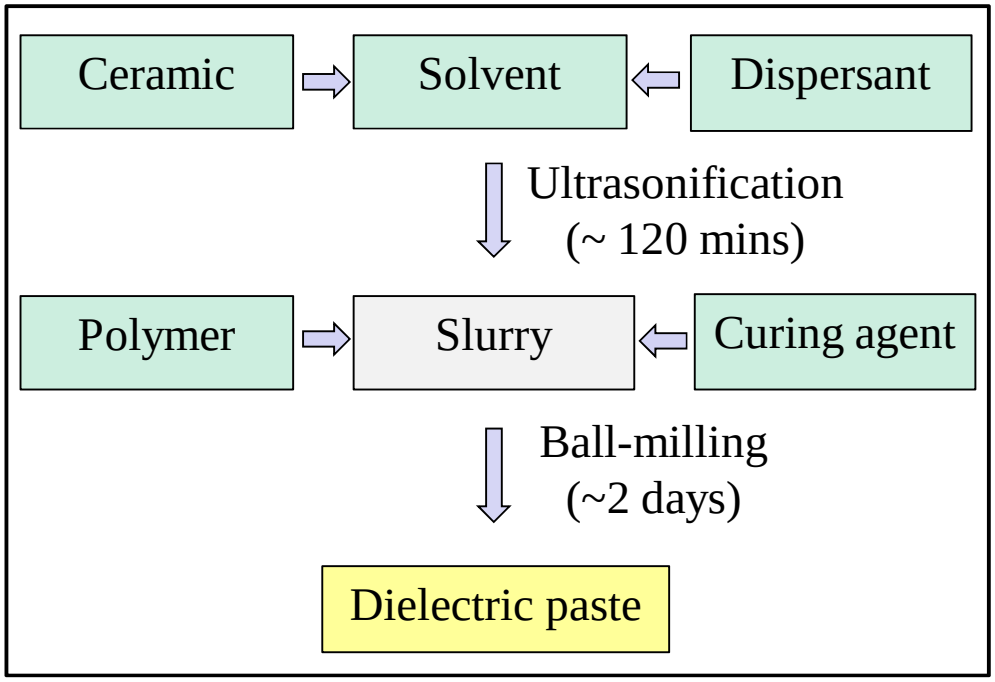


***Figure 2-2.*** *Process steps for the preparation of the dielectric paste.*

Use of proper dispersant prevents the agglomeration of ceramic particles, which leads to better packing and a higher dielectric constant. A dielectric constant as high as 74 was obtained for epoxy-$BaTiO_3$ composites at a proper dispersant level [58]. In another study it was observed that the value of the dielectric constant increased from 40 to 65 with a proper selection of dispersants (at 40% ceramic loading by volume) [59]. With the addition of these dispersants, the ceramic particles can be stabilized by two mechanisms, electrostatic stabilization and polymeric stabilization as shown in Figure 2-3 and Figure 2-4 respectively. In electrostatic stabilization, the attractive van der Waals forces are balanced by the repulsive Coulomb forces between the negatively charged ceramic particles. Polymeric stabilization involves the addition of polymeric molecules on the ceramic surface (also known as steric stabilization), which creates a repulsive force that balances the attractive van der Waals force.

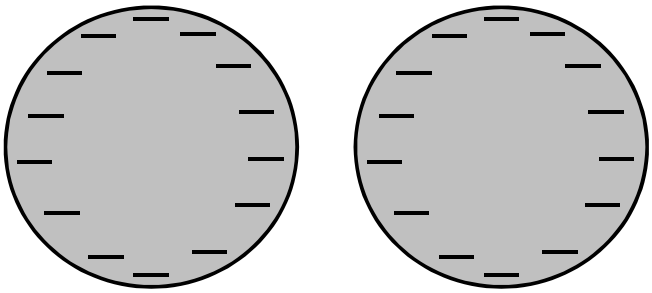

***Figure 2-3.*** *Electrostatic stabilization mechanism in barium titanate.*

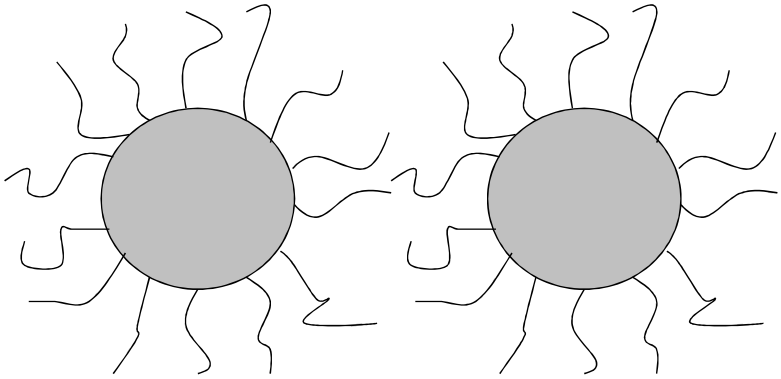

***Figure 2-4.*** *Steric stabilization mechanism in barium titanate.*

Phosphate esters are good dispersants for barium titanate in highly polar solvents like ethanol, water, etc. [60]. Polar solvents can cause the dissociation of phosphate esters and aids in charge generation on the ceramic surface. For most non-polar solvents (or low polarity solvents) the mode of stabilization is steric, and very high molecular weight (>10000) polymeric dispersants are used [60]. However it has been found that even in non-aqueous solvents electrostatic charges may develop on the surface of $BaTiO_3$ leading to electrostatic stabilization [61][62]. $BaTiO_3$ suspended in mixed solvent containing ethanol and acetone, with phosphate ester as additive, was found to be the optimum dispersion condition which combines both electrostatic and steric stabilization mechanisms.

### 2.4.2 Manufacturing of the capacitor

Once the dielectric paste is prepared, embedded capacitor laminate (metal/dielectric/metal) is manufactured using either spin coating, meniscus coating, or roll coating. In spin coating, the dielectric paste is spin-coated on top of a Cu clad substrate and cured followed by deposition of the top Cu layer as shown in Figure 2-5. The thickness of the film in spin coating depends on the spin speed (rpm), viscosity of the dielectric paste, and duration of the spin [63]. A disadvantage of spin coating is its size limitations since it cannot be used to make embedded capacitors of large area.

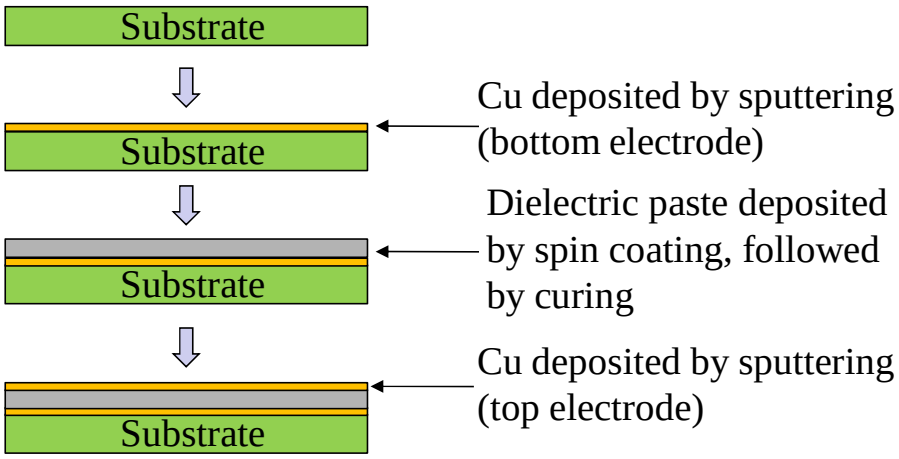


***Figure 2-5.*** *Manufacturing of embedded capacitors using spin coating.*

Meniscus coating is similar to dip coating and is a viable low-cost manufacturing process for depositing thin film (~5 μm) of polymer-ceramic composite dielectric. The major advantages of meniscus coating over dip coating are: (1) low wastage of material, (2) ease of thin film deposition over large area substrates, and (3) applicability to a wide variety of substrate material. Thin films can be deposited on a Cu clad PWB substrate, as shown in Figure 2-6. Slow speed and multiple passes are required to achieve films with good uniformity and the desired thickness.

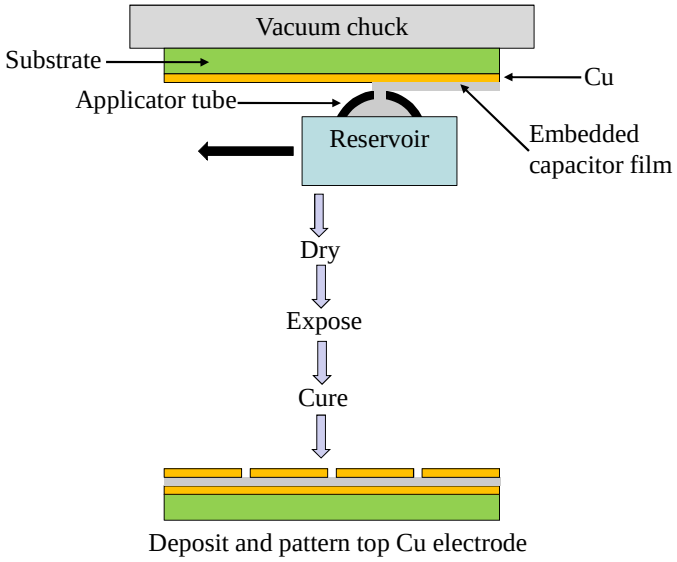


***Figure 2-6.*** *Manufacturing of embedded capacitors using meniscus coating.*

Roll coating can also be used for the deposition of polymer-ceramic composite dielectric. Figure 2-7 shows one type of roll coating in which the dielectric paste is coated on a releasing film using a roll coater [64]. The embedded capacitor film (ECF) on the releasing film is dried sequentially before rewinding. This method is widely used since it can be used to make embedded planar capacitors of large area. Furthermore, the embedded capacitor manufactured is in a laminate form, which can be used as a stack in a multilayered PWB.

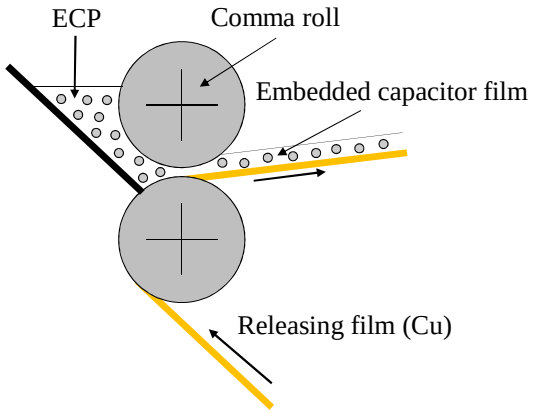


***Figure 2-7.*** *Manufacturing of embedded capacitors using roll coating.*

# 3. Test vehicle

Two different designs of test vehicles are used in this study. The first test vehicle was used for THB test, highly accelerated life tests, and also to investigate the conduction mechanism in epoxy-$BaTiO_3$ composites. This test vehicle was fabricated by a standard PWB manufacturer and had multiple embedded capacitors in a multilayered PWB. The second test vehicle was used to further investigate the conduction mechanism in epoxy-$BaTiO_3$ composites. This test vehicle consisted of Cu/dielectric/Cu coupon with one capacitor per test vehicle. This test vehicle was fabricated in our laboratory using colloidal process.

## *3.1 Test vehicle with multiple embedded capacitors*

This design of the test vehicle was first used in the NCMS embedded capacitor project [65]. The test vehicle consisted of two sizes of capacitors which are termed as group A (small) and group B (large) as shown in Figure 3-1. There were 80 capacitors of group A and 6 capacitors of group B in the test vehicle.

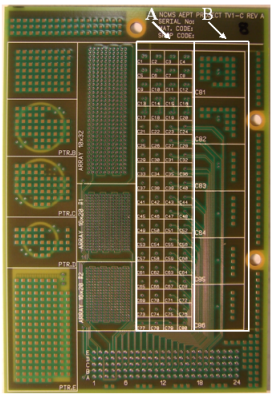


***Figure 3-1.*** *Test vehicle with capacitors of group A (small) and group B (large) for THB test and highly accelerated life tests.*

The test vehicle was a 4-layer PWB (as shown in Figure 3-2 and Figure 3-3) in which layers 1 and 4 were the signal layers, and the planar capacitor laminate (C Ply from 3M) formed layer 2 (power plane) and layer 3 (ground plane). The power plane was etched at various locations to form discrete capacitors and the ground plane was common for all capacitors.

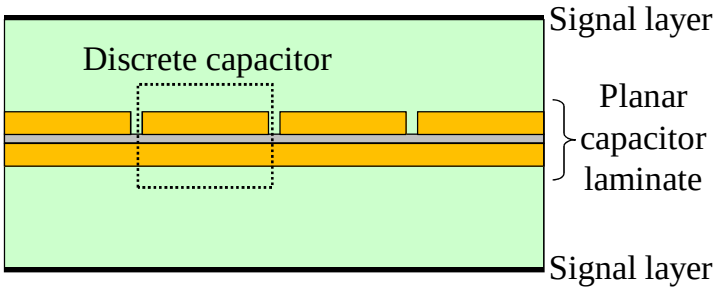


***Figure 3-2.*** *Schematic of sectional view of the test vehicle with embedded planar capacitor laminate as layer 2 and 3.*

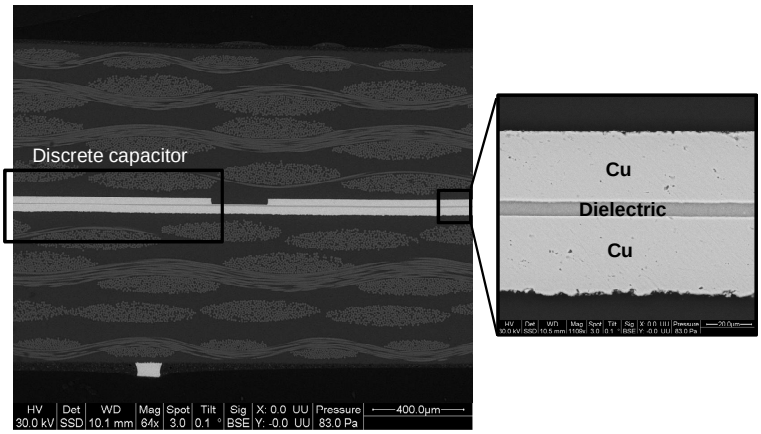


***Figure 3-3.*** *Sectional view of the test vehicle as observed through a scanning electron microscope (SEM).*

The dielectric was a composite of epoxy and $BaTiO_3$ and is shown in Figure 3-4. The mean diameter of $BaTiO_3$ particles was about 250 nm and $BaTiO_3$ particles were loaded 45% by volume in the epoxy matrix. The dielectric constant and dissipation factor of this composite was 16 and 0.005 respectively at 1 kHz.

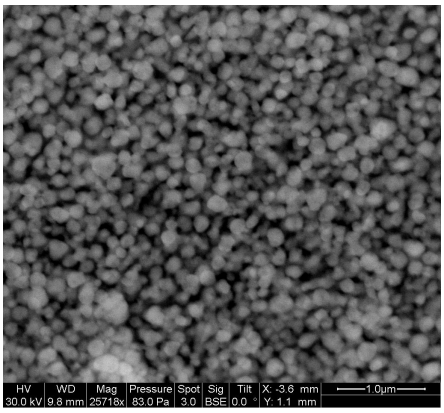


***Figure 3-4.*** *Magnified view of the epoxy-$BaTiO_3$ composite dielectric as observed through a scanning electron microscope.*

Embedded capacitors of two different dielectric thicknesses (C-Ply with 8 μm and 14 μm) are investigated in this study. Capacitors with different dielectric thicknesses were on different test vehicles. The test vehicle with capacitors of dielectric thickness 8 μm and 14 μm are termed as TV-1 and TV-2 respectively:

1. TV-1: C-Ply (8 μm).
2. TV-2: C-Ply (14 μm).

## *3.2 Test vehicle with a single embedded capacitor*

To further investigate the conduction mechanism in epoxy-$BaTiO_3$ composites, Cu/dielectric/Cu test structures were fabricated in our laboratory with varying $BaTiO_3$ loading and $BaTiO_3$ particle diameter. The $BaTiO_3$ loading was selected as 20%, 40%, and 60% by volume (keeping the particle diameter constant at 500 nm). The $BaTiO_3$ particle diameter was selected as 100 nm, 300 nm, and 500 nm (keeping the loading constant at 40% by volume). Various formulations of the dielectric material that were

prepared are shown as ‘x’ in Table 3-1. A control dielectric material was also made with 0% loading of $BaTiO_3$.

***Table 3-1.*** *Diameter and loading of barium titanate used to make the capacitors.*

| | | Particle diameter (nm) | | |
|---|---|---|---|---|
| | | 100 | 300 | 500 |
| Loading (Vol%) | 20 | | | x |
| | 40 | x | x | x |
| | 60 | | | x |

The dielectric paste was prepared using the colloidal process. The materials used to prepare the dielectric paste were:

- Ceramic : $BaTiO_3$
- Solvent: Propylene glycol methyl ether acetate (PGMEA)
- Dispersant: Phosphate ester
- Polymer : Bisphenol A diglycidyl ether
- Curing agent: Dicyandiamide (DICY)

The ratio of the dispersant to the ceramic was maintained at 2% by weight in the dielectric paste of all the samples. The ratio of curing agent to epoxy was maintained at 6% by weight in the dielectric paste of all the samples. The process steps for the preparation of dielectric paste have already been discussed in section 2.4. Ultrasonification was performed for 2 hrs using Cole-Parmer 8890 ultrasonic cleaning equipment as shown in Figure 3-5. Ball milling was performed in a rock tumbler as shown in Figure 3-6 using $ZrO_2$ grinding media (balls of 10 mm diameter) for 2 days.


***Figure 3-5.*** *Cole-Parmer 8890 ultrasonic cleaning equipment.*

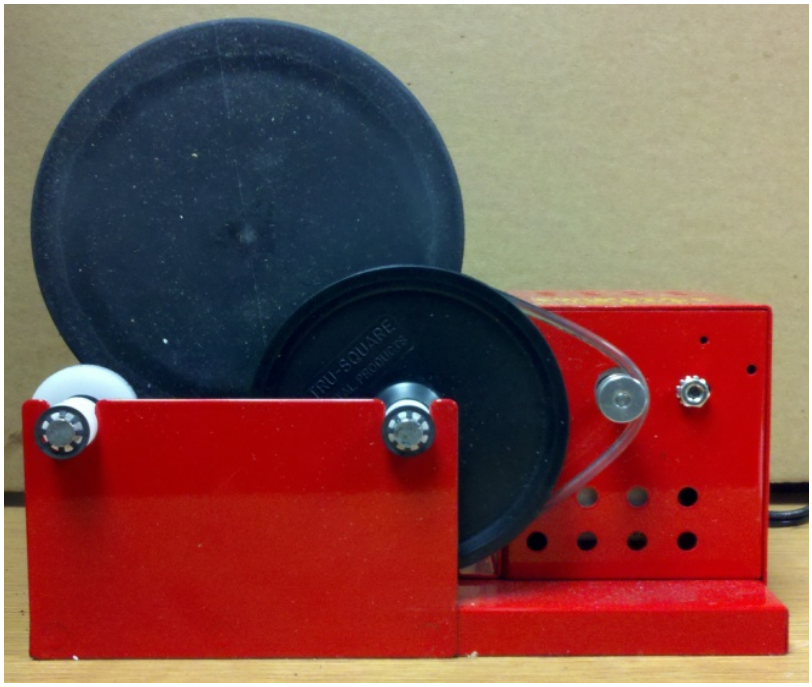

***Figure 3-6.*** *Rock tumbler with Zirconia ($ZrO_2$) grinding media (spherical balls of 10 mm diameter) used for ball milling.*

For each dielectric material three Cu/dielectric/Cu structures were fabricated. The dimensions of each capacitor were 40 mm × 40 mm. The top and the bottom Cu plates were made using polyimide based Cu laminates. The spacing between two plates of the capacitor was kept constant at 125 μm using polyimide based optical fibers (whose diameter was 125 μm) that acted as spacers. The process flow for the fabrication of the capacitors is shown in Figure 3-7.

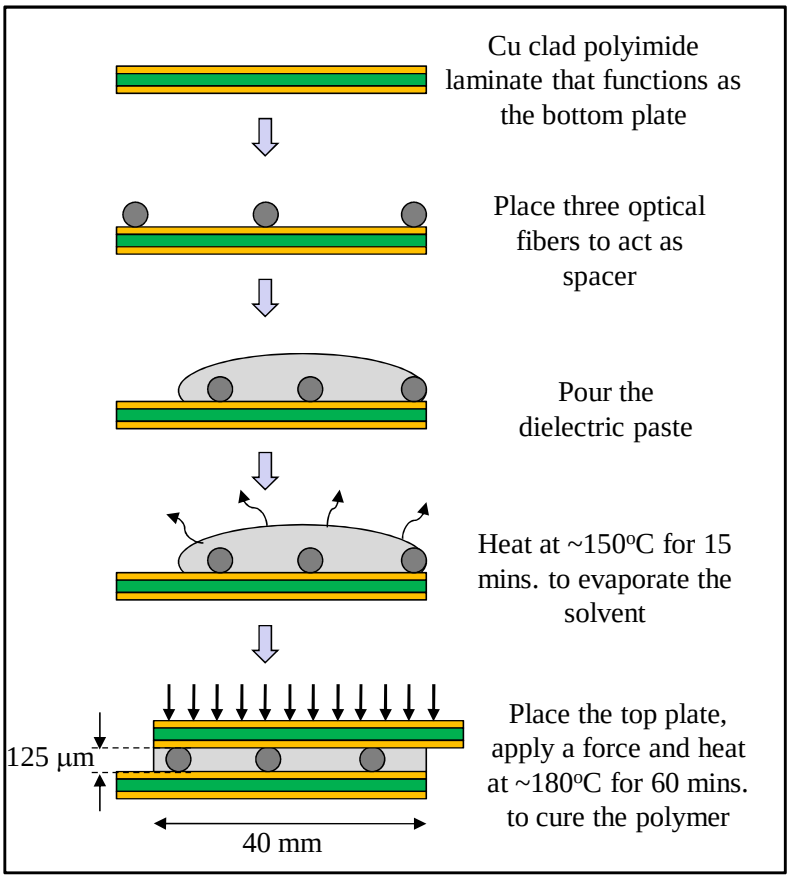


***Figure 3-7.*** *Process steps for the fabrication of Cu/dielectric/Cu structures.*

The boiling point of the solvent (PGMEA) was 146$^{o}$C so before placing the top laminate the structure was heated at 150$^{o}$C for 15 minutes to evaporate the solvent. The curing profile (180$^{o}$C for 1 hr) was selected after performing isothermal differential

scanning calorimetry (DSC) scans of the polymer (only with curing agent) at various temperatures. Isothermal DSC scans of the polymer (only with the curing agent) were performed at 160°C, 170°C, 180°C, and 190°C and are shown in Figure 3-8. It was observed that the polymer cured in about 60, 30, 20, and 15 minutes at 160°C, 170°C, 180°C, and 190°C respectively. Finally 180°C for 1 hr was selected as the curing conditions to ensure that the polymer cured completely.

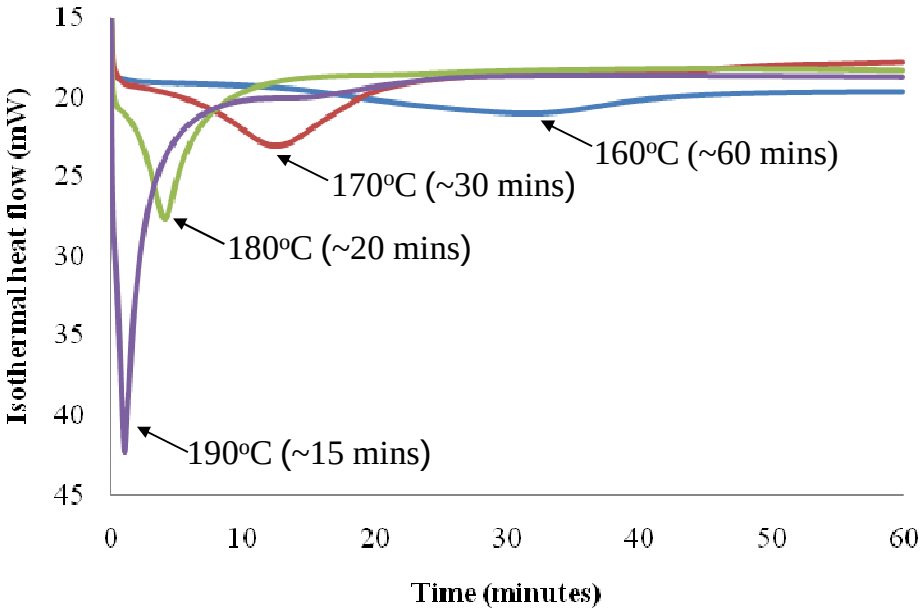


***Figure 3-8.*** *Isothermal differential scanning calorimetry (DSC) scans of the polymer (only with curing agent) at various temperatures.*

The final fabricated structure is shown in Figure 3-9. Cross sectional view of the fabricated capacitor is shown in Figure 3-10 for 0 % and 60 % loading by volume of $BaTiO_3$. A magnified view of the epoxy-$BaTiO_3$ composite dielectric at different loading conditions and different $BaTiO_3$ particle diameter is shown in Figure 3-11 and Figure 3-12.

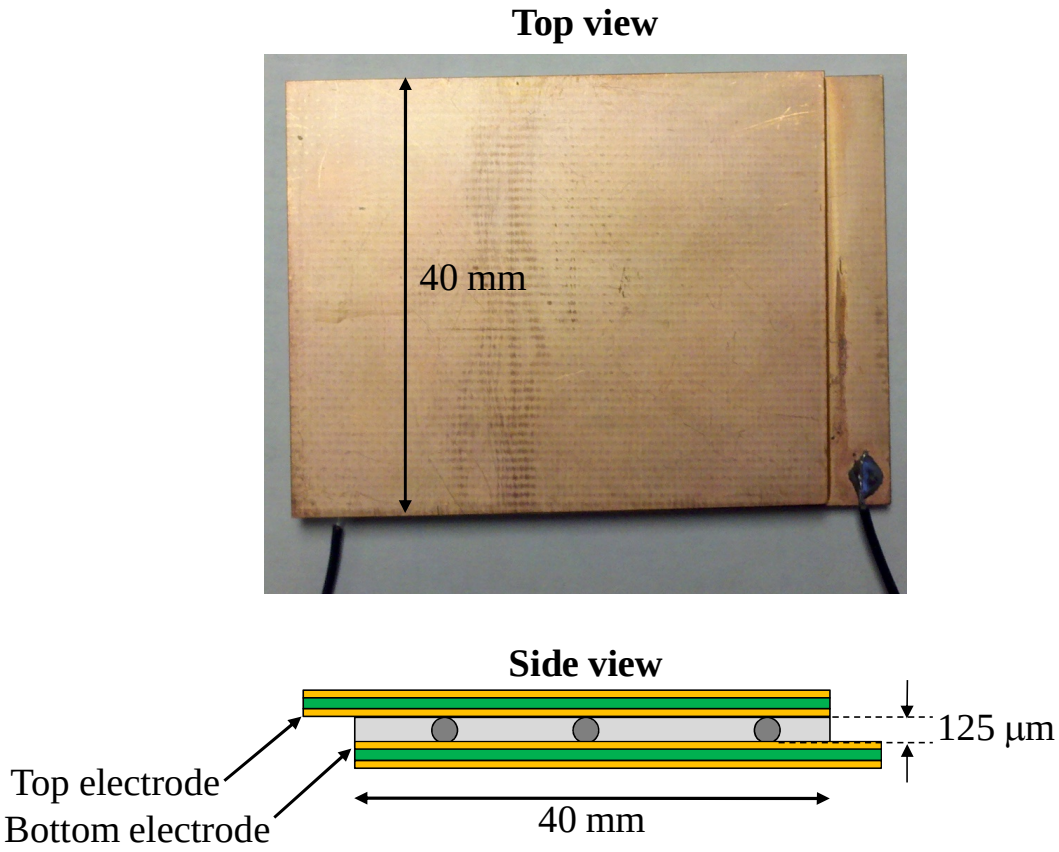


***Figure 3-9.*** *The fabricated Cu/dielectric/Cu structure.*

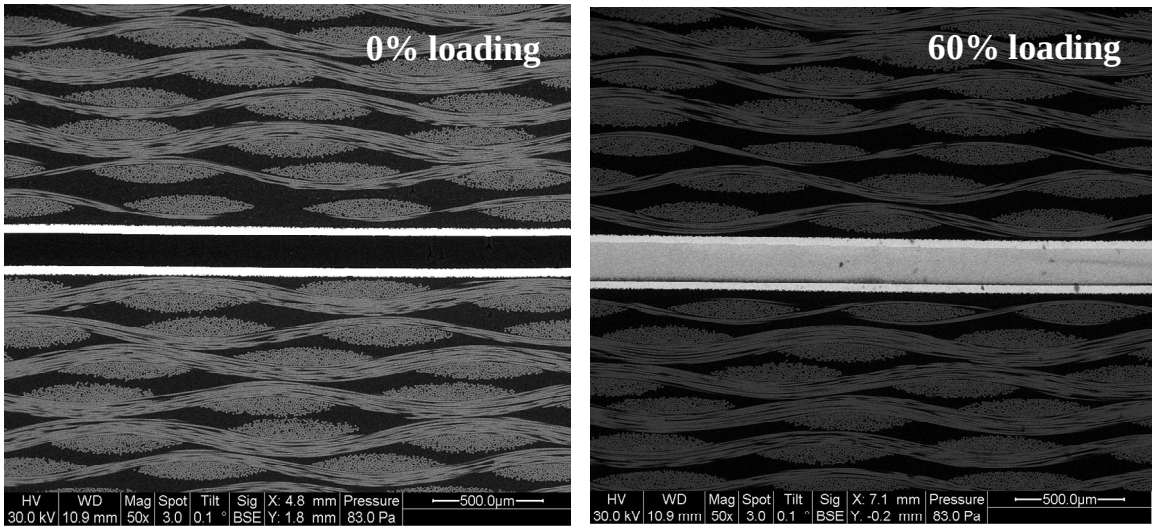


***Figure 3-10.*** *Cross sectional view of the capacitor (at 0% and 60% loading of $BaTiO_3$).*

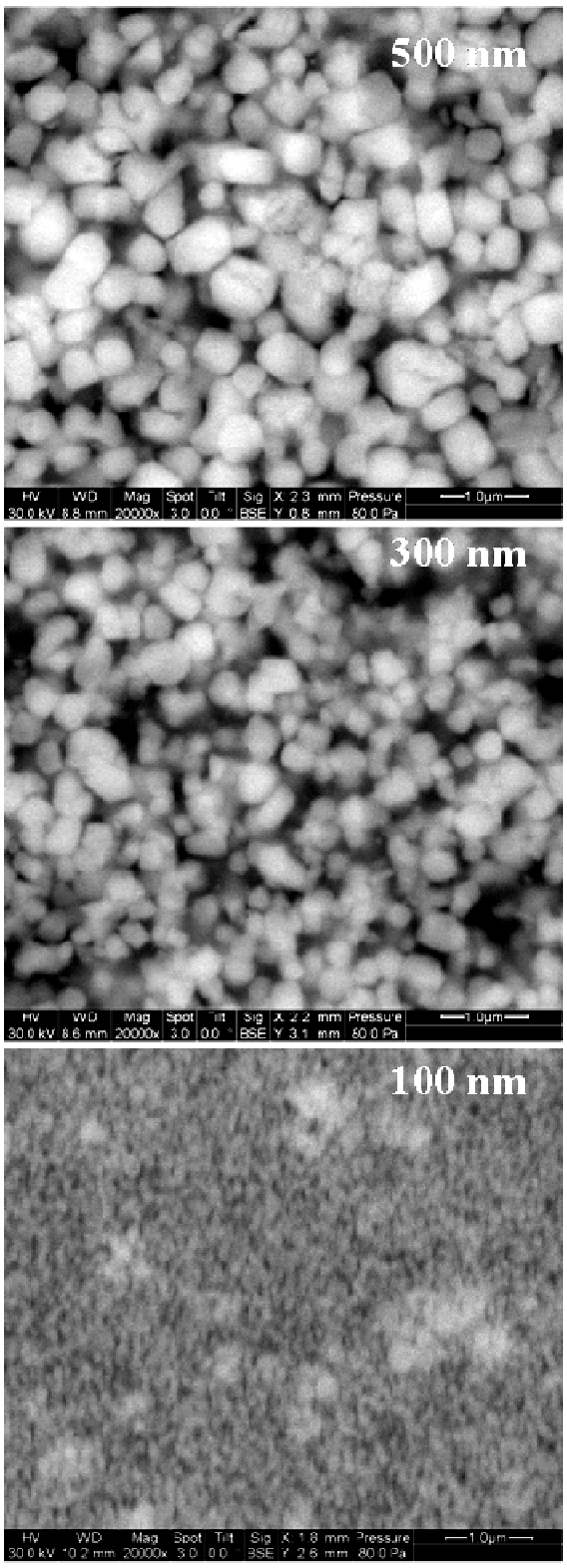


***Figure 3-11.*** *SEM view of the* ***c****omposite dielectric for* $BaTiO_3$ *particles of different diameter (at a loading of 40% by volume).*

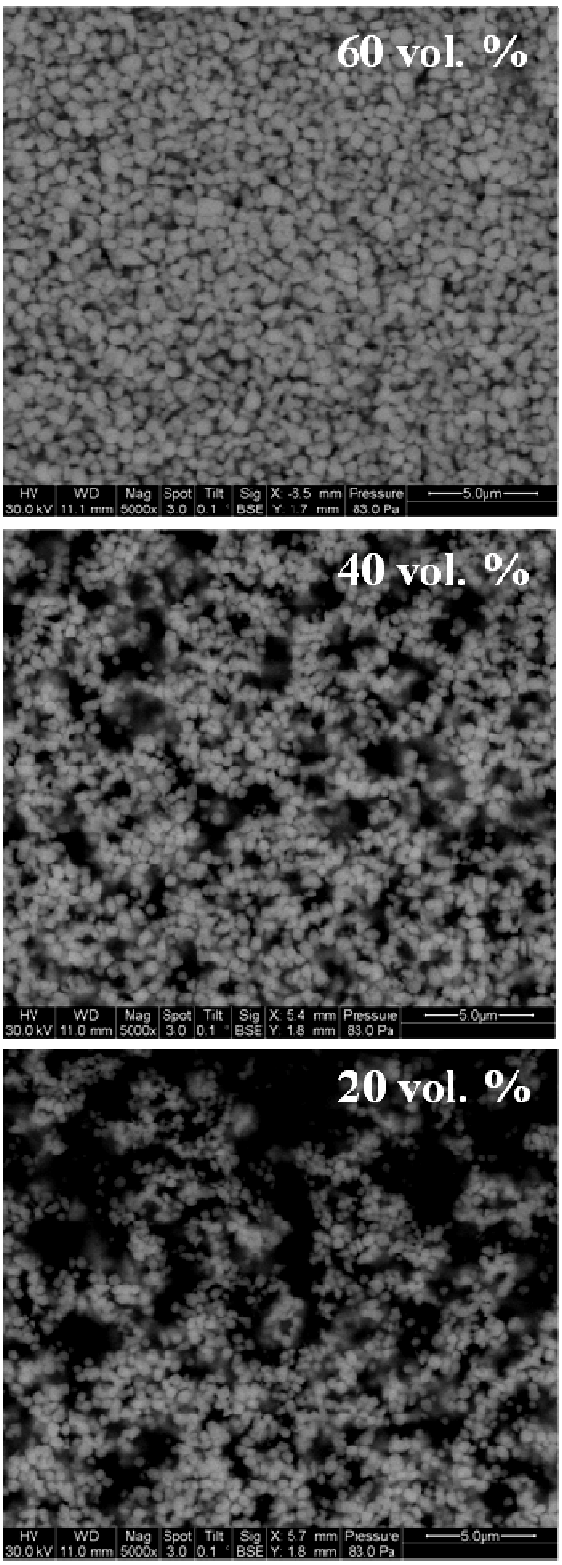


***Figure 3-12.*** *SEM view of the composite dielectric at different loading of $BaTiO_3$ particles (of diameter 500 nm).*

Measurements of dielectric thickness were performed in 2 out of 3 capacitors for each material set. In each capacitor, 10 measurements were performed along the two sections (I and II) as shown in Figure 3-13. The values of dielectric thickness of all the capacitors are given in Table 3-2. The thickness of the control sample (0% loading) was found to be 149 ± 3.1 μm.

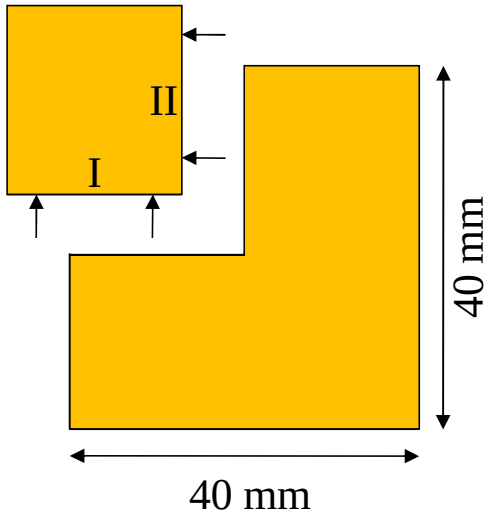


***Figure 3-13.*** *Measurements of dielectric thickness*

***Table 3-2.*** *Dielectric thickness of all capacitors*

| | | $BaTiO_3$ particle diameter (nm) | | |
|---|---|---|---|---|
| | | 100 | 300 | 500 |
| $BaTiO_3$ loading (Vol.%) | 20 | | | 163 ± 3.1 |
| | 40 | 156 ± 5.9 | 163 ± 2.7 | 166 ± 4.2 |
| | 60 | | | 163 ± 2.6 |

# 4. Electrical characterization of the test vehicle

## *4.1 Test vehicle with multiple embedded capacitors*

Capacitance and dissipation factor of 3 small capacitors (group A) from TV-1 were measured using an LCR meter. The measurements were performed at 100 kHz and at temperatures between 25$^{o}$ C to 125$^{o}$ C in steps of 25$^{o}$ C. The mean values of capacitance and dissipation factor as a function of temperature is shown in Figure 4-1 and Figure 4-2 respectively. The temperature coefficient of capacitance was found to be 743 ppm/$^{o}$C.

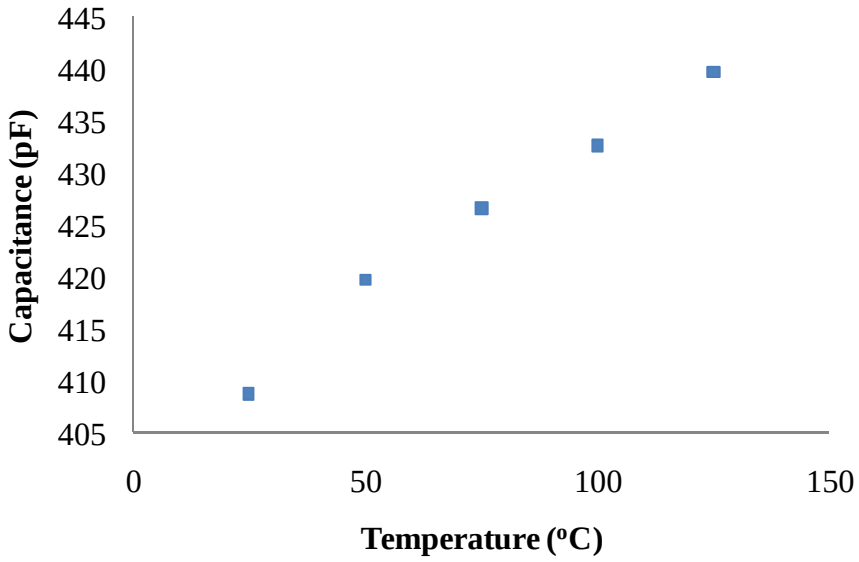


***Figure 4-1.*** *Effect of temperature on capacitance (of TV-1 with 8 μm dielectric thickness).*

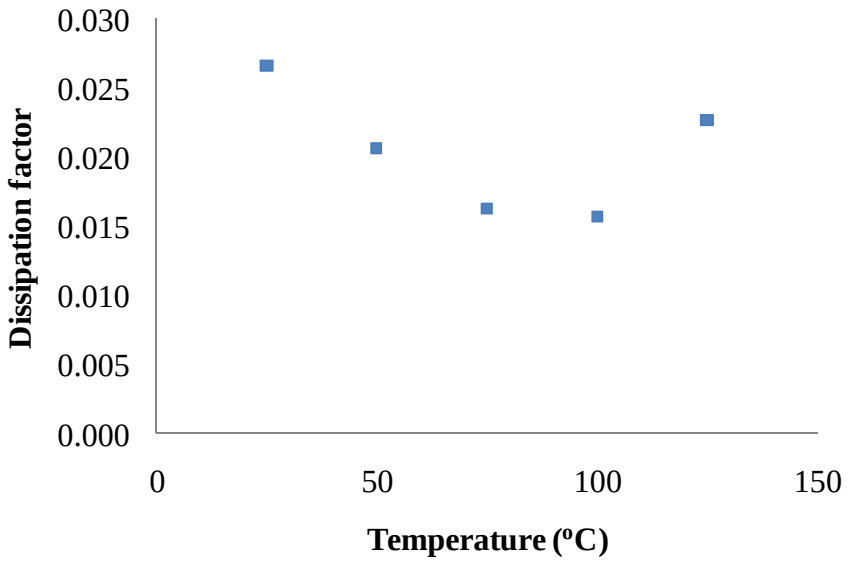


***Figure 4-2.*** *Effect of temperature on dissipation factor (of TV-1 with 8 μm dielectric thickness).*

## *4.2 Test vehicle with a single embedded capacitor*

The effective dielectric constant of the composite material was calculated by measuring the value of capacitance using an LCR meter at 100 kHz and 25° C. The mean values of the effective dielectric constant are presented in this work. The effective dielectric constant ($\varepsilon_{eq}$) of the composite was found to increase with an increase in the $BaTiO_3$ loading as shown in Figure 4-3. The maximum effective dielectric constant was close to 30 at 60% loading (for 500 nm $BaTiO_3$ particles). The effective dielectric constant was found to follow the well known Lichtenecker equation (as shown in Figure 4-3) which is given by [66]:

$$\log \varepsilon_{eq} = \nu \log \varepsilon_c + (1-\nu)\log \varepsilon_p \tag{8}$$

where $\varepsilon_c$ is the dielectric constant of ceramic, $\varepsilon_p$ is the dielectric constant of polymer, and $\nu$ is the loading fraction of ceramic by volume. The goodness of fit of the experimental

data with the Lichtenecker equation was found to be 0.97. Using regression analysis the dielectric constant of $BaTiO_3$ was found to be 137.

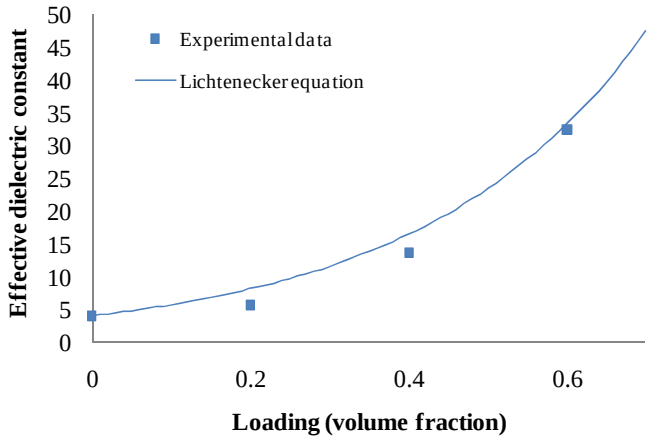


***Figure 4-3.*** *Effective dielectric constant versus $BaTiO_3$ loading: experimental data and Lichtenecker equation (for $BaTiO_3$ particles of 500 nm diameter).*

The effective dielectric constant ($\varepsilon_{eq}$) was found to decrease when the $BaTiO_3$ particle diameter was reduced to 100 nm as shown in Figure 4-4. This may be due to an increase in the agglomeration of $BaTiO_3$ particles at nanometric dimensions. Further the dielectric constant of $BaTiO_3$ is minimum when the particle size is close to 60 nm and that can also be a reason for this behavior [67].

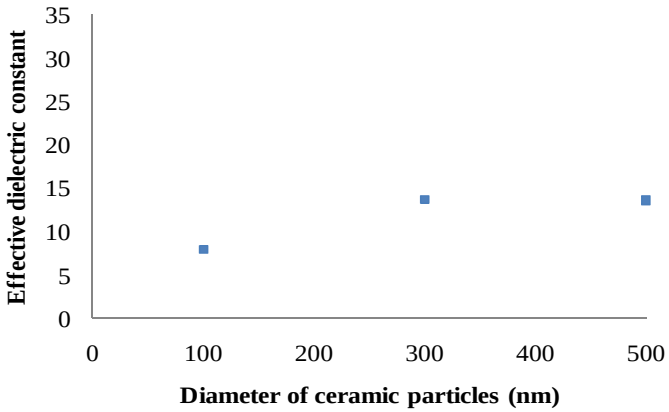


***Figure 4-4.*** *Effective dielectric constant of the composite versus diameter of $BaTiO_3$ particles (for 40% loading by volume of $BaTiO_3$ particles).*

The effect of temperature on the capacitance was investigated for capacitors with different loading conditions. Capacitance was measured using an LCR meter at 100 kHz between 25°C and 125°C in steps of 10°C. The effect of temperature on capacitance for capacitors with different loading conditions is shown in Figure 4-5 and Figure 4-6. Capacitance was found to increase linearly with temperature for all the capacitors.

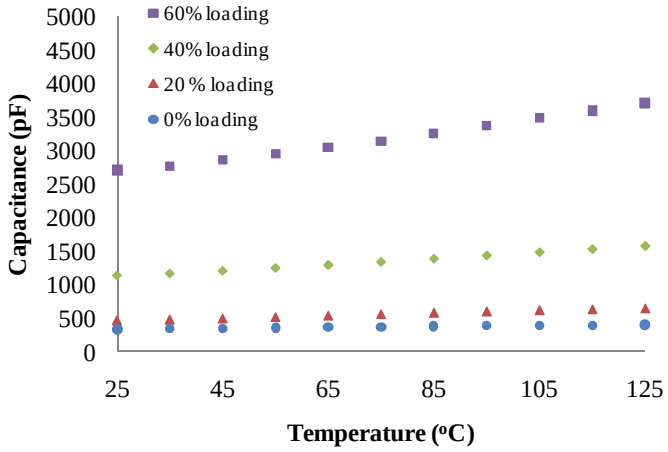


***Figure 4-5.*** *Effect of temperature on capacitance at different loading conditions (vol. %) of $BaTiO_3$ in the composite (for $BaTiO_3$ particles of 500 nm diameter).*

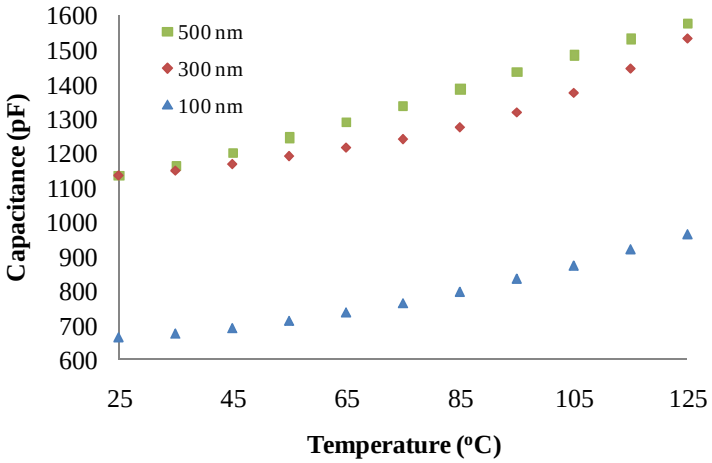


***Figure 4-6.*** *Effect of temperature on capacitance for $BaTiO_3$ particles of different diameters in the composite (at 40% loading by volume of $BaTiO_3$ particles).*

The temperature coefficient of capacitance (TCC) of the capacitors was measured between 25°C and 125°C (at 100 kHz). It was observed that the TCC of the capacitor with nanocomposite dielectric was higher than the capacitor with pure polymer dielectric. But there was no effect of loading (20, 40, and 60%) in the nanocomposite dielectric on TCC as shown in Figure 4-7. Further there was no clear trend on TCC with variation in the diameter of ceramic particles as shown in Figure 4-8.

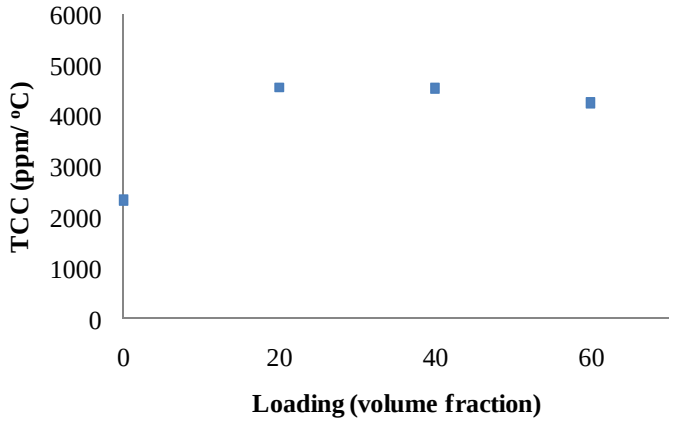


***Figure 4-7.*** *Temperature coefficient of capacitance (TCC) at different loading conditions (vol. %) of $BaTiO_3$ in the composite (for $BaTiO_3$ particles of 500 nm diameter).*

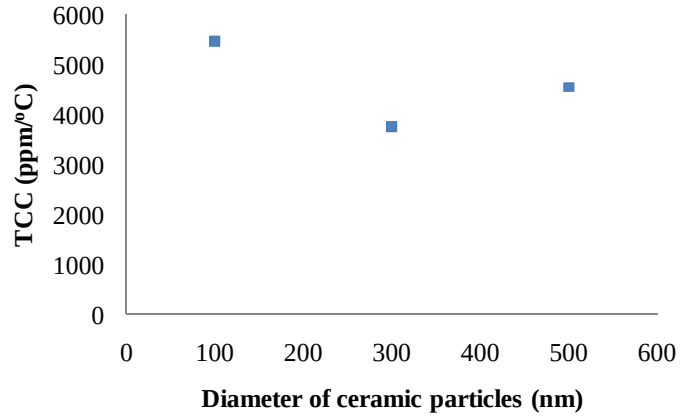


***Figure 4-8.*** *Temperature coefficient of capacitance (TCC) for $BaTiO_3$ particles of different diameter in the composite (at 40% loading by volume of $BaTiO_3$ particles).*

The effect of temperature on the dissipation factor was also investigated. Dissipation factor of all the capacitors was measured using an LCR meter at 100 kHz between 25°C and 125°C in steps of 10°C. Dissipation factor was found to increase with an increase in the temperature an increase in the loading of $BaTiO_3$ particles as shown in Figure 4-9. There was no clear trend in the values of dissipation with a change in the diameter of ceramic particles as shown in Figure 4-10.

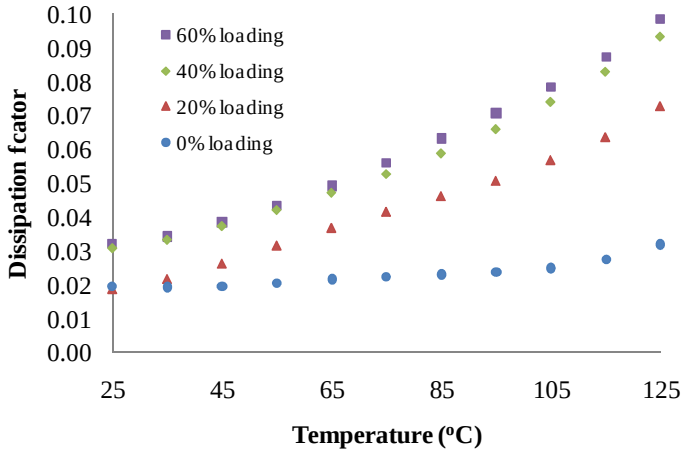


***Figure 4-9.*** *Effect of temperature on dissipation factor at different loading conditions (vol. %) of $BaTiO_3$ in the composite (for $BaTiO_3$ particles of 500 nm diameter).*

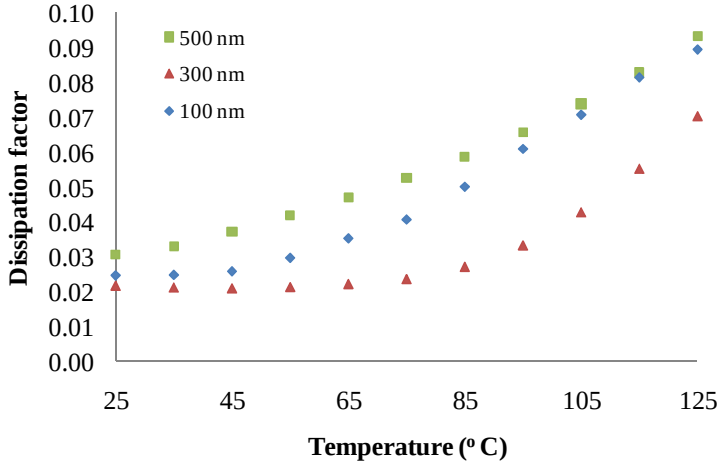


***Figure 4-10.*** *Effect of temperature on dissipation factor for $BaTiO_3$ particles of different diameter in the composite (at 40% loading by volume of $BaTiO_3$ particles).*

# 5. Temperature-humidity-bias (THB) test

## *5.1 Experimental setup*

A setup was designed for biasing the capacitors and measuring their electrical parameters during THB test. Thirty-six out of 80 capacitors of Group A and 4 out of 6 capacitors of Group B were randomly from TV-1 (with 8 μm dielectric thickness) selected for reliability investigation. In this work, three parameters-capacitance, dissipation factor, and insulation resistance were measured in-situ every hour for all capacitors. The capacitance and dissipation factors were measured by an Agilent 4263B LCR meter at 100 KHz. Insulation resistances were measured by an Agilent 4339B high resistance meter (by applying a bias of 10 V) and also by Agilent 34980A measuring unit. The switching of individual capacitor channels for measurements was performed by an Agilent 34980A switching unit. Two test vehicles were used for the THB test. One test vehicle was unbiased and the other test vehicle was biased at 5 V. Both of these test vehicles were kept in an environmental chamber maintained at 85$^{o}$C and 85%RH.

The test vehicles were preconditioned at 105$^{o}$C for 48 hours to remove the absorbed moisture. These conditions were established by performing some preconditioning experiments. During these experiments, the weight of one PWB and the dissipation factor of 5 small capacitors were monitored every day during baking at 105$^{o}$C. The weight of the PWB and the dissipation factor during baking is shown in Figure 5-1 and Figure 5-2 respectively. The experimental data implies that a suitable condition for preconditioning is 48 hrs at 105$^{o}$C.

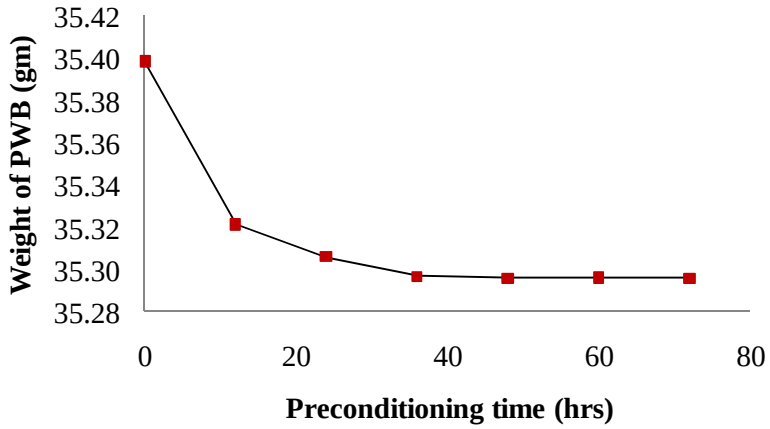


***Figure 5-1.*** *Weight of one PWB while baking at 105 $^{o}$C.*

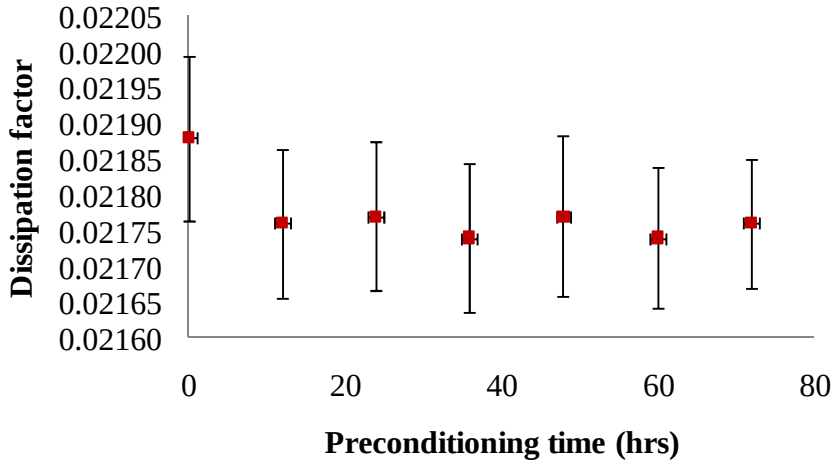


***Figure 5-2.*** *Dissipation factor while baking at 105 $^{o}$C.*

A series resistor of resistance 1.1 MΩ was connected in series to each capacitor to limit the current in the dielectric as shown in Figure 5-3. The failure criteria selected were: a 20% decrease in capacitance, an increase in dissipation factor by a factor of 2, or a drop in insulation resistance below 1.1 MΩ. The insulation resistance failure criterion

of 1.1 MΩ was the resistance of the series resistor connected to each capacitor. A schematic of the setup is shown in Figure 5-4.

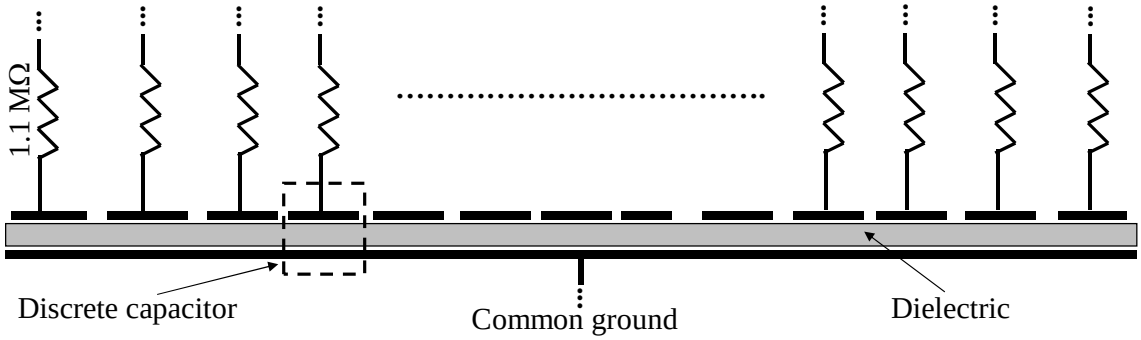


***Figure 5-3.*** *Schematic of the test vehicle with resistors of resistance 1.1 MΩ added in series to each capacitor.*

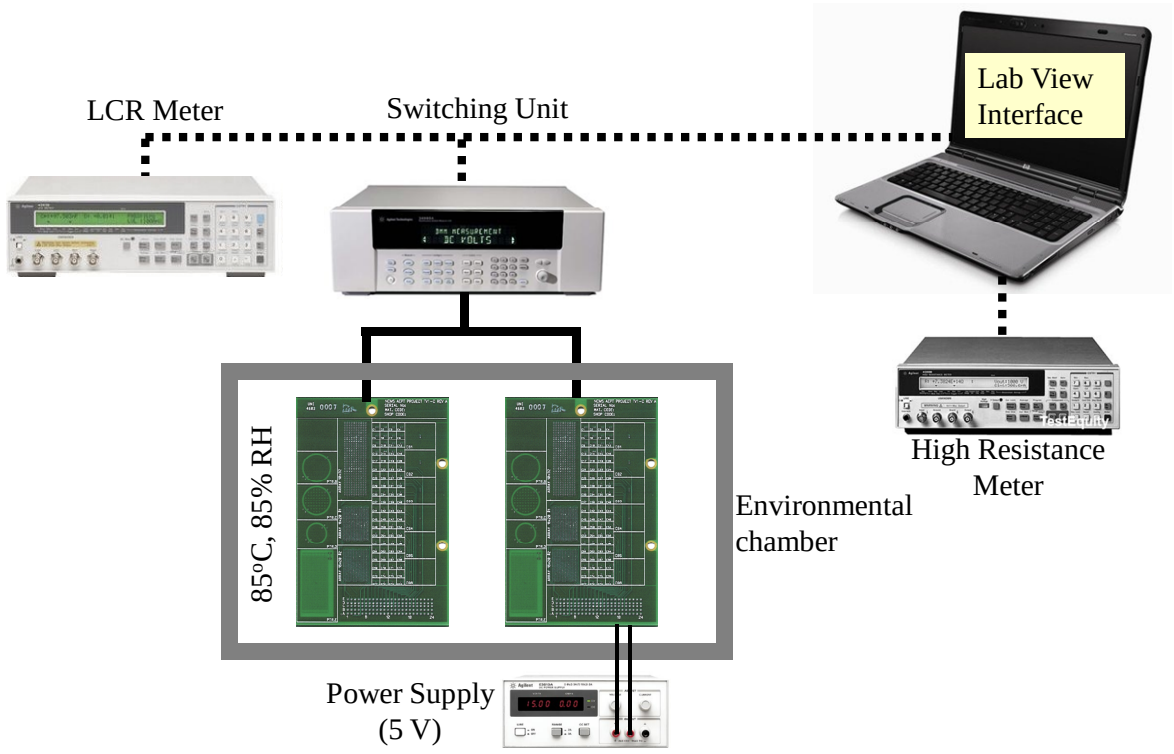


***Figure 5-4.*** *Schematic of the experimental setup used for the temperature-humidity-bias (THB) tests.*

## *5.2 Observations during THB test*

THB test continued for 2000 hours, and capacitance and dissipation factor were observed to increase as expected due to moisture absorption in the dielectric. Failures as a result of a sharp drop in insulation resistance and sharp increase in dissipation factor were observed in the test vehicle that was biased at 5 V. These failure modes were the result of the same physical phenomenon, i.e. the formation of a conducting path through the dielectric.

### 5.2.1 Behavior of capacitance

The capacitance was observed to increase as expected in both groups of capacitors. It was also observed that the increase in capacitance stabilized within 100 hours in small (Group A) capacitors. In large (Group B) capacitors the capacitance did not stabilize even within 2000 hours. Typical plots of the capacitance of small and large capacitors are shown in Figure 5-5 and Figure 5-6, respectively. The average increase in capacitance after 2000 hours at 85$^{o}$C and 85% RH for small and large capacitors was found to be 19.6±1.3 % and 22.6±0.2 %, respectively. Analysis of increase in capacitance was not carried out for the test board that was biased at 5 V because after failures the value of the capacitance started to fluctuate.

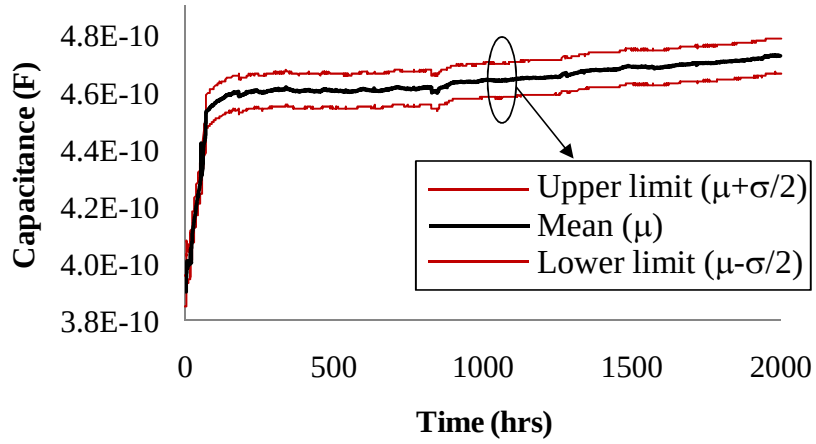


***Figure 5-5.*** *Capacitance of small (group A) capacitors at 85 $^{o}$C and 85% RH.*

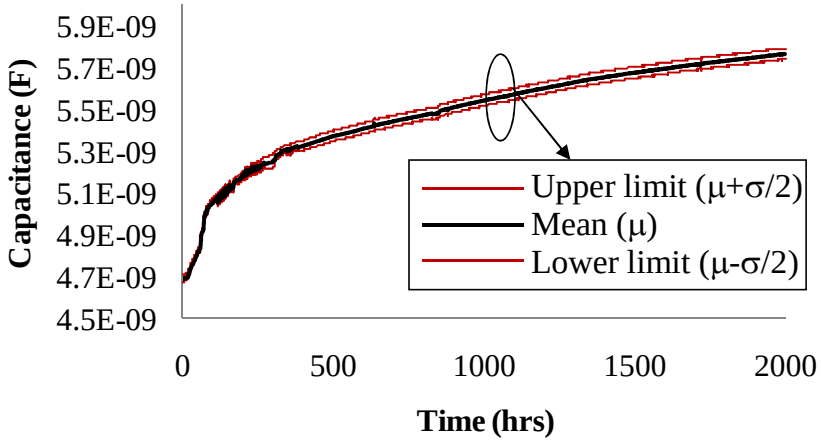


***Figure 5-6.*** *Capacitance of large (group B) capacitors at 85 $^{o}$C and 85% RH.*

## 5.2.2 Behavior of dissipation factor

The value of the dissipation factor was also found to increase. The behavior of the dissipation factor was found to be similar to the capacitance for both groups of capacitors. A plot of dissipation factor versus time for Group A and Group B capacitors is shown in Figure 5-7 and Figure 5-8. The average increase in dissipation factor after 2000

hours at 85°C and 85% RH for small and large capacitors was found to be 21.2±1.1 % and 24.2±0.2 %, respectively.

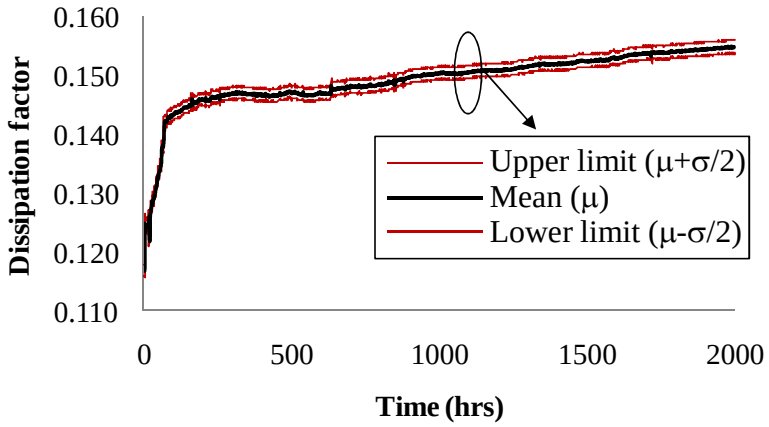


***Figure 5-7.*** *Dissipation factor of small (group A) capacitors at 85 °C and 85% RH.*

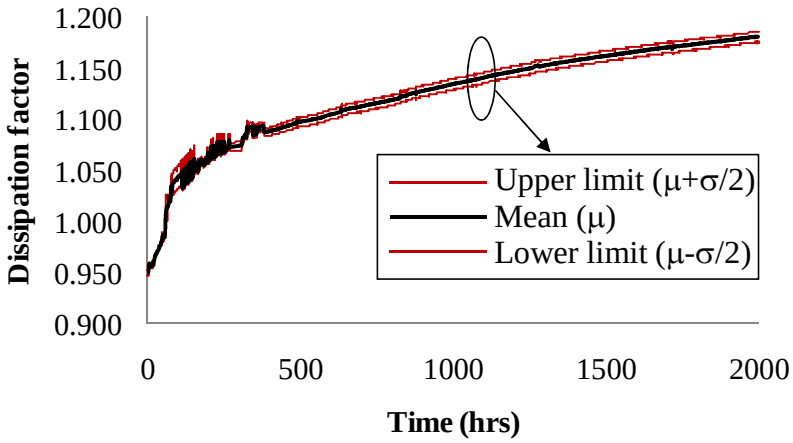


***Figure 5-8.*** *Dissipation factor of large (group A) capacitors at 85°C and 85% RH.*

A similarity in the plot of capacitance and dissipation factor during temperature and humidity tests implies that the cause of an increase in the dissipation factor is also moisture absorption in the dielectric. To show that the values of capacitance and dissipation factor comes from the same distribution, a Q-Q plot between capacitance and dissipation factor during 2000 hours of test is drawn. Q-Q plot is a probability plot, which

is a graphical method for comparing two probability distributions by plotting their quantiles against each other. If the two distributions being compared are similar, the points in the Q-Q plot will approximately lie on the line $y = x$. If the distributions are linearly related, the points in the Q-Q plot will approximately lie on a line, but not necessarily on the line $y = x$. In Figure 5-9 the Q-Q plot is shown for small (Group A) capacitors in which the data points are always close to the $45^{o}$ line except the initial few points implying that both data come from the same distribution. The values of correlation coefficient between capacitance and dissipation factor for small (Group A) and large (Group B) capacitors were found to be $0.77 \pm 0.14$ and $0.94 \pm 0.02$ respectively.

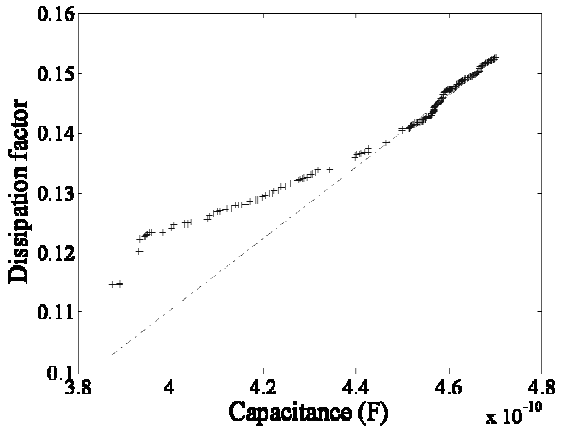


***Figure 5-9.*** *Q-Q plot between capacitance and dissipation factor for one small (group A) capacitor at 85 $^{o}$C and 85% RH.*

## 5.2.3 Behavior of insulation resistance

Failures as a result of a sharp drop in insulation resistance were only observed in the test board that was biased at 5 V. Six out of 36 small (Group A) capacitors and 2 out of 4 large (Group B) capacitors failed by this failure mode. A typical plot of the insulation resistance of a failed capacitor during $85^{o}$C, 85% RH, and 5 V is shown in Figure 5-10. In all the failed capacitors many intermittent failures were observed.

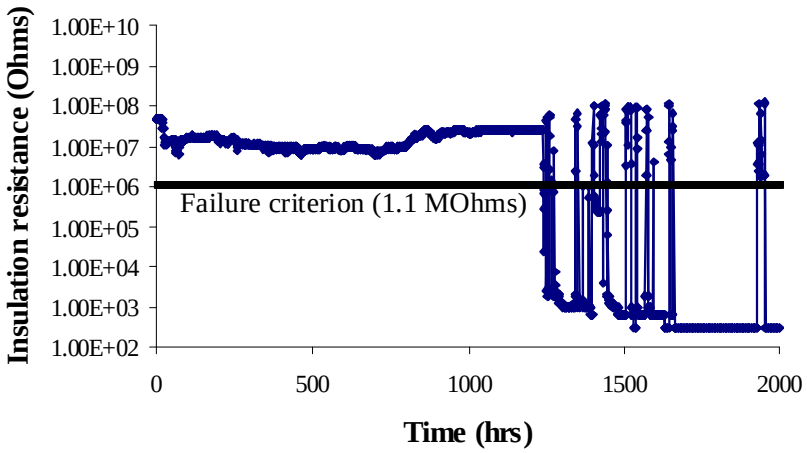


***Figure 5-10.*** *Failures as a result of a drop in the insulation resistance observed at 85 $^{o}$C, 85% RH, and 5 V (for one small capacitor).*

Statistical analysis was performed on the time-to-failure data of small (Group A) capacitors using Weibull software. A Weibull 3-parameter distribution was fitted to the time-to-failure data as shown in Figure 5-11. The parameters of the Weibull 3-parameter distribution $\beta$ (shape parameter), $\eta$ (scale parameter) and $\gamma$ (failure free operating period) were found to be 1.2, 3904, and 217 respectively. The two failures in the large capacitors took place at 363 and 855 hours.

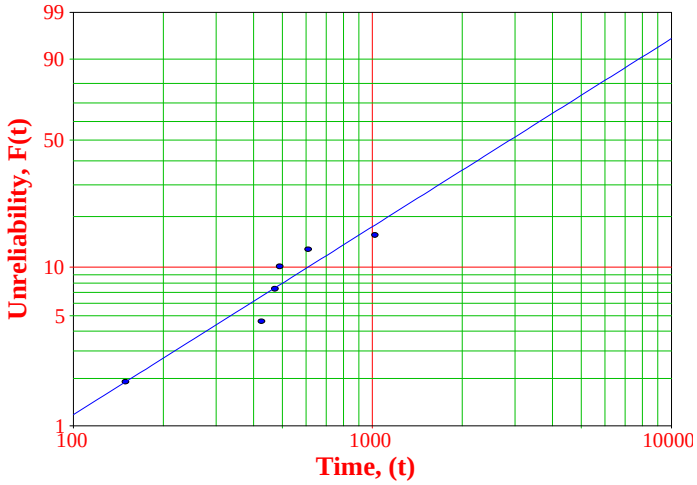


***Figure 5-11.*** *Unreliability versus time plot for small (group A) capacitors at 85 $^{o}$C, 85% RH, and 5 V.*

## 5.3 Observations during baking the board

After 2000 hours of test, both test vehicles were baked at 125$^{o}$C for 60 hours to investigate for reversibility in the changed electrical parameters. The capacitance and dissipation factors of both groups of capacitors were found to decrease during baking. The reversibility of capacitance and dissipation factors was investigated for the capacitors in the test vehicle that was stressed at 85$^{o}$C and 85% RH. Typical plots of relative capacitance and relative dissipation factors during baking at 125$^{o}$C are shown in Figure 5-12 and Figure 5-13 respectively. This plot shows the reversibility of moisture absorption phenomenon. The average decrease in the capacitance of small (Group A) and large (Group B) capacitors after 60 hours was found to be (24.2 ± 1.2) % and (27.5 ± 2.8) %, respectively. The average decrease in the dissipation factor of small (Group A) and large (Group B) capacitors after 60 hours was found to be 32.7 ± 0.9 % and 28.1 ± 2.7 %, respectively.

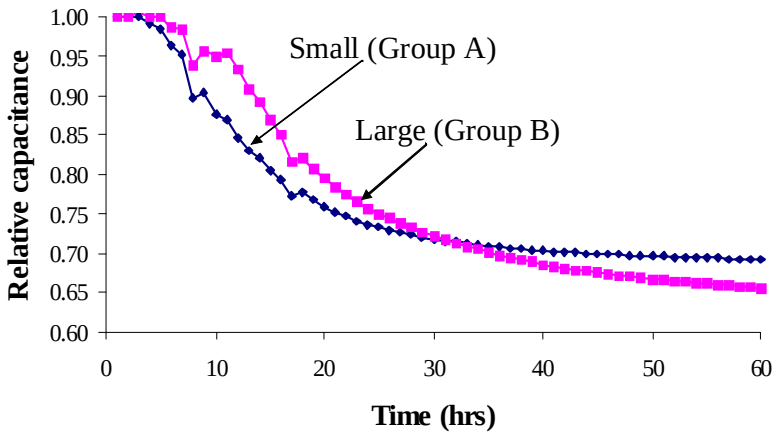


***Figure 5-12.*** *Relative capacitance of one small (group A) and large (group B) capacitor during baking at 125 $^{o}$C.*

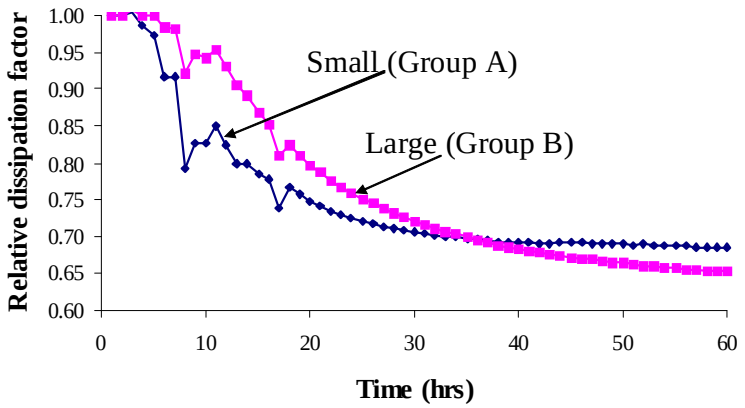


***Figure 5-13.*** *Relative dissipation factor of one small (group A) and large (group B) capacitor during baking at 125 $^{o}$C.*

The percentage change in capacitance and dissipation factor during temperature and humidity test (85$^{o}$C and 85% RH for 2000 hours) and during baking (125$^{o}$C for 60 hours) is summarized in Table 5-1. It can be observed that the increase in capacitance and dissipation factor was reversible during baking. However, the percentage increase and decrease cannot be compared strictly since they are measured at different temperatures (85$^{o}$C and 125$^{o}$C respectively), and the capacitance and dissipation factors are a function of temperature.

***Table 5-1.*** *Percentage change in capacitance and dissipation factor during THB test followed by baking.*

| | | 85$^{o}$C and 85% RH for 2000 hours | 125$^{o}$C for 60 hours |
|---|---|---|---|
| Capacitance | Group A | (19.6 ± 1.3) | -(24.2 ± 1.2) |
| | Group B | (22.6 ± 0.2) | -(27.5 ± 2.8) |
| Dissipation factor | Group A | (21.2 ± 1.1) | -(32.7 ± 0.9) |
| | Group B | (24.2 ± 0.2) | -(28.1 ± 2.7) |

A Q-Q plot of capacitance and dissipation factor during the baking of the board is shown in Figure 5-14 for small (group A) capacitors. The values of capacitance and dissipation factor are close to the $45^{o}$ line and imply that the data points come from the same distribution. The values of capacitance and dissipation factor were strongly correlated with each other, and the value of the correlation coefficient for small (group A) and large (Group B) capacitors was found to be $0.99 \pm 0.0$.

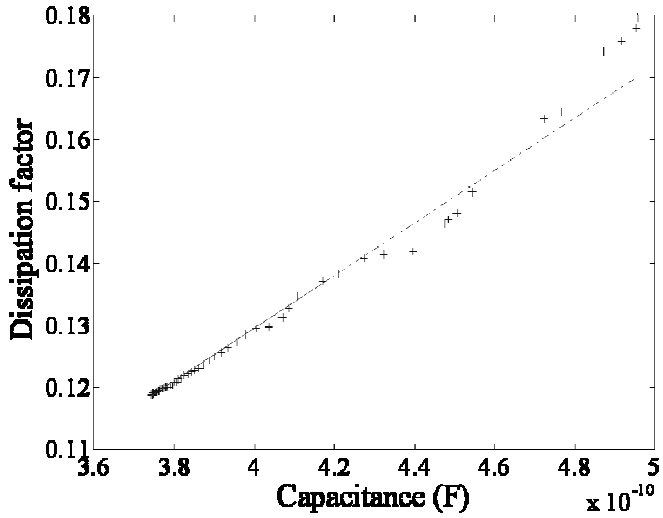


***Figure 5-14.*** *Q-Q plot between capacitance and dissipation factor for one small (group A) capacitor during baking at 125 $^{o}$C.*

The failure mode that was a sharp drop in the insulation resistance (observed at $85^{o}$C and 85% RH and 5V) was also found to be reversible. The insulation resistance of all the capacitors returned to a value above 1.1 MΩ during baking as shown in Figure 5-15.

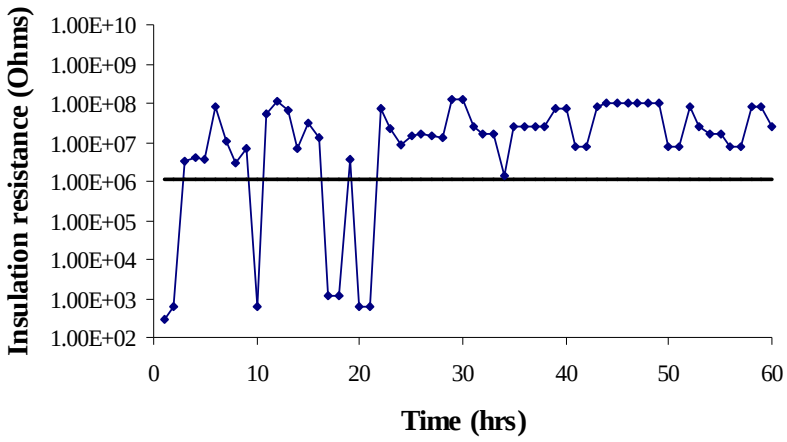


***Figure 5-15.*** *Disappearance of the insulation resistance failures during baking at 125 $^{o}C$ (for one small capacitor).*

## *5.4 Hypothesis of insulation resistance failures*

The disappearance of the failure signature during baking made it challenging to isolate and analyze the failure site. Hence the mechanism of failure is hypothesized by performing data analysis.

The value of $\beta$ (~1) and the disappearance of failures after ~ 50% of the test time (as shown in Figure 5-11) indicates that these failures are random in nature. These failures may be due to some defects in the dielectric such as porosity or void that can favor the formation of a conduction path under THB conditions. The percentage of failures in large capacitors (50%) was found to be more than that in small capacitors (17%). This further supports our hypothesis that these failures were driven by some defects in the dielectric whose number increases with the area of the capacitor. Other conditions required for the formation of this conductive path is moisture and an applied bias. Moisture is required since the insulation resistance failures disappeared after baking.

An applied bias is also required since these failures were only observed in the capacitors that were biased.

Defects such as porosity or voids, moisture, and applied bias can lead to the formation of a low resistance conducting path which is explained as follows (Hypothesis A in Figure 5-16). Defects act as a hollow region for the formation of the conducting path. The charge carriers are expected to be the ionic contaminants which are present in epoxy resin and on the surface of $BaTiO_3$. The absorbed moisture in the hollow region acts as a medium for the transport of charged carriers in the presence of a bias. Another possible low resistance path can be formed by the overlap of water shells of $BaTiO_3$ (Hypothesis A in Figure 5-16). Large number of intermittent failures (as shown in Figure 5-10) implies that the conduction path is not very stable.

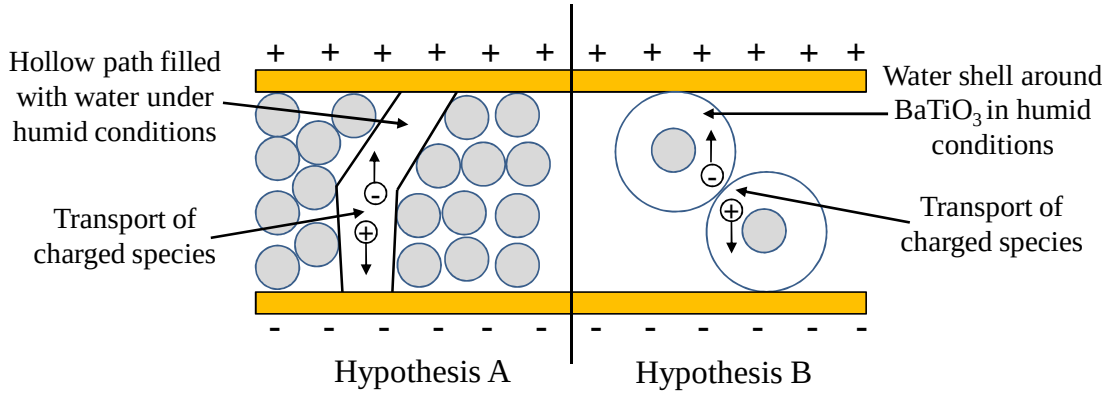


***Figure 5-16.*** *Possible low resistance path formed under THB conditions.*

In this work, the PWB was baked at 125°C to drive away the absorbed moisture. Since moisture absorption and desorption is taking place at different temperatures (85°C and 125°C respectively), temperature can also play a role in the disappearance of these failures. It is possible that the conduction path is simply destroyed due to a mismatch in the coefficient of thermal expansion of conduction path and the dielectric material. The

moisture desorption should be performed at the same temperature (at 85$^{o}$C), in order to eliminate the effect of temperature in the disappearance of these failures. Further, a bias reversal can also be performed after the THB test to see if these failures disappear.

## *5.5 Modeling the drift in electrical parameters*

Although moisture absorption is reversible, an increase in capacitance can affect the system (where these capacitors are used) for a period of time. In addition to capacitance, the dissipation factor of the dielectric was also found to increase under these conditions. Dissipation factor is a critical electrical parameter and is a measure of losses in the dielectric. In this work, the diffusion of moisture in the dielectric is also modeled using transient finite element method (FEM), and the changes in electrical parameters are calculated theoretically.

Since the behaviors of the capacitance and dissipation factor were similar, analysis was done only for an increase in the capacitance. The diffusion of moisture in the capacitor dielectric increased the dielectric constant of the dielectric (since the dielectric constant of water is ~78), and led to an increase in the capacitance. The path of moisture ingress in the capacitor is shown in Figure 5-17.

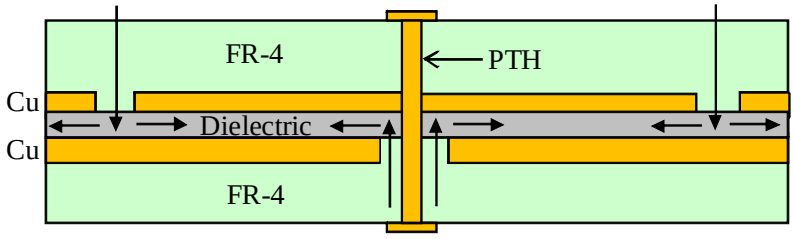


***Figure 5-17.*** *Path of moisture ingress in the capacitor dielectric.*

### 5.5.1 Assumptions and boundary conditions (B.C)

Moisture ingress in the capacitor dielectric takes place in two dimensions, *x* and *y* (assuming that the *z* axis is along the axis of the PTH). The concentration of moisture was assumed to be constant along the *z* axis in the dielectric. A 2D diffusion equation had to be solved which is given as:

$$\frac{\partial^2 c}{\partial x^2} + \frac{\partial^2 c}{\partial y^2} - \frac{1}{D}\frac{\partial c}{\partial t} = 0 \tag{9}$$

where *c* is the concentration of the moisture, *D* is the diffusion coefficient, and *t* is the time. A Dirichlet boundary condition (B.C.) was selected, which implies that the concentration of moisture was assumed to be constant along the edges of the capacitor, i.e., along all four edges and the circular antipads of the PTH, as shown in Figure 5-18 (top view of the capacitor). The moisture concentration at these edges was assumed to be equal to the saturation moisture concentration in the epoxy resin (used in FR-4) at 85$^{o}$C and 85% RH.

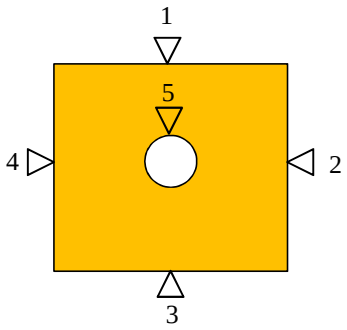


***Figure 5-18.*** *Dirichlet boundary condition on the five edges.*

Since the thickness of FR-4 above and below the capacitor was much less compared to the *x* and *y* dimensions of the capacitor, the time required for the FR-4 to become saturated with moisture was much less than the time required for the capacitor

dielectric to get saturated with moisture. Hence it was assumed that at the start of the elevated temperature and humidity test, FR-4 was saturated with moisture.

Some preliminary experiments were also performed to verify this assumption. Three samples of the test vehicle each 1 cm × 1 cm were exposed to 85$^{o}$C and 85% RH and their weight was monitored after every 24 hrs. It was observed that the time required for FR-4 to saturate with moisture was close to 80 hrs. This time is comparable to the time required for the capacitance of small capacitors to saturate (≈100 hrs) under these conditions. This implies that the assumption is not very convincing for small capacitors. But for large capacitors this assumption holds since the time required for FR-4 to saturate with moisture is very small as compared to the time required for the capacitance of large capacitors to saturate under these conditions (> 2000 hrs). In this work, the moisture diffusion in FR-4 was assumed to be valid for both sizes of capacitors in order to simplify the computation.

A more scientific way of modeling diffusion in this structure is by considering the diffusion of moisture in FR-4 also. If we carefully observe the whole process, we see that the diffusion of moisture in the capacitor dielectric is taking place at all times (even before the saturation of FR-4 with moisture). It implies that the boundary condition is not a constant. The concentration of moisture at the boundary is also increasing and getting saturated as the FR-4 is getting saturated with moisture.

The numerical value of the B.C. was calculated by performing moisture absorption and decomposition experiments. Three samples of the test vehicle each 1 cm × 1 cm were exposed to 85$^{o}$C and 85% RH and their weight was monitored after every 24

hrs. The saturated weight of moisture in these samples (epoxy + Cu + glass fibers) was found to be 0.59% by weight. It was assumed that all the moisture absorbed was contained in epoxy resin. The saturated weight of moisture in epoxy was obtained by deducting the weight of Cu plates and glass fibers in these samples. The weight of Cu plate was obtained by measuring the dimensions of the Cu plate. The weight of glass fibers was obtained by measuring the weight of these samples before and after the decomposition experiment. In decomposition experiments, three similar samples (1 cm × 1 cm ) were heated to 550$^{o}$C for 90 minutes to burn off the epoxy resin (leaving behind Cu and glass fibers). By deducting the weight of Cu and glass fibers, the saturation moisture content in epoxy was found to be 1.24% by weight or 14.98 kgm$^{-3}$.

Corresponding to a change in the concentration of moisture, there was a change in the dielectric constant of the nanocomposite dielectric. It has been observed that the moisture content in a board laminate is linearly related to the change in capacitance [68] and hence a linear model was selected. This linear model relates the concentration of moisture ($c$) to the effective dielectric constant of the composite ($\varepsilon_{eff}$) and is given by:

$$\varepsilon_{eff}(x, y, t) = 16 + \frac{c(x, y, t)}{A} \tag{10}$$

where 16 is the original dielectric constant of the nanocomposite and $A$ is a constant whose value has to be computed.

### 5.5.2 Methodology

To solve the above diffusion problem the values of the constants $D$ and $A$ have to be known. The value of $D$ can be easily calculated by measuring the weight gain in a thin plate (x, y >> z) of dielectric material over time and then applying the 1D Fick's law of

diffusion. However, in this work, there was no access to the dielectric material. In this work another methodology is proposed which can be used to calculate the values of $D$ and $A$ in complex capacitor structures embedded in a PWB.

This methodology was first implemented on group A capacitors. In the first step of this methodology some realistic values of $D$ and $A$ was chosen. Then a 2D FEM model of group A capacitor was made in Abaqus which is shown in Figure 5-19. This model had 2104 quadrilateral elements. The type of element was a 4 node heat transfer element (DC2D4) and a transient analysis was performed. After solving equation (1) using Abaqus, the concentration of moisture at the centroid of each element as a function of time, $c(x,y,t)$ was determined. Using equation (2), the effective dielectric constant of each element as a function of time, $\varepsilon_{eff}(x,y,t)$ was calculated. The theoretical capacitance of the capacitor as a function of time was calculated by summing the capacitances of all the elements in parallel using the following equation:

$$C^{theo}(t) = \sum_{i=1}^{2104} \frac{\varepsilon_{eff}(x_i, y_i, t)\varepsilon_o A_i}{d} \tag{11}$$

where $\varepsilon_o$ is the permittivity of free space, $A_i$ is the area of the $i^{th}$ element, and $d$ is the spacing between the capacitor plates. A dimensional change in the dielectric thickness due to hygroscopic swelling was assumed to be zero.

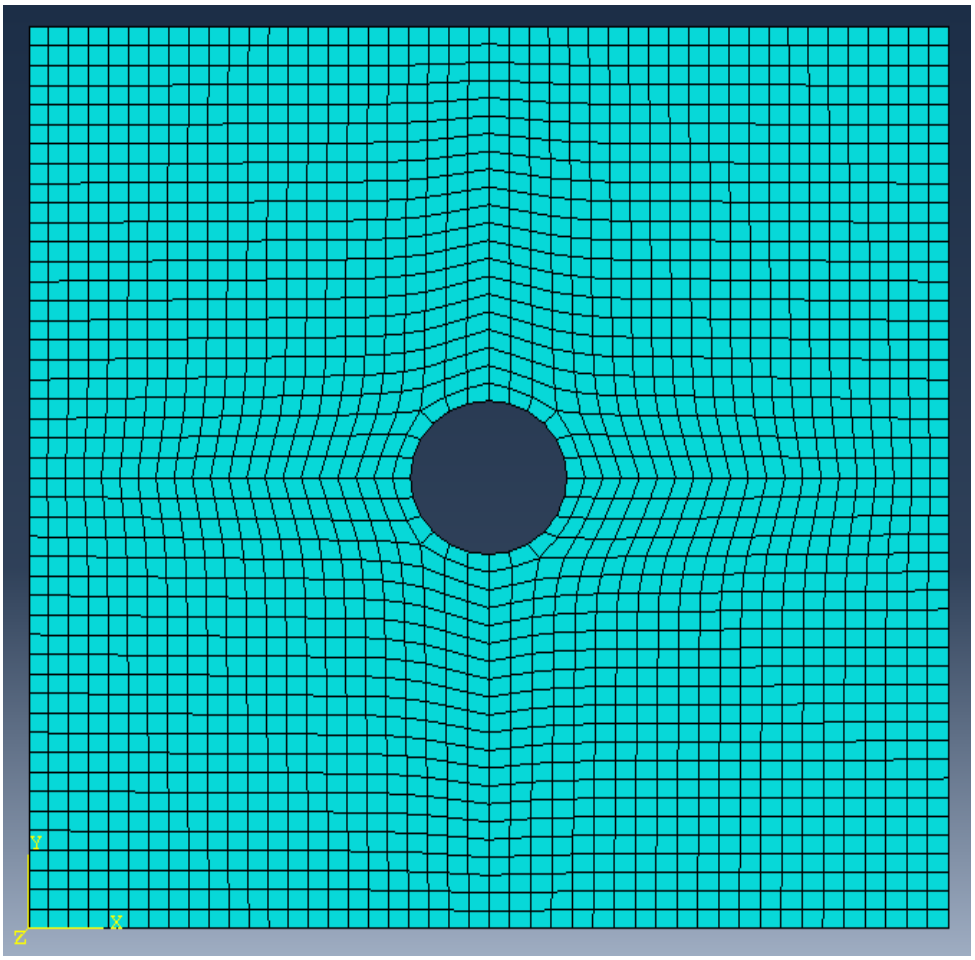


***Figure 5-19.*** *FEM model of group A capacitor.*

The last step of the methodology was to minimize the root mean square errors between the theoretical plot ($C^{theo}$) and the experimental plot ($C^{exp}$) at equally divided 2000 points along the time axis. The values of $D$ and $A$ were obtained by minimizing the function ($f$) in equation (4). The entire methodology is shown in Figure 5-20.

$$f = \min\left(\sqrt{\frac{\sum_{i=1}^{2000}\left(C_i^{theo} - C_i^{\exp}\right)^2}{2000}}\right) \tag{12}$$

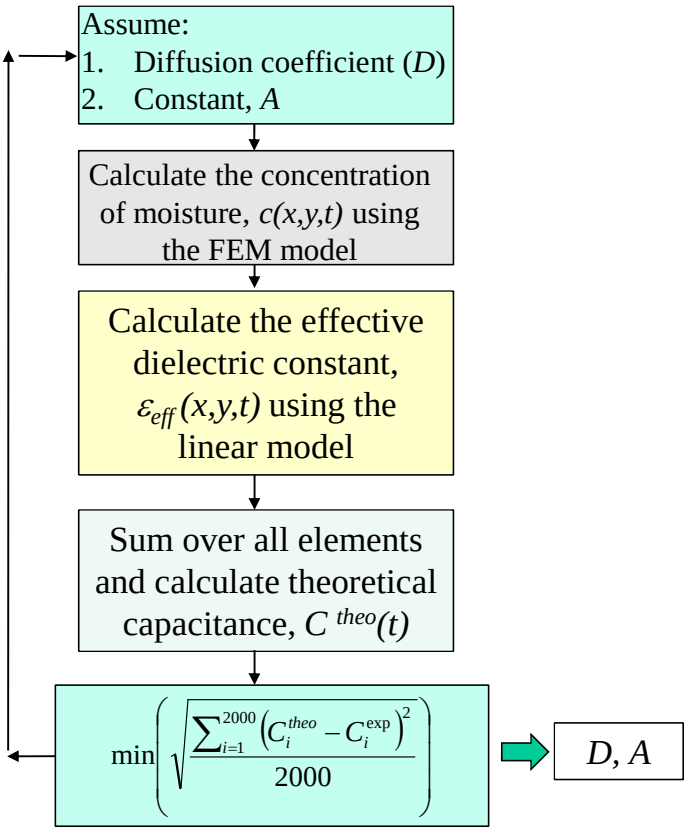


***Figure 5-20.*** *Methodology of modeling diffusion of moisture inside the embedded capacitor dielectric.*

After applying this methodology to group A capacitors (Figure 5-21), the values of $D$ and $A$ were found to be $9\times10^{-12}$ $m^2$ $s^{-1}$ and 4.2 kg $m^{-3}$. The plot of experimental versus theoretical capacitance for small capacitors is shown in Figure 5-22.

| | | D | | | | | | | | | |
|---|---|---|---|---|---|---|---|---|---|---|---|
| | | 7.00E-12 | 8.00E-12 | 9.00E-12 | 1.00E-11 | 2.00E-11 | 3.00E-11 | 4.00E-11 | 5.00E-11 | 6.00E-11 | 7.00E-11 |
| a | 3.6 | 6.90E-12 | 6.90E-12 | 9.00E-12 | 8.39E-12 | 9.11E-11 | 8.59E-11 | 5.11E-11 | 7.38E-11 | 9.23E-11 | 8.23E-11 |
| | 3.7 | 8.00E-12 | 7.81E-12 | 8.11E-12 | 9.11E-12 | 5.94E-11 | 8.11E-11 | 7.39E-11 | 9.11E-11 | 2.45E-11 | 7.29E-11 |
| | 3.8 | 9.12E-12 | 9.30E-12 | 8.19E-12 | 1.20E-11 | 9.11E-11 | 5.11E-11 | 3.73E-11 | 5.11E-11 | 5.20E-11 | 8.34E-11 |
| | 3.9 | 1.01E-11 | 6.54E-11 | 5.11E-11 | 9.11E-11 | 5.11E-11 | 7.39E-11 | 5.11E-11 | 7.39E-11 | 9.39E-11 | 3.22E-11 |
| | 4.0 | 1.29E-11 | 3.28E-11 | 7.39E-11 | 5.11E-11 | 7.39E-11 | 5.11E-11 | 7.39E-11 | 9.23E-11 | 6.28E-11 | 3.73E-11 |
| | 4.1 | 7.90E-11 | 6.54E-11 | 5.11E-11 | 9.11E-11 | 9.11E-11 | 6.54E-11 | 7.90E-11 | 9.38E-11 | 4.28E-11 | 7.32E-11 |
| | 4.2 | 9.11E-11 | 3.28E-11 | 6.12E-12 | 5.10E-11 | 7.39E-11 | 3.28E-11 | 9.11E-11 | 8.18E-11 | 6.32E-11 | 6.94E-11 |
| | 4.3 | 5.11E-11 | 9.11E-11 | 5.20E-11 | 5.11E-11 | 5.17E-11 | 5.11E-11 | 5.19E-11 | 8.11E-11 | 9.11E-11 | 9.23E-11 |
| | 4.4 | 7.39E-11 | 8.65E-12 | 9.88E-12 | 1.10E-11 | 7.39E-11 | 5.11E-11 | 5.11E-11 | 5.11E-11 | 5.11E-11 | 4.94E-11 |
| | 4.5 | 6.80E-12 | 7.10E-12 | 9.13E-12 | 8.11E-12 | 5.11E-11 | 5.11E-11 | 5.11E-11 | 5.67E-11 | 7.39E-11 | 3.28E-11 |

***Figure 5-21.*** *Optimizing the values of D and A (for small capacitors)*

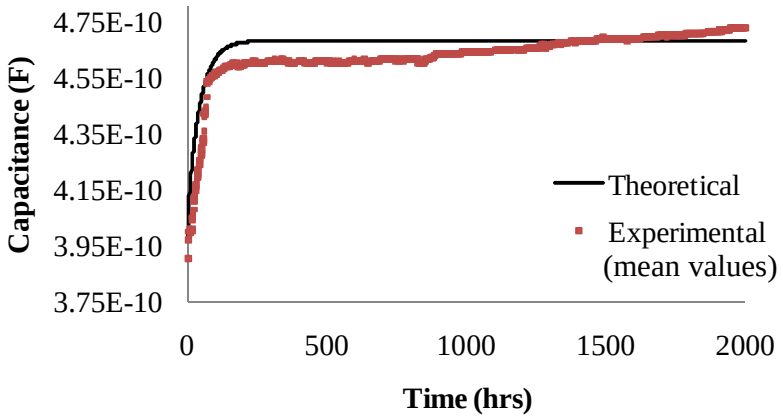


***Figure 5-22.*** *Theoretical versus experimental capacitance for small capacitors*

## *5.6 Verification of the methodology*

The accuracy of the methodology was verified by applying it to group B capacitors. The 2D FEM model of the group B capacitor had 26157 quadrilateral elements. After applying this methodology to group B capacitors (Figure 5-23), the values of $D$ and $A$ were found to be $1\times10^{-11}$ $m^2$ $s^{-1}$ and 4.0 kg $m^{-3}$. The values of the constants obtained were close to each other for both groups of capacitors, implying the validity of the methodology. The plot of experimental versus theoretical capacitance for large capacitors is shown in Figure 5-24. The capacitance did not stabilize even in 2000 hrs and this is evident from the concentration of moisture at 2000 hrs (Figure 5-25).

| | | D | | | | | | | | | |
|---|---|---|---|---|---|---|---|---|---|---|---|
| | | 7.00E-12 | 8.00E-12 | 9.00E-12 | 1.00E-11 | 2.00E-11 | 3.00E-11 | 4.00E-11 | 5.00E-11 | 6.00E-11 | 7.00E-11 |
| a | 3.6 | 7.12E-08 | 4.23E-08 | 6.98E-08 | 7.34E-08 | 8.88E-08 | 3.22E-08 | 9.11E-08 | 3.22E-08 | 4.11E-08 | 8.14E-08 |
| | 3.7 | 6.19E-08 | 6.93E-08 | 9.23E-08 | 2.33E-08 | 3.32E-08 | 8.16E-09 | 9.11E-08 | 7.13E-08 | 6.34E-08 | 7.11E-08 |
| | 3.8 | 9.74E-08 | 7.15E-08 | 6.87E-09 | 6.23E-08 | 8.44E-08 | 6.33E-08 | 8.44E-08 | 6.19E-08 | 7.77E-08 | 3.56E-08 |
| | 3.9 | 4.84E-08 | 7.29E-09 | 7.23E-09 | 7.21E-09 | 8.33E-09 | 7.88E-08 | 8.45E-08 | 9.74E-08 | 8.31E-08 | 6.11E-08 |
| | 4.0 | 6.36E-08 | 8.39E-08 | 4.53E-08 | 5.03E-09 | 5.77E-09 | 4.32E-08 | 6.34E-08 | 6.98E-08 | 8.12E-08 | 6.33E-08 |
| | 4.1 | 9.54E-08 | 2.12E-08 | 8.45E-09 | 7.34E-09 | 5.91E-09 | 9.11E-08 | 9.32E-08 | 2.11E-08 | 5.12E-08 | 7.88E-08 |
| | 4.2 | 2.12E-08 | 8.12E-09 | 9.34E-09 | 7.11E-09 | 6.33E-08 | 9.13E-09 | 8.12E-08 | 6.33E-08 | 7.15E-08 | 7.11E-08 |
| | 4.3 | 4.29E-08 | 4.23E-08 | 2.45E-08 | 4.23E-08 | 7.88E-08 | 7.66E-08 | 4.23E-08 | 7.88E-08 | 6.39E-08 | 6.14E-08 |
| | 4.4 | 7.36E-08 | 8.34E-08 | 5.87E-08 | 4.23E-08 | 9.34E-08 | 5.11E-08 | 9.34E-08 | 9.49E-08 | 7.23E-08 | 8.12E-08 |
| | 4.5 | 4.28E-08 | 4.59E-08 | 6.34E-08 | 2.66E-08 | 4.23E-08 | 7.15E-08 | 4.22E-08 | 8.34E-08 | 5.45E-08 | 5.33E-08 |

***Figure 5-23.*** *Optimizing the values of D and A (for large capacitors)*

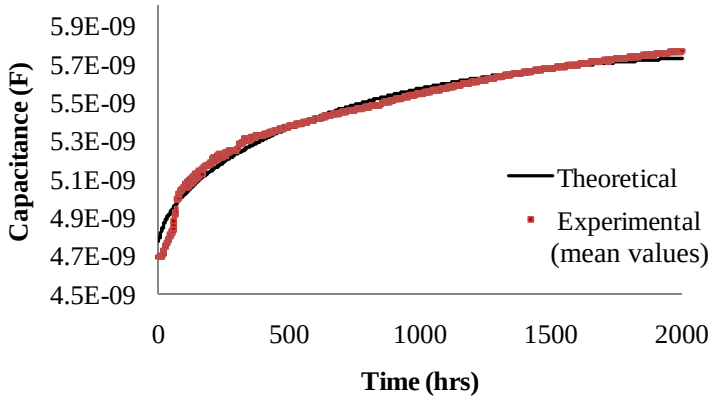


***Figure 5-24.*** *Theoretical versus experimental capacitance for large capacitors.*

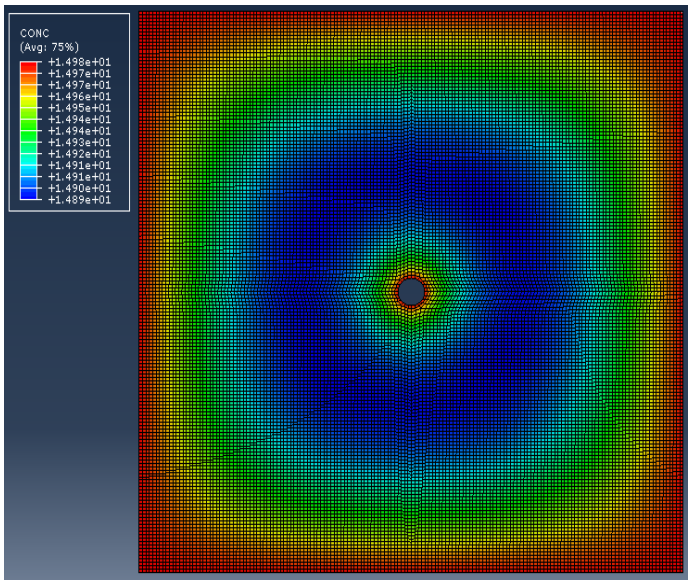


***Figure 5-25.*** *Concentration of moisture in large capacitors at 2000 hrs.*

# 6. Lifetime modeling

## 6.1 Experimental setup

For highly accelerated life tests, the same monitoring setup and failure criterion was used that was used in the THB test. Measurements were performed on about 35 out of 80 small capacitors (group A) and 4 out of 6 large capacitors (group B) of TV-1 (8 μm dielectric thickness).

## 6.2 Stress levels

The temperature at any stress condition was less than 125$^{o}$C since the maximum operating temperature of the test board was 130$^{o}$C. The applied voltage was selected such that the voltage was well below the breakdown voltage ($V_{BD}$) of the capacitor dielectric at that temperature. The breakdown voltage of 10 embedded capacitors (of group A) was measured at 85$^{o}$C and 125$^{o}$C [68]. The results of the breakdown voltage are shown in Figure 6-1. It was observed that the value of $V_{BD}$ decreased with an increase in temperature. A reduction in breakdown voltage with an increase in temperature can be explained by the free volume theory of the polymer matrix [70]. With an increase in temperature, free volume or open air spaces in the polymer increases. Charged particles now get accelerated for a longer distance and have higher energy and hence the breakdown voltage decreases. From the observed trend and this theory it implies that breakdown was taking place in the polymer matrix as expected.

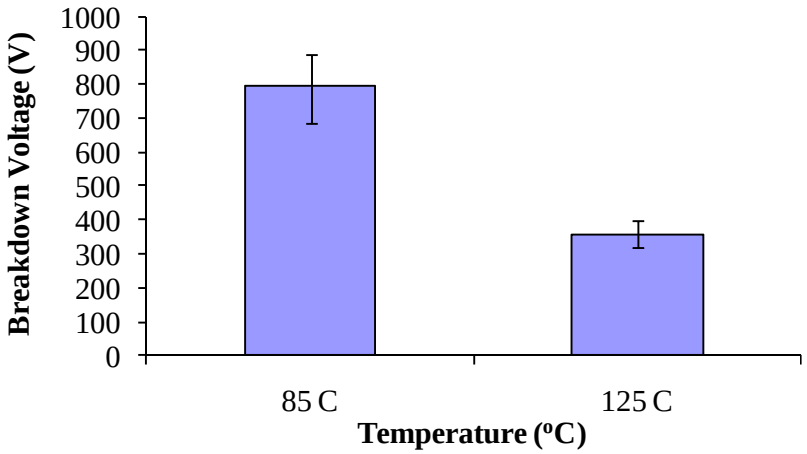


***Figure 6-1.*** *Effect of temperature on the breakdown voltage ($V_{BD}$) of small (group A) capacitors.*

Failure-terminated tests were conducted at 5 different stress levels, as shown in Table 6-1. Before the start of these tests the test vehicle was preconditioned at 105°C for 48 hrs to remove any moisture. The value of the time-to-failure of each capacitor was recorded at all five stress levels.

***Table 6-1.*** *Stress levels for highly accelerated life testing.*

| Stress level | Temperature (T) | Voltage (V) |
|---|---|---|
| 1 | 105°C | 285 |
| 2 | 115°C | 285 |
| 3 | 125°C | 285 |
| 4 | 125°C | 250 |
| 5 | 125°C | 225 |

## 6.3 Observations

At all stress levels the failure modes observed were a sudden decrease in insulation resistance, sudden increase in dissipation factor, and a gradual decrease in capacitance. The sudden decrease in insulation resistance and sudden increase in dissipation factor were the result of the same physical phenomenon, i.e. avalanche breakdown (ABD) of the dielectric [71]. A typical plot of insulation resistance and dissipation factor is shown in Figure 6-2 and Figure 6-3 respectively. This failure mode is not expected during the normal operating condition due to highly accelerated conditions; however the results can be used for qualification tests, development of new composite materials, and development of new manufacturing processes.

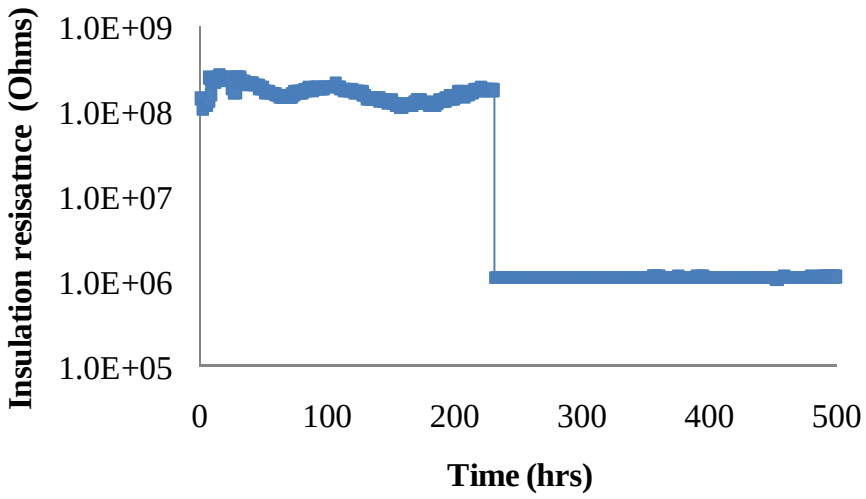


***Figure 6-2.*** *Insulation resistance of one small (group A) capacitor at 125 $^{o}$C and 285 V.*

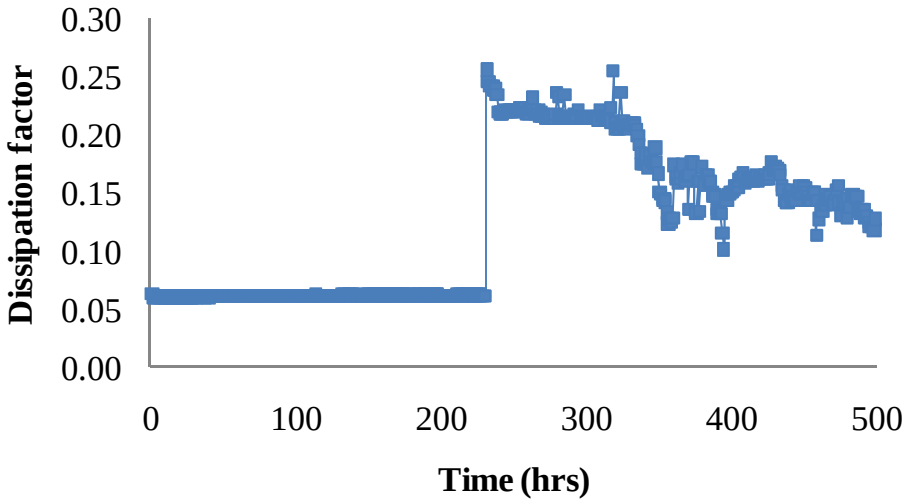


***Figure 6-3.*** *Dissipation factor of one small (group A) capacitor at 125 °C and 285 V.*

It was observed that the capacitance degraded logarithmically according to well known aging equation (equation 2). A typical plot of capacitance during aging is shown in Figure 6-4.

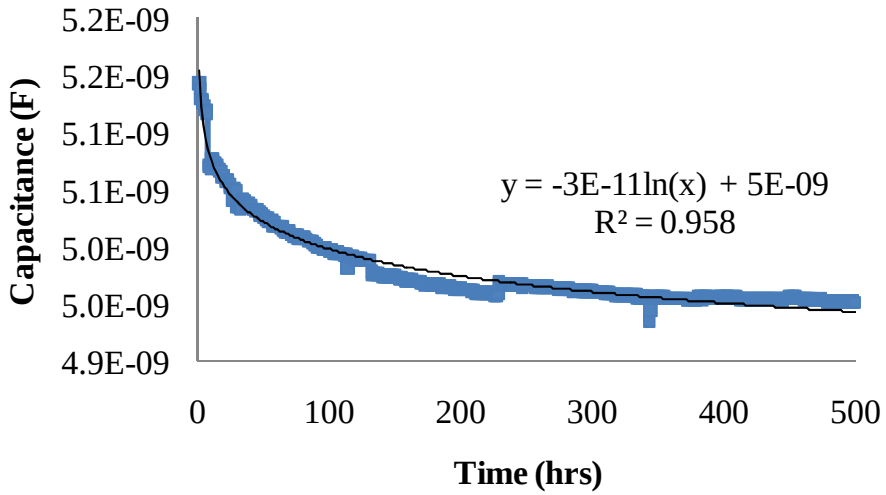


***Figure 6-4.*** *Capacitance of one large (group B) capacitor at 125 °C and 285 V.*

### 6.3.1 Rapid monitoring of insulation resistance

In these experiments, data were monitored after every 1 h and it is possible that the degradation in IR or DF could have taken place over a period of a few minutes. In order to find a trend in the values of IR before failure (if any), another experiment was conducted with rapid monitoring of IR. Since rapid monitoring was to be performed, the experimental setup was modified and the voltage bias was not turned off while performing measurements [72]. A voltage bias of 285V was applied across one capacitor dielectric (maintained at 125$^{o}$C) and the resulting current was monitored in the circuit after every 1 s. The value of the IR was then calculated using Ohm's law. It was observed that the drop in IR took place within 1 seconds implying ABD as shown in Figure 6-5. This experiment was repeated for three large (group B) capacitors.

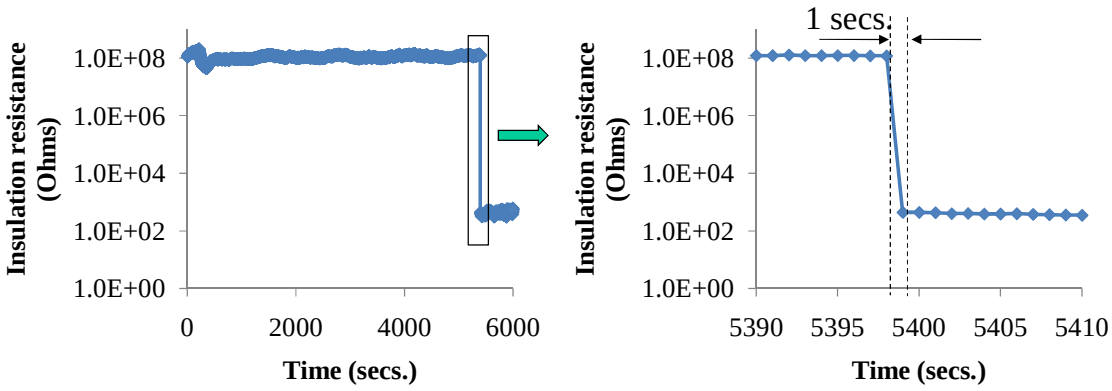


***Figure 6-5.*** *Rapid monitoring of insulation resistance at 125 $^{o}$C and 285 V for one large (group B) capacitor.*

## *6.4 Modeling the avalanche breakdown failures*

A summary of the test results at all five stress levels is shown in Table 6-2, where F represents failed and S represents survived.

***Table 6-2.*** *Summary of highly accelerated life testing.*

| Stress level | Duration of test (hrs) | Number of failed (F) and survived (S) capacitors at the end of test | |
|---|---|---|---|
| | | Group A | Group B |
| 105°C, 285V | 2400 | 15(F) + 18 (S) | 4(F) + 0(S) |
| 115°C, 285V | 2000 | 36(F) + 0(S) | 4(F) + 0(S) |
| 125°C, 285V | 500 | 32(F) + 1(S) | 4(F) + 0(S) |
| 125°C, 250V | 875 | 31(F) + 2(S) | 4(F) + 0(S) |
| 125°C, 225V | 2300 | 35(F) + 1(S) | 4(F) + 0(S) |

Statistical analysis of the time-to-failure was performed using the Weibull software. At all stress levels the time-to-failure followed a bimodal distribution, so a mixed Weibull distribution with 2 subpopulations was used for further analysis. The probability density function (pdf) plot of time-to-failure at various stress levels is shown in Figure 6-6, Figure 6-7, Figure 6-8, Figure 6-9, and Figure 6-10 The two lobes of the pdf plot are referred to as Type I and Type II here after as shown in Figure 6-6. No statistical analysis was performed on the time-to-failure of large capacitors (group B) due to the small sample size.

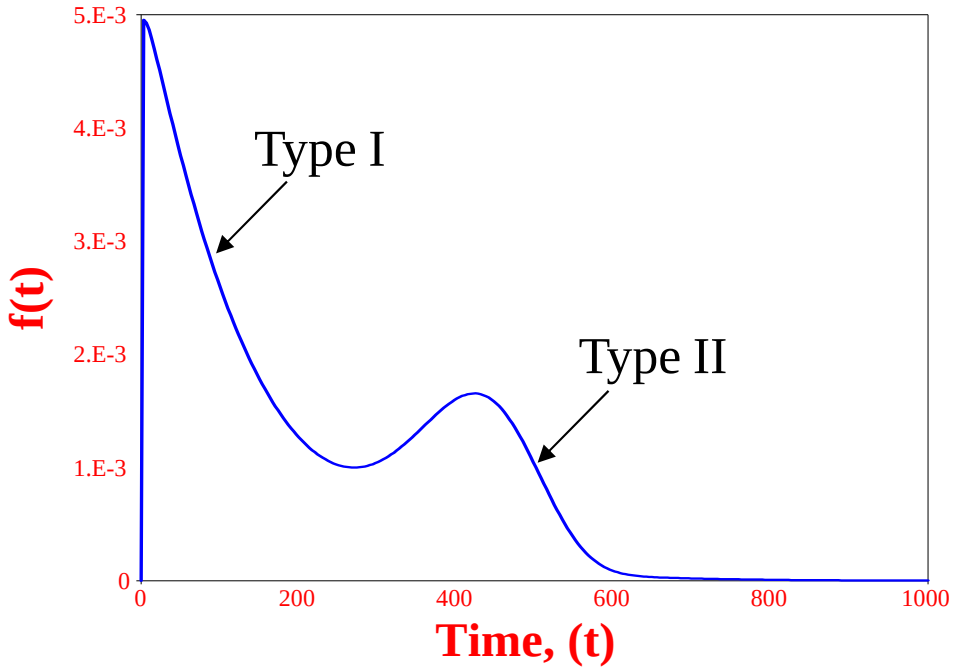


***Figure 6-6.*** *Probability density function of the time-to-failure at 125 $^{o}$C and 285 V for small (group A) capacitors.*

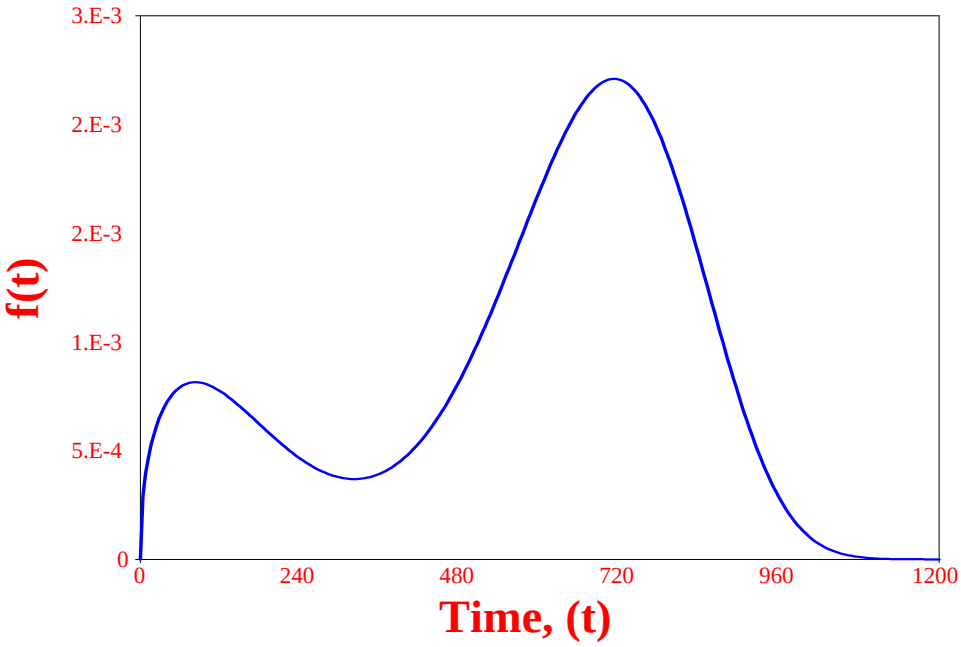


***Figure 6-7.*** *Probability density function of the time-to-failure at 125 $^{o}$C and 250 V for small (group A) capacitors.*

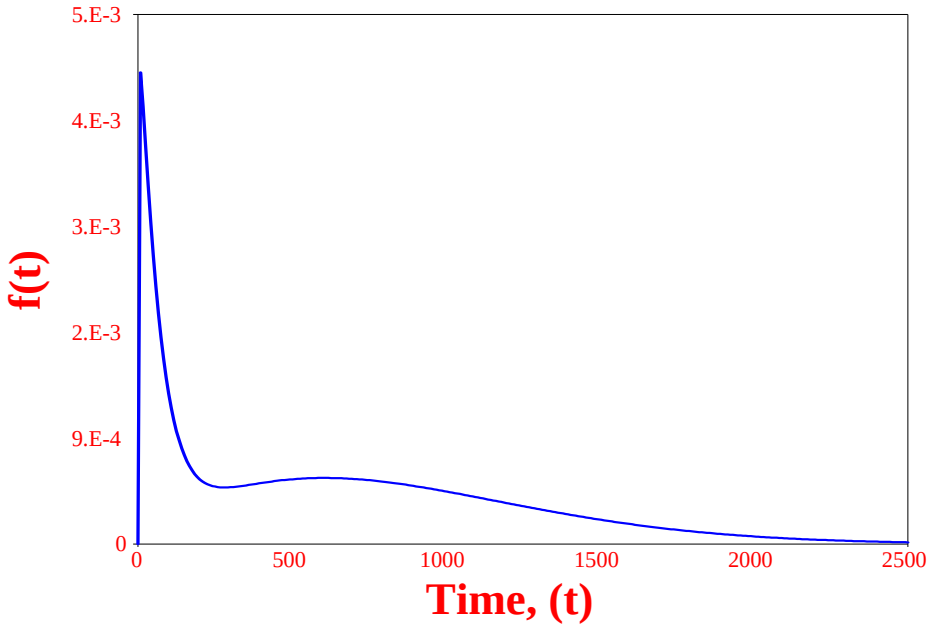


***Figure 6-8.*** *Probability density function of the time-to-failure at 115 $^{o}$C and 285 V for small (group A) capacitors.*

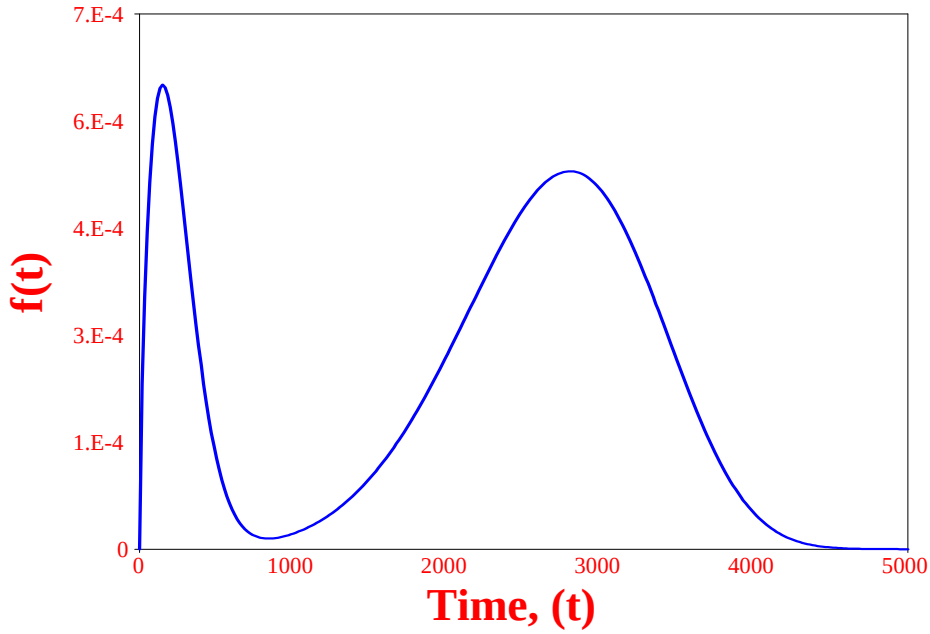


***Figure 6-9.*** *Probability density function of the time-to-failure at 105 $^{o}$C and 285 V for small (group A) capacitors.*

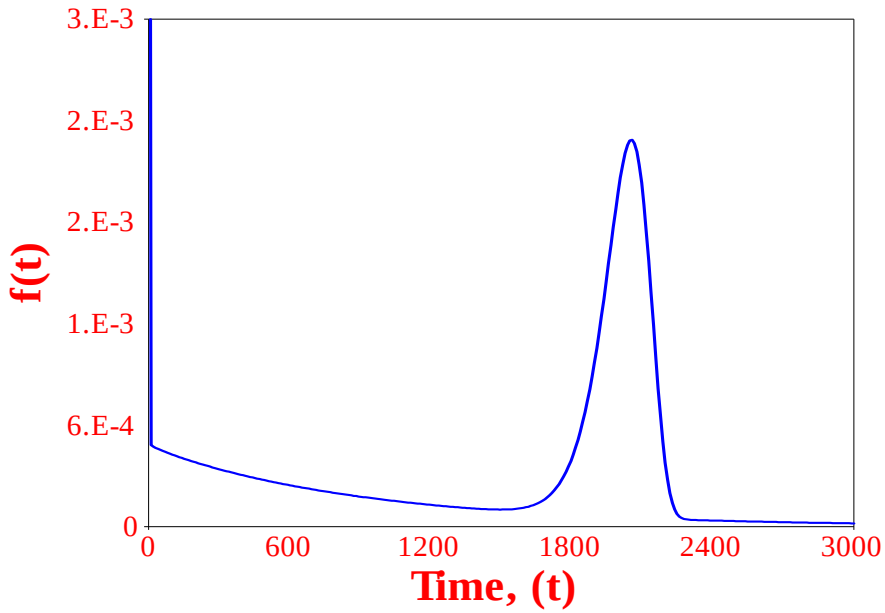


***Figure 6-10.*** *Probability density function of the time-to-failure at 125$^{o}$C and 225 V for small (group A) capacitors.*

### 6.4.1 Activation energy of the Prokopowicz model

For computing the activation energy ($E_a$) of the Prokopowicz model, the results of highly accelerated life tests conducted at stress levels 1, 2 and 3 (Table 6-1) are used. The unreliability versus time plot for small capacitors (group A) at these three stress conditions is shown in Figure 6-11.

Statistical analysis of the time-to-failure at these stress levels using mixed Weibull distribution (2 sub-population) is shown in Table 6-3. In Table 3, $\beta$ is the shape parameter, $\eta$ is the scale parameter, and MTTF is the mean-time-to-failure of a Weibull distribution. It is observed that the value of $\beta$ for Type I failure is close to 1, implying random failures. These failures were expected to be due to defects in the dielectric such as porosity, voids, and agglomeration of the ceramic particles. The value of $\beta$ for Type II

failure is greater than 1, implying that these failures were the result of a wear-out process. Since Type I failures are random in nature, it is difficult to model using the Prokopowicz model. This is also clear from the MTTF data of Type I failures that do not show a consistent trend.

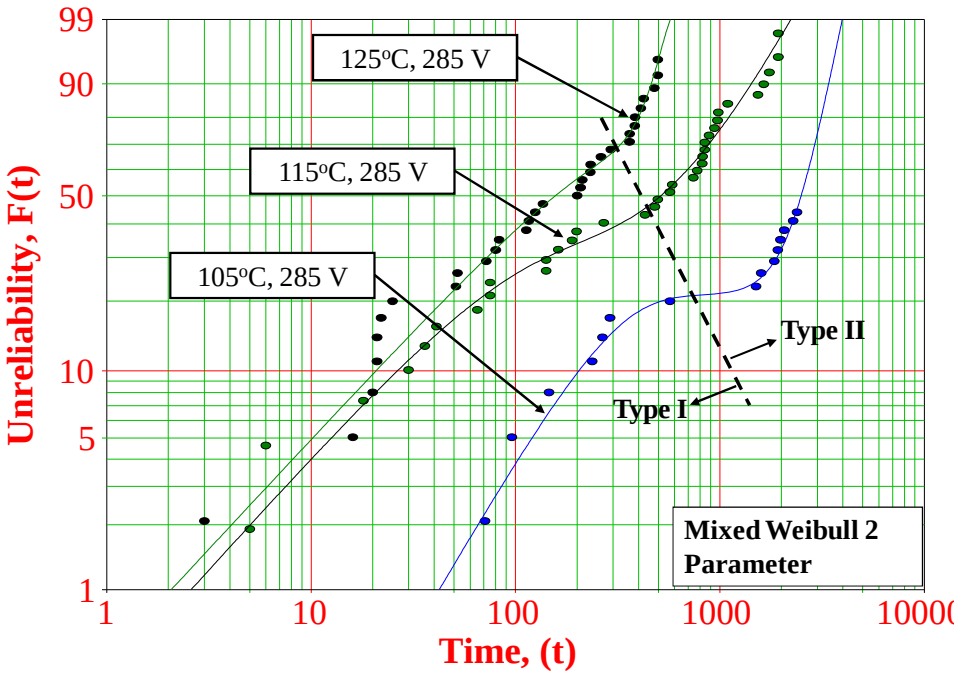


***Figure 6-11.*** *Unreliability versus time plot at different temperatures (at a constant voltage of 285 V) for small (group A) capacitors.*

***Table 6-3.*** *Statistical analysis of time-to-failure to calculate the activation energy of the Prokopowicz model.*

| Stress levels | Type I | | | Type II | | |
|---|---|---|---|---|---|---|
| | $\beta$ | $\eta$ | MTTF (hrs) | $\beta$ | $\eta$ | MTTF (hrs) |
| 105°C, 285V | 1.6 | 267 | 238 | 4.9 | 2937 | 2702 |
| 115°C, 285V | 1.1 | 65 | 63 | 1.8 | 979 | 871 |
| 125°C, 285V | 1.0 | 130 | 130 | 6.0 | 444 | 413 |

The value of $\beta$ for Type II failures at 115$^{o}$C and 285V was found to 1.8 which is closer to 1. This is not expected and it contradicts the defect/wear-out driven failure theory proposed earlier. If we take a closer look at the unreliability versus time plot at this stress level (Figure 6-11), we can see that the last 5 failure points do not follow the trend of other Type II failures. There might be various possible reasons for this behavior. These 5 failures may be due to a new failure mechanism (i.e. Type III) and have a separate distribution. But this is not very likely since this behavior was not observed at other stress levels. Another possible explanation is that these 5 failures belong to Type I. This is possible since the slope of Type I failures and these 5 failures seem to be close to each other.

At constant voltage, the Prokopowicz model reduces to an Arrhenius equation, which is given by:

$$MTTF = A\exp\left(\frac{E_a}{kT}\right) \tag{13}$$

where A is a constant. A plot of *MTTF* versus *T* is shown in Figure 6-12. Regression was performed to fit the Arrhenius equation to the experimentally obtained data points. The goodness of fit ($R^2$) was found to be 0.98, implying that the Arrhenius equation can be used to model the temperature-dependent mean-time-to-failure in these nanocomposites. The value of the activation energy was found to be 1.11 eV.

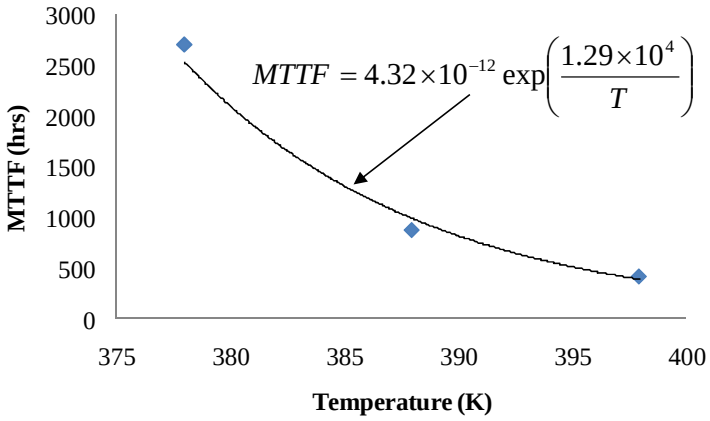


***Figure 6-12.*** *The effect of temperature on the mean time to failure (MTTF) of small (group A) capacitors at 285 V.*

## 6.4.2 Voltage exponent of the Prokopowicz model

For computing the voltage exponent ($n$) of the Prokopowicz model, the results of highly accelerated life tests conducted at stress levels 3, 4 and 5 (Table 6-1) are used. The unreliability versus time plot for small capacitors (group A) is shown in Figure 6-13.

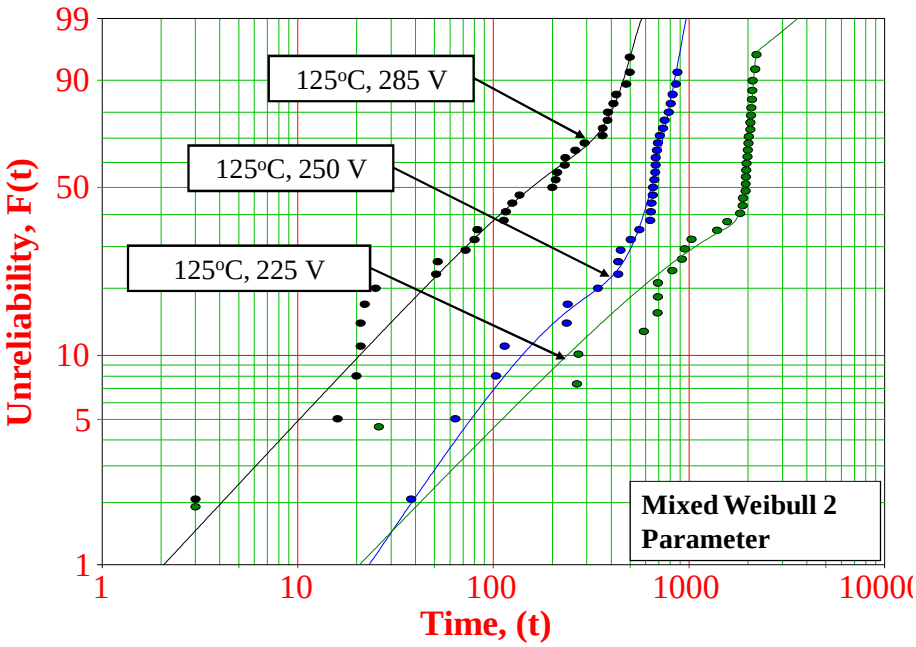


***Figure 6-13.*** *Unreliability versus time plot at different voltages (at a constant temperature of 125 $^{o}$C) for small (group A) capacitors.*

Statistical analysis of the time-to-failure at these stress levels using a mixed Weibull distribution (2 sub-population) is shown in Table 6-4. At these stress levels also, the value of $\beta$ for Type I failures was found to be close to 1, implying random failures.

***Table 6-4.*** *Statistical analysis of time-to-failure to calculate the voltage exponent of the Prokopowicz model.*

| Stress levels | Type I | | | Type II | | |
|---|---|---|---|---|---|---|
| | β | η | MTTF (hrs) | β | η | MTTF (hrs) |
| 125$^{o}$C, 285V | 1.0 | 130 | 130 | 6.0 | 444 | 413 |
| 125$^{o}$C, 250V | 1.4 | 188 | 171 | 5.5 | 739 | 680 |
| 125$^{o}$C, 225V | 1.0 | 935 | 935 | 22.3 | 2058 | 1996 |

The value of $\beta$ for Type II failures at 125$^{o}$C and 225V was found to 22.3 which is very high as compared to the value of $\beta$ at other stress levels. This might be due to a shift in the mechanism of failure. Although, the failure mode was avalanche breakdown at all the stress levels, there can be various mechanisms leading to this failure mode. This breakdown can take place due to higher electric field in the epoxy matrix due to a difference in the dielectric constant of epoxy and Barium titanate. A higher electric field in the epoxy matrix (leading to breakdown) can also be due to agglomeration of Barium titanate particles. Presence of a void (where the electric field is maximum) can also trigger avalanche breakdown. The root cause of avalanche breakdown was difficult to identify since after breakdown the failure site was charred (which was confirmed by performing failure analysis) and all the information about that site was lost.

At constant temperature, the Prokopowicz model reduces to a power law equation:

$$MTTF = \frac{B}{V^n} \tag{14}$$

where $B$ is a constant. A plot of $MTTF$ versus $V$ is shown in Figure 6-14. Regression was performed to fit the power law equation to the experimentally obtained data points. The goodness of fit ($R^2$) was found to be 0.93, implying that the power law equation can be used to model the voltage-dependent time-to-failure in these nanocomposites. The value of the voltage exponent was found to be 6.55.

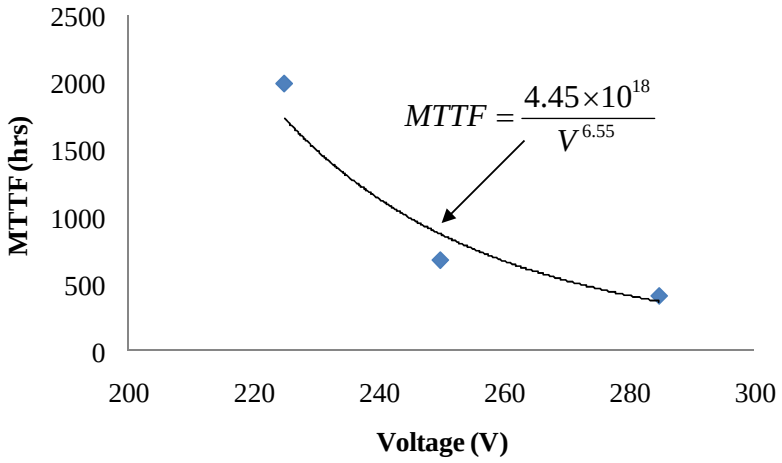


***Figure 6-14.*** *The effect of voltage on the mean time to failure (MTTF) of small (group A) capacitors at 125 $^oC$.*

## 6.4.3 Effect of area on avalanche breakdown failures

All four large capacitors (group B) were observed to fail within 10 hrs at all stress levels, i.e., long before the time-to-failure of small capacitors (group A). This can be explained by the defect-driven failure theory proposed earlier in this paper. Failures in large capacitors were expected to belong to Type I, since they occurred early in the

lifetime. As we increase the area of the capacitor, the number of defects in the dielectric increases, which leads to a reduction in the time-to-failure.

### 6.4.4 Applicability of the Prokopowicz model

Although the lifetime was modeled using the data of Group A capacitors from TV-1 (with 8 μm dielectric thickness), this model is applicable to capacitor of any configuration (area and dielectric thickness) as long as the dielectric material is same. This is because Prokopowicz model relates the ratio of time-to-failure at two different stress levels for a capacitor of given dimensions. This model is expected to work in general for an epoxy-$BaTiO_3$ composite with loading of $BaTiO_3$ close to 45%.

$$\left(\frac{t_1}{t_2}\right)_{Configuration\,1} = \left(\frac{t_1}{t_2}\right)_{Configuration\,2} = \text{.....} = \left(\frac{V_2}{V_1}\right)^{6.55} \exp\left(\frac{1.11\,eV}{k}\left(\frac{1}{T_1}-\frac{1}{T_2}\right)\right) \qquad (15)$$

## *6.5 Modeling the capacitance failures*

Regression was performed to compute the values of the dielectric aging rate ($k$) at all stress levels. The results of the regression analysis are shown in Table 6-5. In some capacitors, the value of capacitance started to fluctuate after avalanche breakdown failures. Data of such capacitors were eliminated since the objective here was to model the decrease in capacitance independently of the decrease in insulation resistance.

Failures as a result of a decrease in capacitance (>20%) were observed in small capacitors (group A) at all stress levels. Histograms of decrease in capacitance for small capacitors (group A) for the three test conditions are shown in Figure 6-15.

***Table 6-5.*** *Dielectric aging rate of small (group A) and large (group B) capacitors.*

| Stress levels | Small (group A) | Large (group B) |
|---|---|---|
| 105°C, 285V | $12.64\times10^{-11}$ | $3.35\times10^{-11}$ |
| 115°C, 285V | $7.94\times10^{-11}$ | $3.43\times10^{-11}$ |
| 125°C, 285V | $6.89\times10^{-11}$ | $3.98\times10^{-11}$ |
| 125°C, 250V | $4.43\times10^{-11}$ | $7.21\times10^{-11}$ |
| 125°C, 225V | $4.13\times10^{-11}$ | $4.97\times10^{-11}$ |

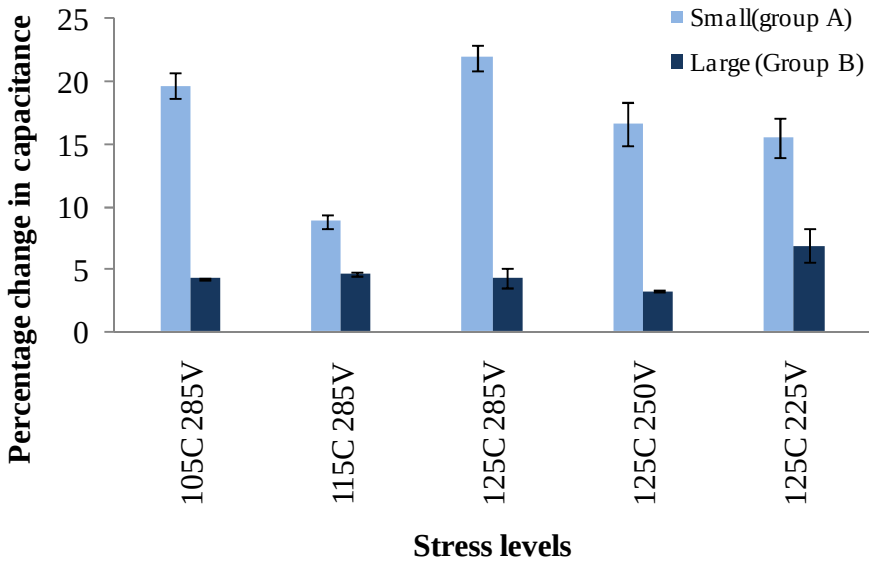


***Figure 6-15.*** *Percentage change in capacitance at different stress levels for small (group A) and large (group B) capacitors.*

## 6.5.1 Effect of area on capacitance failures

No failures as a result of a gradual decrease in capacitance were observed in large capacitors (group B). The maximum decrease in capacitance of large capacitors was only

about 5%. This can be explained as follows: the TTF as a result of a 20% decrease in capacitance can be expressed as [73]:

$$TTF = \ln^{-1}\left(\frac{0.2C_o}{k_o}\right) \tag{16}$$

The value of dielectric aging rate ($k$) was found to be comparable for small and large capacitors (which are shown in Table 6-5). But the initial value of capacitance ($C_o$) of large capacitors (~5nF) was around one order of magnitude higher than the initial value of capacitance of small capacitors (~400pF) and hence no failures were observed in large capacitors during the duration of the test.

## *6.6 Investigation of the failure/degradation mechanisms*

### 6.6.1 Avalanche breakdown

Avalanche breakdown (ABD) leads to the formation of a conduction path through the dielectric material. But even after ABD, the final insulation resistance of the dielectric was quite high (of the order of $10^4$-$10^5\,\Omega$), implying that the dimensions of the failure site were microscopic. The challenge in performing failure analysis was to locate the failure site, which was at an unknown location in the capacitor dielectric. Use of non-destructive techniques such as thermal imaging and SQUID (Superconducting Quantum Interference Device) microscopy can possibly locate the failure site which can be analyzed later after cross sectioning. But thermal imaging was not expected to work due to a high insulation resistance even after failure. Further there were some probing issues for the use of SQUID.

In this work a novel technique was used to understand the mechanism of these failures [74]. In this technique similar failures were induced in a healthy capacitor at a predetermined site. Since the failure site was already known, use of other non-destructive techniques was not required. The temperature dependant breakdown voltage of the dielectric material was utilized in this technique. The procedure involved removing a healthy capacitor from the PWB. Electrical wires were connected to both planes of the capacitor and the capacitor was potted in epoxy. The potted sample was grinded from one direction to expose both planes of the capacitor. The sample was then fine polished and etched in $FeCl_3$ solution to make sure that the spacing between the Cu planes was uniform and also to remove any Cu debris from the dielectric. Finally the polished surface was coated with a thin layer of epoxy to prevent any corona discharge. The process steps of sample preparation are shown in Figure 6-16.

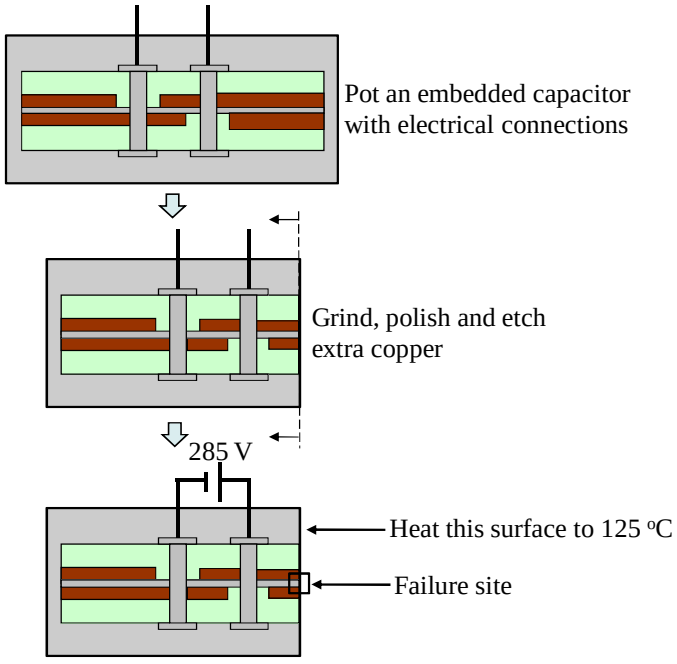


***Figure 6-16.*** *Sample preparation steps to investigate the site of avalanche breakdown.*

Once the sample was made, this technique was demonstrated to analyze the failure site during stress test at 125$^{o}$C and 285 V. The polished surface of the sample was heated to 125$^{o}$C a voltage of 285 V was applied across the capacitor. Since the maximum temperature was at the polished surface, the probability of ABD in the dielectric close to the polished surface was high. Figure 6-17 shows the site of avalanche breakdown that was achieved using the technique described above.

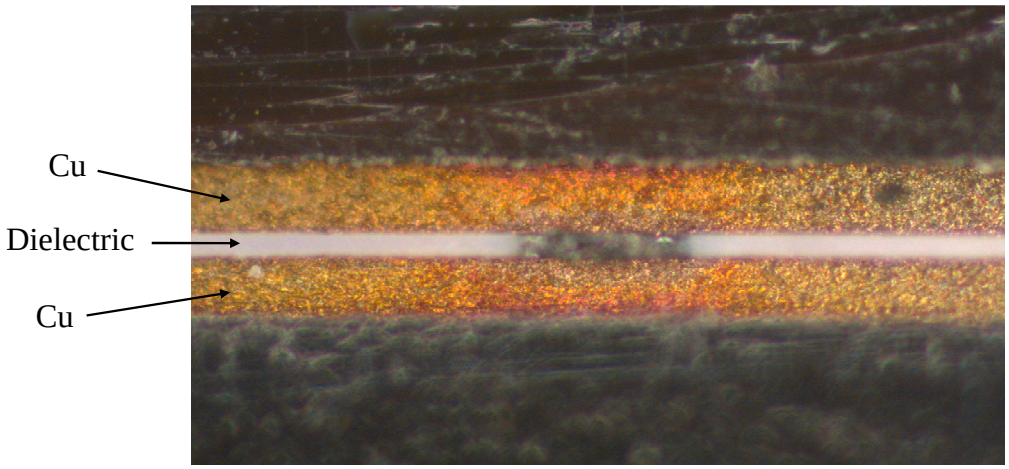


***Figure 6-17.*** *The site of avalanche breakdown, seen as the dark region in the dielectric.*

## 6.6.2 Decrease in capacitance

The mechanism of decrease in capacitance can be either an increase in the plate spacing due to thermal stresses or a decrease in the dielectric constant due to aging in $BaTiO_3$. An increase in plate spacing due to thermal deformations is not dominant in this case since the percentage decrease in capacitance of small and large capacitors was quite different. Further, the degradation in capacitance followed the aging equation so aging in $BaTiO_3$ is expected to be the degradation mechanism.

The degradation in capacitance was investigated for de-aging (by heating the test vehicle at a temperature close to the Curie temperature of $BaTiO_3$). To investigate this,

the test vehicle that was aged at 105$^{o}$C and 285 V for 2400 hrs was selected. The aged test board was heated for 20 hrs at a temperature of 130$^{o}$C (which is close to the Curie temperature of $BaTiO_3$) and in-situ measurements of capacitance were performed. It was observed that the capacitance continued to decrease as shown in Figure 6-18. It implies that were no de-aging effects in this composite material as are found in pure $BaTiO_3$ dielectric. It might also be possible that the Curie temperature of $BaTiO_3$ in this composite material was higher than 130$^{o}$C. But the temperature was not increased beyond 130$^{o}$C since this was the maximum operating temperature of the PWB.

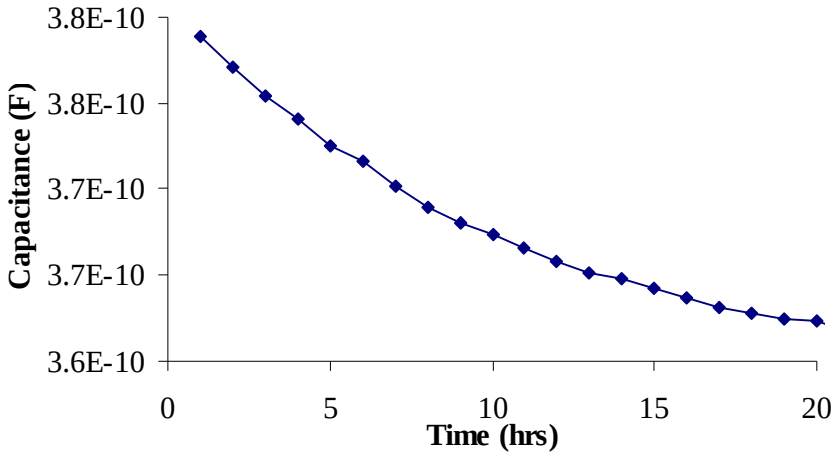


***Figure 6-18.*** *Capacitance of one small (group A) capacitor during heating at 130 $^{o}$C.*

## 6.7 Comparison with other commercially available embedded capacitor

Highly accelerated life test at 125$^{o}$C and 285V was also performed on TV-2 (test vehicle with a dielectric thickness of 14 μm). Capacitors of TV-1 and TV-2 had the same dielectric material but had a different dielectric thickness. The objective of this test was to compare two different embedded capacitors at a constant stress level.

The testing at 125°C and 285V lasted for 525 hours. The failure modes were the same that were observed during highly accelerated life tests of TV-1. Typical plots of insulation resistance, dissipation factor, and capacitance are shown in Figure 6-19, Figure 6-20, and Figure 6-21 respectively.

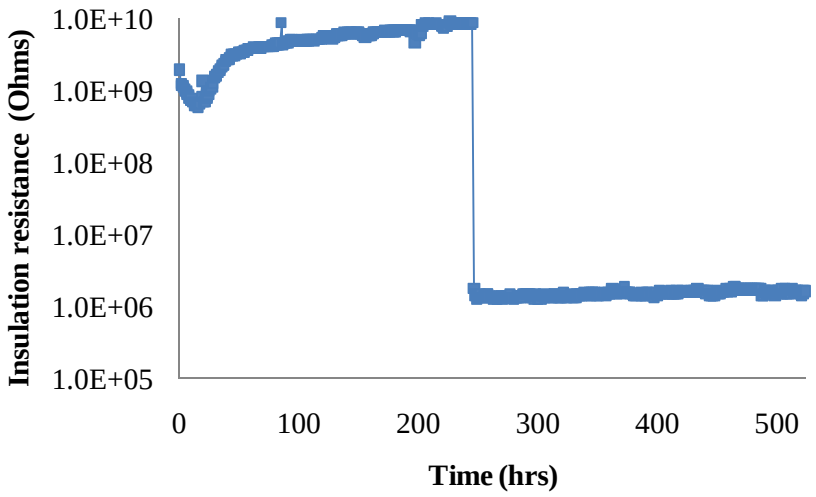


***Figure 6-19.*** *Insulation resistance of one small (group A) capacitor from TV-2 (14 μm dielectric thickness) at 125 °C and 285 V.*

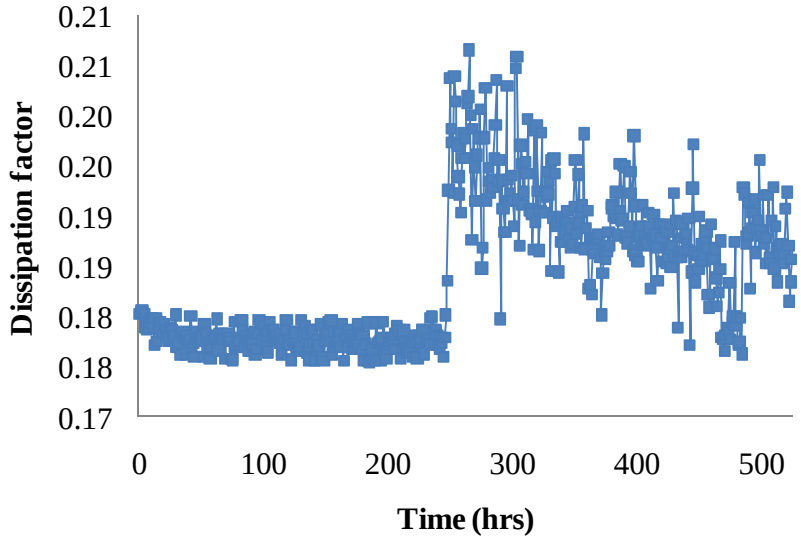


***Figure 6-20.*** *Dissipation factor of one small (group A) capacitor from TV-2 (14 μm dielectric thickness) at 125 °C and 285 V.*

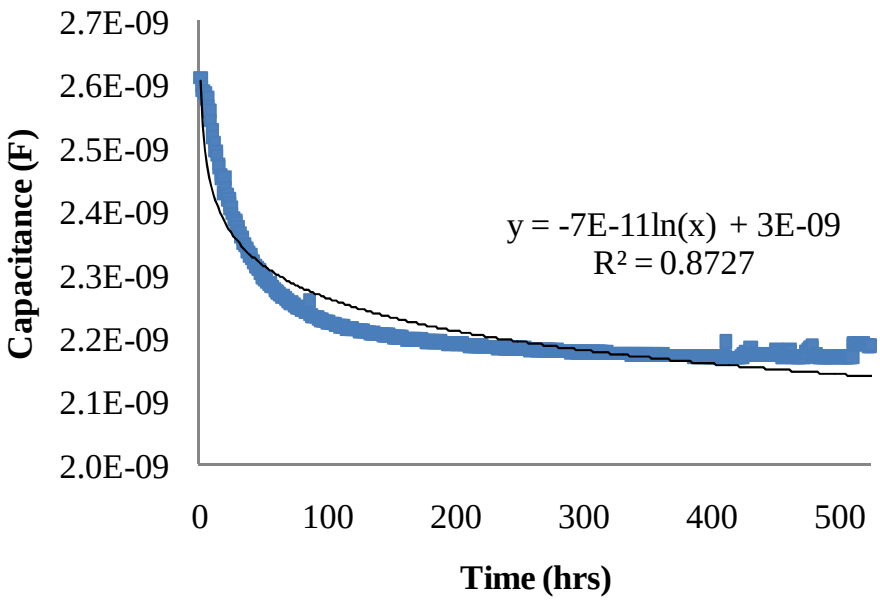


***Figure 6-21.*** *Capacitance of one large (group B) capacitor from TV-2 (14 μm dielectric thickness) at 125 °C and 285 V.*

Statistical analysis was performed on the time-to-failure data (as a result of a decrease in the insulation resistance at 125°C and 285V) of small capacitors using the Weibull software. The time-to-failure was observed to follow a Weibull 2 parameter distribution. The parameters of the distribution, $\beta$ and $\eta$ were found to be 2.0 and 383 respectively. The unreliability versus time-to-failure plots of capacitors from TV-1 (8 μm dielectric thickness) and TV-2 (14 μm dielectric thickness) are shown in Figure 6-22. It was observed that with an increase in the dielectric thickness, type I (random) failures disappeared. A possible hypothesis for this can be an improvement in the manufacturing processes of these capacitors since the capacitor laminate of TV-2 was newer than the capacitor laminate of TV-1.

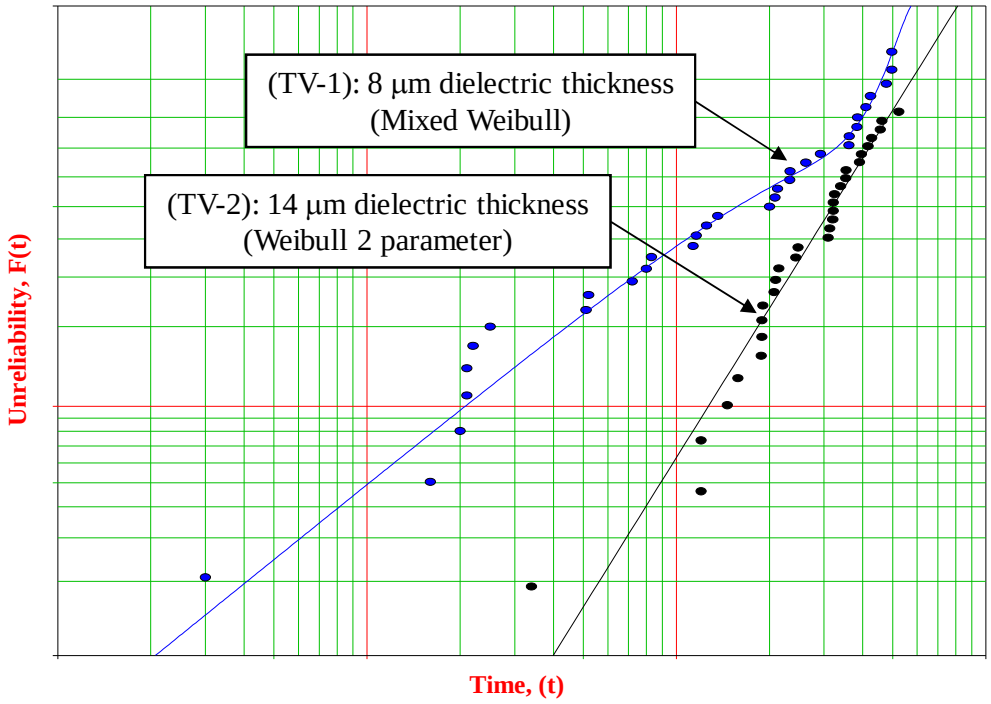


***Figure 6-22.*** *Unreliability versus time plot for small (group A) capacitors at 125 $^{o}$C and 285 V.*

Regression was performed to calculate the value of the dielectric aging rate ($k$). The value of the dielectric aging rate for small (group A) and large (group B) capacitors were found to be $4.52\times10^{-11}$ and $7.75\times10^{-11}$ respectively and is shown in Table 6-6. These values are close to the dielectric aging rate of capacitors from TV-1 since the dielectric material was the same.

***Table 6-6.*** *Dielectric aging rate of capacitors from TV-1 and TV-2.*

| Stress level | TV-1 | | TV-2 | |
|---|---|---|---|---|
| | Small | Large | Small | Large |
| 125$^{o}$C and 285V | $6.89\times10^{-11}$ | $3.98\times10^{-11}$ | $4.52\times10^{-11}$ | $7.75\times10^{-11}$ |

# 7. Conduction mechanisms in a commercially available capacitor

The mechanism of current conduction was investigated in the test vehicle that was used for THB test and for life time modeling during highly accelerated life tests (TV-1) [75]. Three small (group A) capacitors from TV-1 were selected for this analysis.

## *7.1 Measurement of leakage current*

The leakage current across the capacitor dielectric was measured using an Agilent 4155C Semiconductor parameter analyzer (Figure 7-1) as a function of voltage. The voltage was varied from 0 to 100 V in steps of 10 volts. Leakage current was measured 10 seconds after each step change of voltage, allowing ample time for the current to stabilize. This voltage sweep was repeated over the temperature range of 25$^{o}$C to 125$^{o}$C in increments of 10$^{o}$C. Once the voltage sweep at a given temperature was performed, the temperature was raised by 10$^{o}$C and voltage sweep at the next temperature was performed after 5 minutes, allowing sufficient time for the temperature to stabilize. The temperature of the test board was controlled using a Thermostream (Figure 7-2). In addition to the temperature readings from the Thermostream; a thermocouple was also attached on the surface of the test board. These measurements were performed on three small (group A) capacitors. The results of the experiment are shown in Figure 7-3 for one capacitor.

***Figure 7-1.*** *Agilent 4155C semiconductor parameter analyzer.*

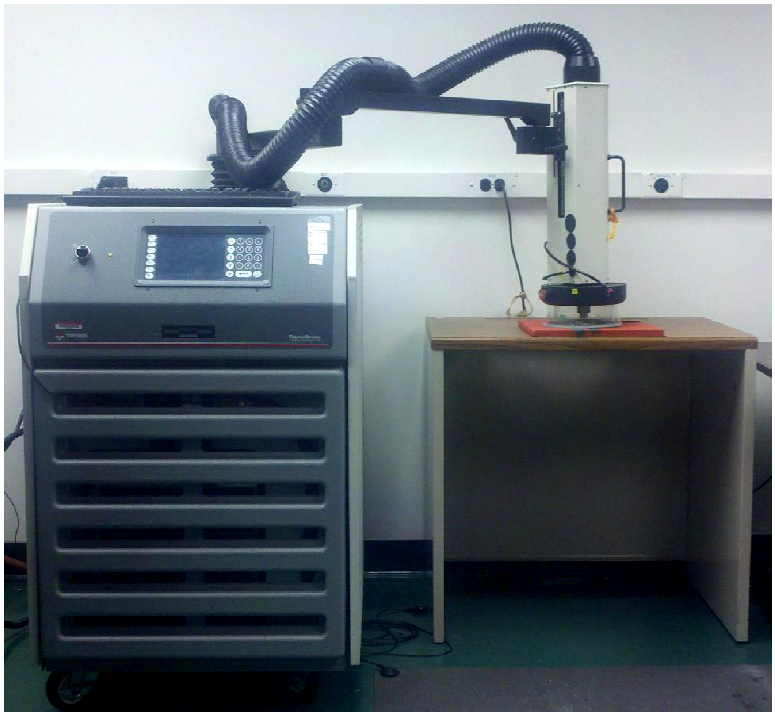

***Figure 7-2.*** *Thermostream (air stream temperature forcing system from Temptronic Corporation).*

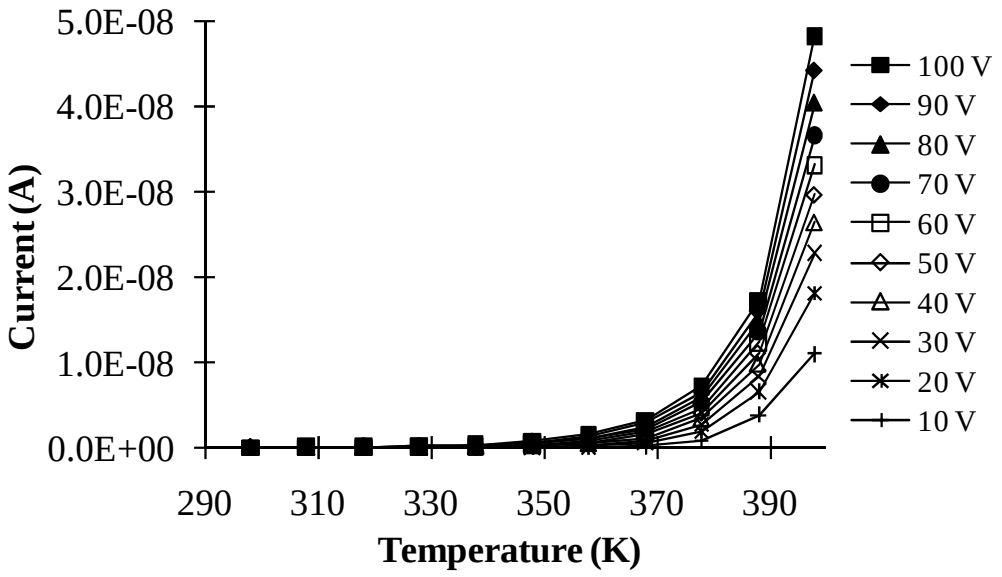


***Figure 7-3.*** *Leakage current versus temperature at various voltages in one capacitor.*

## *7.2 Evaluation of Ohmic conduction*

The conduction of current at a constant temperature is checked for Ohmic behavior. In general the current density ($J$) and electric field ($E$) is related by:

$$J = \sigma E^{p} \tag{17}$$

where $\sigma$ is the conductivity and $p$ is the electric field exponent. For a current to follow the Ohm's law, the mobility of charged carriers has to be independent of the applied electric field. The value of $p$ for Ohmic conduction is equal to 1. A plot of logarithm of current density versus logarithm of electric field should produce straight lines (at constant temperature) with a slope of 1 if the current follows Ohm's law.

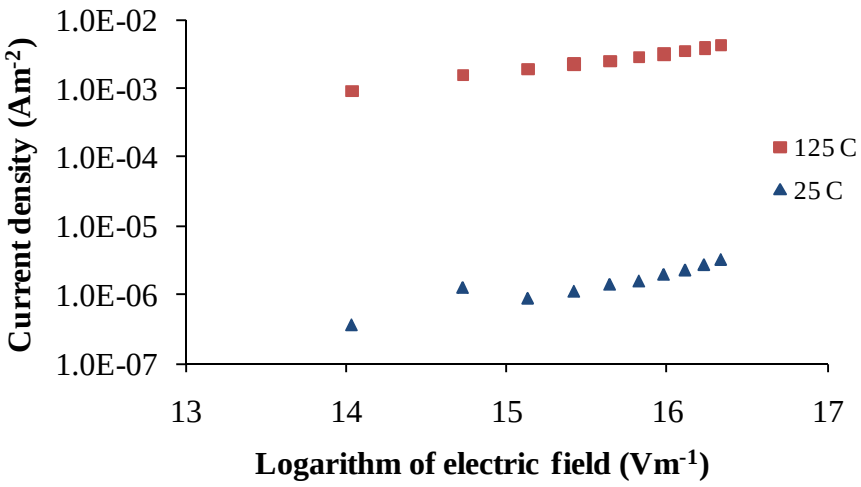


***Figure 7-4.*** *Logarithm of current density versus logarithm of electric field at various temperatures.*

Plots of current density (on log scale) versus logarithm of electric field at 25°C and 125°C are shown in Figure 7-4 and appear to be straight lines. The behavior at intermediate temperatures was also the same. Linear regression was performed to obtain the value of the electric field exponent (*p*) at all temperatures and the mean values for the three capacitors are shown in Figure 7-5. Since the values of *p* are close to 1 it can be said that the current follows the Ohm's law.

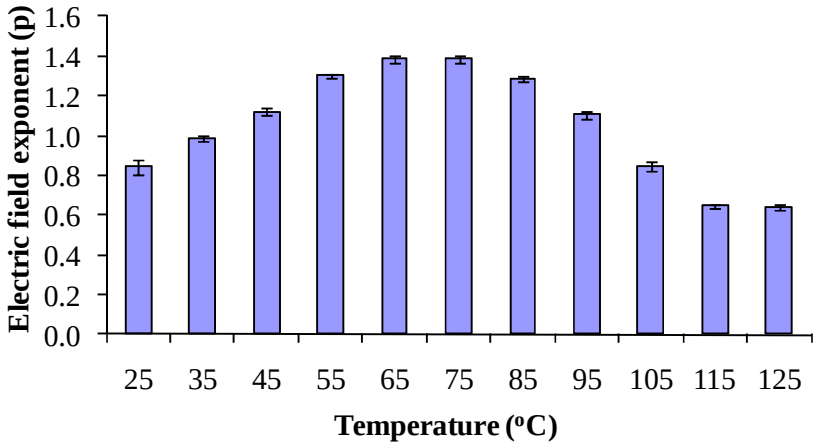


***Figure 7-5.*** *Electric field exponent (p) at various temperatures.*

## 7.3 Evaluation of Arrhenius behavior

Previous studies of leakage current in barium titanate [52][53], polymer [54], and a composite dielectric of PVC and $BaTiO_3$ [55] found the current to follow the Arrhenius relationship. The temperature dependence of the steady state current density ($J$) is analyzed for Arrhenius behavior. The Arrhenius relationship is of the form:

$$J = J_o \exp\left(-\frac{E_a}{kT}\right) \tag{18}$$

where $J_o$ is a constant, $E_a$ is the activation energy, $k$ is the Boltzmann constant, and $T$ is the absolute temperature. At a fixed voltage, the logarithm of current versus reciprocal of absolute temperature should produce a straight line with a slope of ($-E_a/k$) to follow the Arrhenius relationship. It is observed that the Arrhenius plot is not a straight line as shown in Figure 7-6 at 10 V and 100 V. The behavior at intermediate voltages was also found to be the same.

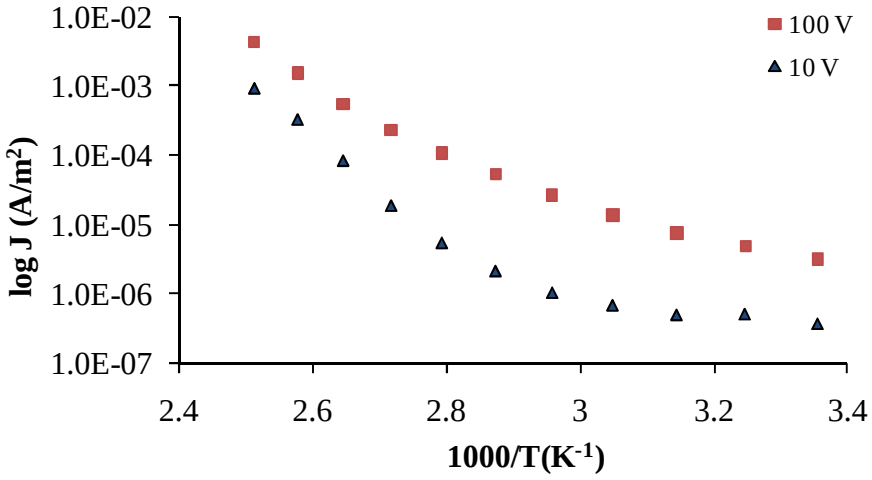


***Figure 7-6.*** *Logarithm of current density versus reciprocal of absolute temperature at various voltages.*

A curved Arrhenius plot (which leads to a non-uniform $E_a$ throughout the temperature range) can be due to a change in the mechanism of current conduction. It is possible that there are two conduction mechanisms, one of which is dominant in the high temperature and other in the low temperature region. Based on a survey of the literature this change may be due to a couple of possible reasons. One possible explanation is a change in the free volume of the polymer matrix at the glass transition temperature ($T_g$) that leads to a change in the current conduction mechanism [76]. But the change in mechanism in this case was not due to $T_g$ since the $T_g$ of the polymer was well above 125$^o$C. Another possibility can be a change from extrinsic to intrinsic charge carriers [77]. Extrinsic conduction is due to impurities in the material, whereas intrinsic conduction is due to conduction electrons and holes and other defects in the material (such as vacancies and interstitials). Extrinsic conduction is dominant in the low temperature region and intrinsic conduction is dominant in the high temperature region. But this mechanism is also not possible since the temperature at which intrinsic conduction is dominant in ceramics is generally much higher than 125$^o$C. This implies that the conduction of current does not follow the Arrhenius behavior in epoxy-$BaTiO_3$ composites.

## *7.4 Evaluation of Schottky, Poole-Frenkel and Hopping*

To investigate the mechanism of electrical conduction across this dielectric, various models of electrical conduction were evaluated. Among these mechanisms one or more mechanisms can be dominant depending on the material, applied temperature, or electric field. The conduction of current across the dielectric was evaluated for

consistency with Schottky emission (SE), the Poole-Frenkel (PF) mechanism, and ionic hopping (IH). Another conduction mechanism known as tunneling is not probable in this case since tunneling is a dominant conduction mechanism at an electric field higher than $10^8\,\mathrm{Vm}^{-1}$.

The functional dependence of current density on temperature at constant electric field can be used to identify the conduction mechanism. From the equations of Schottky emission, Poole-Frenkel and ionic hopping, the dependence of current density ($J$) on temperature ($T$) at constant electric field ($E = const.$) can be expressed as:

$$\left(J_{SE}\right)_{E=const.} = A_{SE}T^2 \exp\left(\frac{B_{SE}}{T}\right) \tag{19.1}$$

$$\left(J_{PF}\right)_{E=const.} = A_{PF} \exp\left(\frac{B_{PF}}{T}\right) \tag{19.2}$$

$$\left(J_{IH}\right)_{E=const.} = A_{IH} \exp\left(\frac{B_{IH}}{T}\right)\sinh\left(\frac{C_{IH}}{T}\right) \tag{19.3}$$

where A, B, C are constants and the subscripts SE, PF, and IH refer to Schottky emission, Poole-Frenkel and ionic hopping respectively. It can be seen from equation 9 that the Poole-Frenkel mechanism leads to Arrhenius behavior. It has already been shown that the conduction does not follow Arrhenius behavior (Figure 7-6) which means that the Poole-Frenkel mechanism is not the dominant conduction mechanism in the current case. The equations for SE (equation 8) and IH (equation 10) have a modified Arrhenius behavior with an additional term of $T^2$ and $\sinh(C_{IH}/T)$ respectively and might be the dominant conduction mechanisms in this material.

Regression was performed on the experimental values of current density versus temperature at constant electric field to evaluate the constants for Schottky emission and

the ionic hopping mechanism ($A_{SE}$, $B_{SE}$, $A_{IH}$, $B_{IH}$, *and* $C_{IH}$). This process was performed at all measured voltage steps starting from 10 V to 100V. Once the values of the constants were computed, the theoretical curves corresponding to Schottky emission and ionic hopping were obtained. In Figure 7-7 the curves corresponding to Schottky emission and ionic hopping are shown along with the actual experimental data at 10 V. It was observed that the best fit curve was that corresponding to the Schottky emission with a goodness of fit ≈ 0.98. The goodness of fit for ionic hopping mechanism was found to be ≈ 0.89. Similar behavior was obtained at other voltages also. This implies that the dominant conduction mechanism in this composite is Schottky emission followed by ionic hopping mechanism.

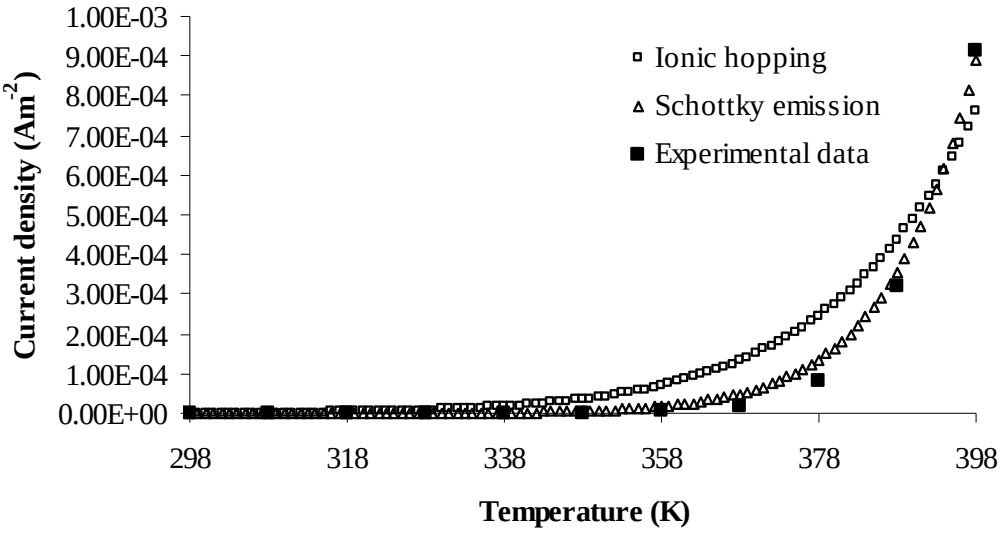


***Figure 7-7.*** *Validation of ionic hopping and Schottky emission.*

The mechanism of Schottky emission was cross-checked by performing further analysis. For the current to follow the Schottky emission, a plot of logarithm of current density versus square root of electric field should be a straight line (with a slope of

$\beta_{SE}/kT$) at constant temperature. In Figure 7-8 the relationship between current density (on a log scale) and the square root of electric field at 25°C and 125°C appears to be a straight line. Similar behavior was observed at other temperatures in between 25°C and 125°C.

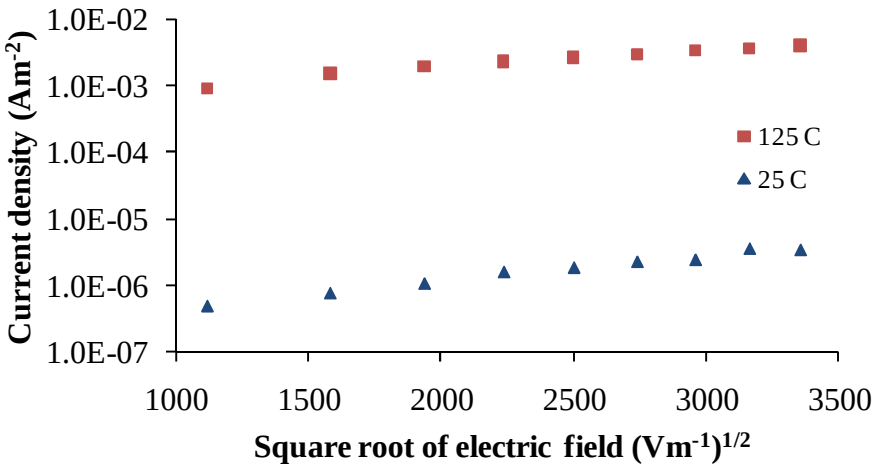


***Figure 7-8.*** *Logarithm of current density versus square root of electric field at various temperatures.*

To further confirm the possibility of Schottky emission, the dielectric constant ($\varepsilon$) was calculated from the values of $\beta_{SE}$. The values of $\beta_{SE}$ at different temperatures were obtained by regression. The values of the calculated dielectric constant at various temperatures are shown in Figure 7-9. The dielectric constant values obtained are closer to the dielectric constant of pure epoxy resin instead of the epoxy-$BaTiO_3$ composite. This difference can be explained by considering the location of Schottky emission which takes place at the interface of the electrode and the dielectric material. It is possible that at regions very close to the electrode, only epoxy resin is present so at the interface the properties of epoxy resin dominate over the properties of the composite.

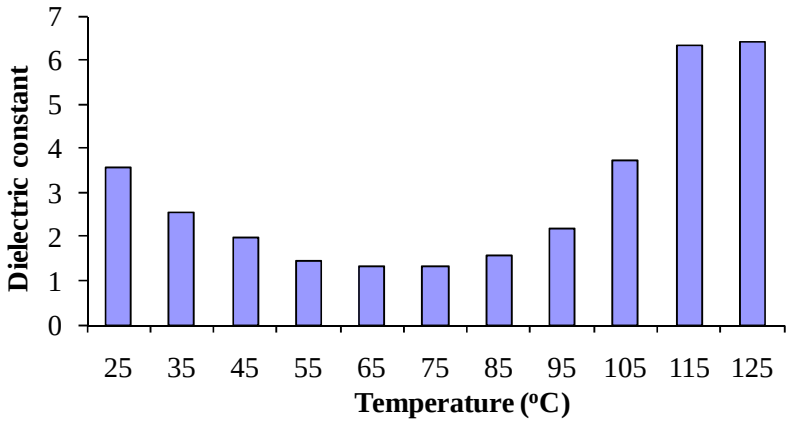


***Figure 7-9.*** *Dielectric constant calculated from the leakage current data assuming Schottky emission at various temperatures.*

3D regression of the leakage current data over the given temperature and voltage range was performed to calculate the constants of the Schottky emission as shown in Figure 7-10. The goodness of fit ($r^2$) was close to 0.98. The values of the Richardson constant ($A$), dielectric constant ($\varepsilon$), and contact potential barrier ($\phi_{SE}$) were found to be $1.17 \times 10^6$ A $m^{-2}$ $k^{-2}$, 4.42 and 1.14 eV respectively.

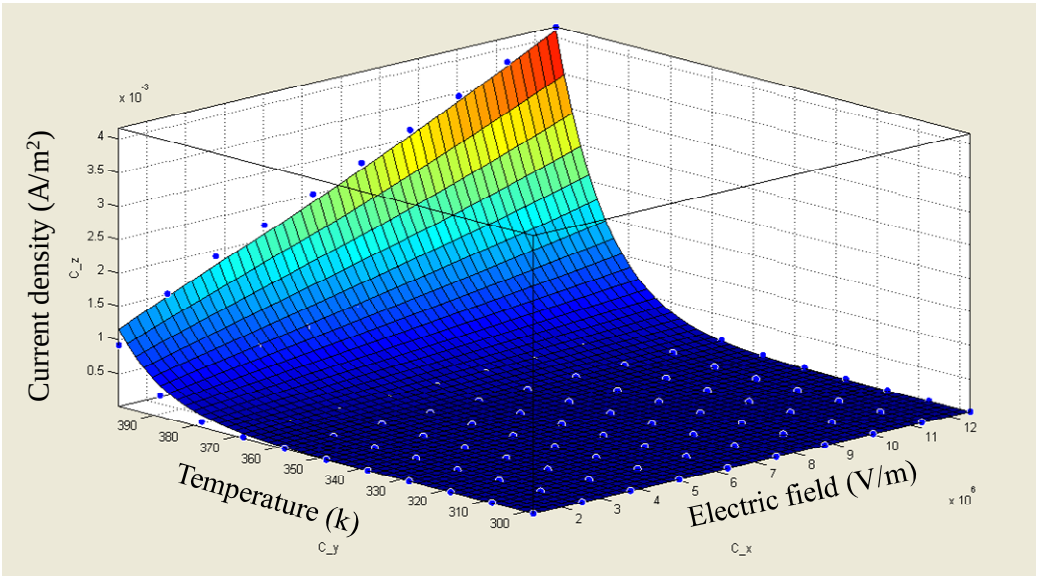


***Figure 7-10.*** *3D regression of the leakage current data to calculate the constants of Schottky emission.*

Since ionic hopping was also a possible conduction mechanism, 3D regression of the leakage current data was performed to calculate the activation energy of ionic hopping. The goodness of fit ($r^2$) for ionic hopping was close to 0.96. The activation energy ($E_a$) of ionic hopping was found to be 1.04 eV.

# 8. Conduction mechanisms in a fabricated capacitor

## *8.1 Measurement of leakage current*

The leakage current across the capacitor (fabricated Cu/dielectric/Cu structure) was measured using an Agilent 4155C Semiconductor parameter analyzer (Figure 7-1) as a function of voltage. The voltage was sweeped from 0 to 50 V in steps of 1 volt. Leakage current was measured 1 second after each step change of voltage, allowing ample time for the current to stabilize. This voltage sweep was repeated over the temperature range of 25$^{o}$C to 125$^{o}$C in increments of 5$^{o}$C. Once the voltage sweep at a given temperature was performed, the temperature was raised by 5$^{o}$C and voltage sweep at the next temperature was performed after 5 minutes, allowing sufficient time for the temperature to stabilize. The temperature of the test board was controlled using a Thermostream (air stream temperature forcing system from Temptronic Corporation) which is shown in Figure 7-2.

Atypical plot of leakage current in 3D as a function of temperature and voltage is shown in Figure 8-1 for the capacitor with 0% loading of $BaTiO_3$. Similarly measurements were performed for all other loading conditions.

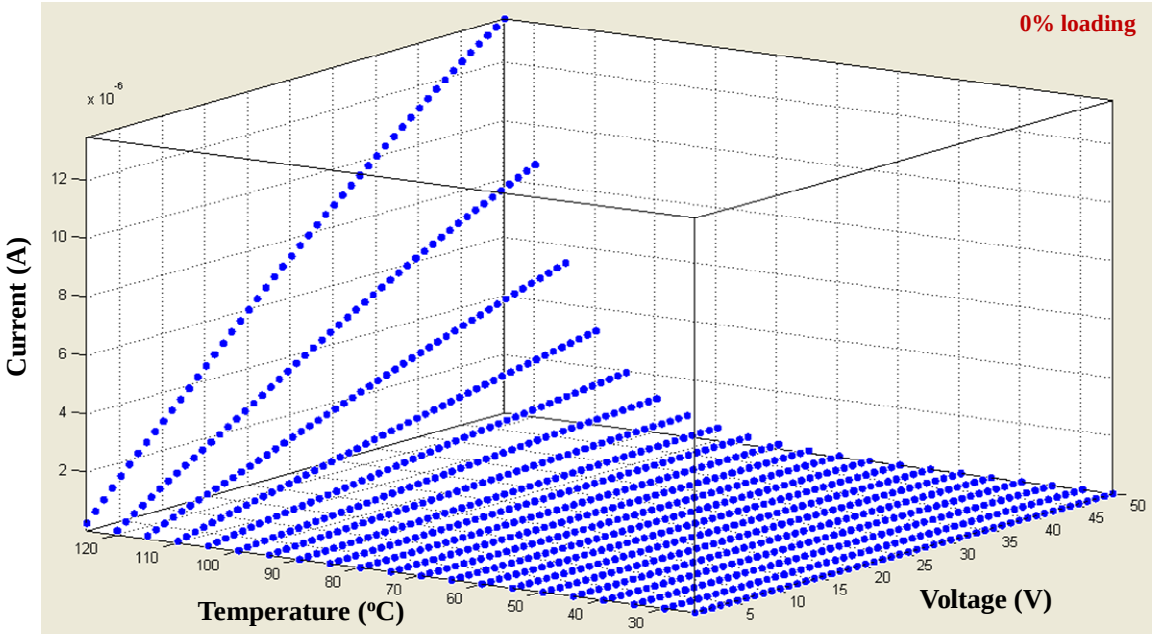


***Figure 8-1.*** *Leakage current as a function of temperature and voltage for one capacitor with 0% loading of $BaTiO_3$.*

The value of leakage current was found to increase with an increase in the ceramic loading and with an increase in the diameter of ceramic particles. Current versus voltage plots of one capacitor (at different loading conditions) at 25°C and 125°C are shown in Figure 8-2, Figure 8-3, Figure 8-4, and Figure 8-5. Similar behavior was observed at other temperatures also.

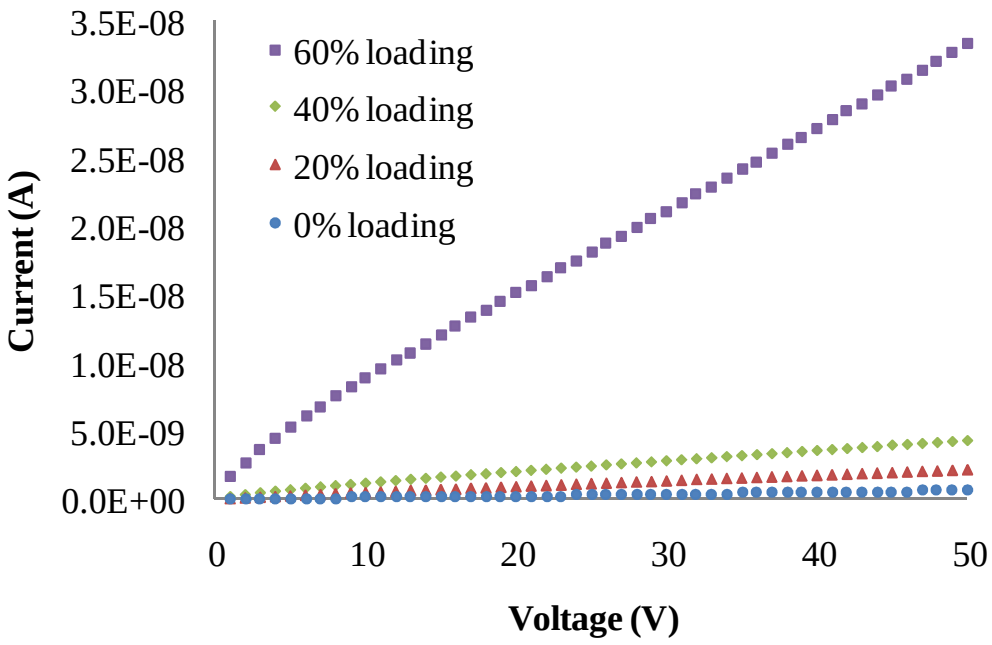


***Figure 8-2.*** *Current versus voltage plots (at 25$^{o}$C ) at various $BaTiO_3$ loading conditions (vol. %) for one capacitor.*

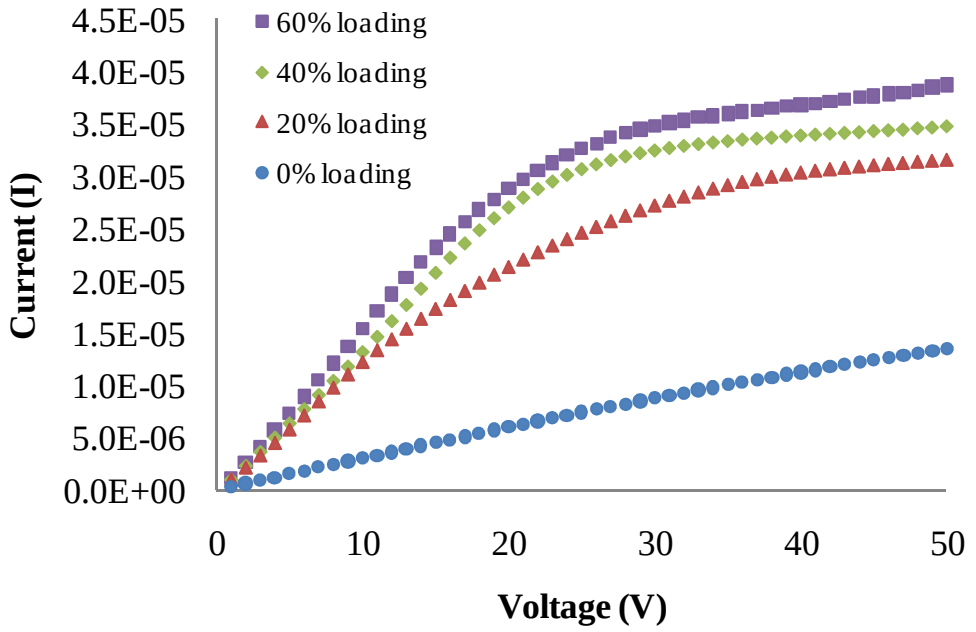


***Figure 8-3.*** *Current versus voltage plots (at 125$^{o}$C) at various $BaTiO_3$ loading conditions (vol %) for one capacitor.*

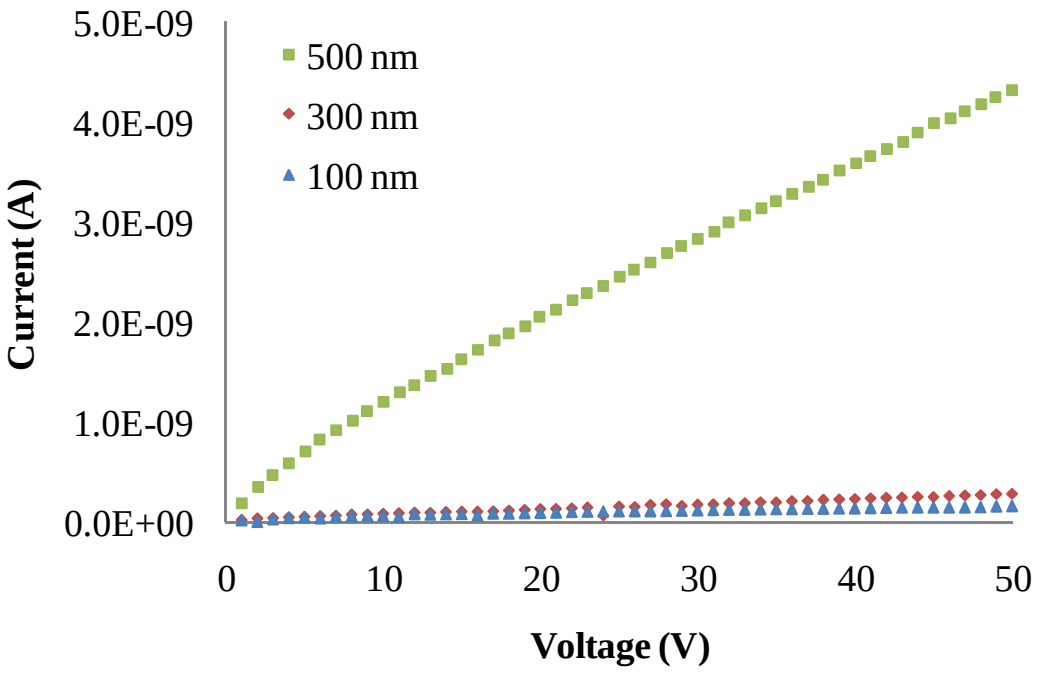


***Figure 8-4.*** *Current versus voltage plots (at 25°C) for various diameters of $BaTiO_3$ particles for one capacitor.*

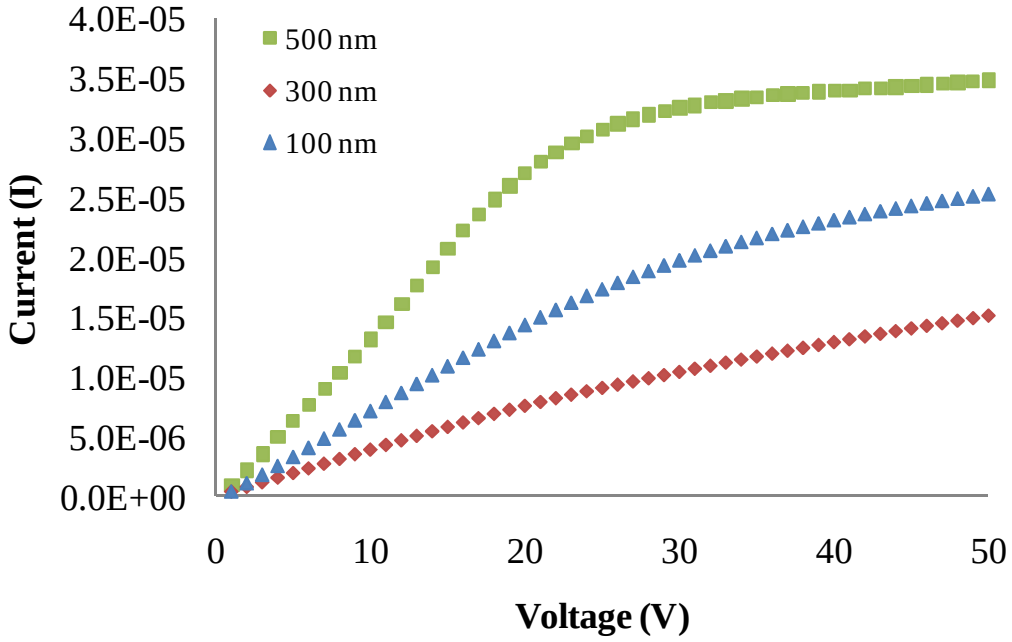


***Figure 8-5.*** *Current versus voltage plots (at 125°C) for various diameters of $BaTiO_3$ particles for one capacitor.*

Leakage current was found to increase with an increase in temperature. Current versus temperature plots of one capacitor (at different loading conditions) at 1 V and 50V are shown in Figure 8-6, Figure 8-7, Figure 8-8, and Figure 8-9. Similar behavior was observed at other voltages also.

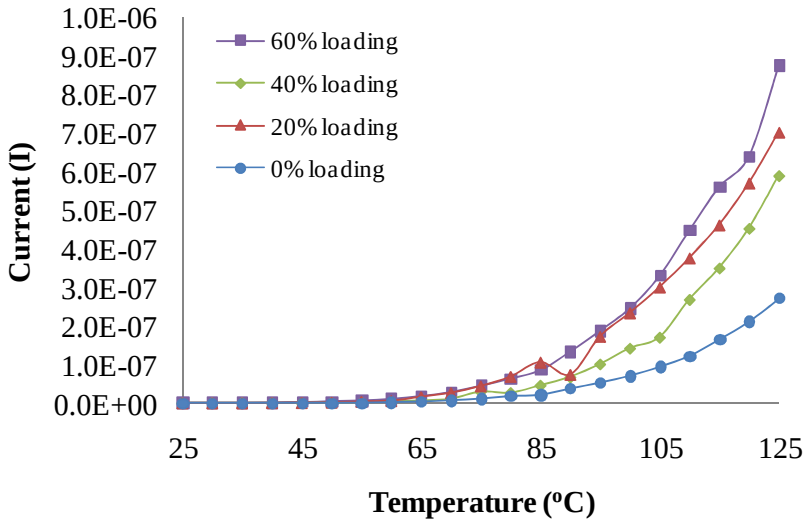


***Figure 8-6.*** *Current versus temperature plots (at 1V) at various $BaTiO_3$ loading conditions (vol %) for one capacitor.*

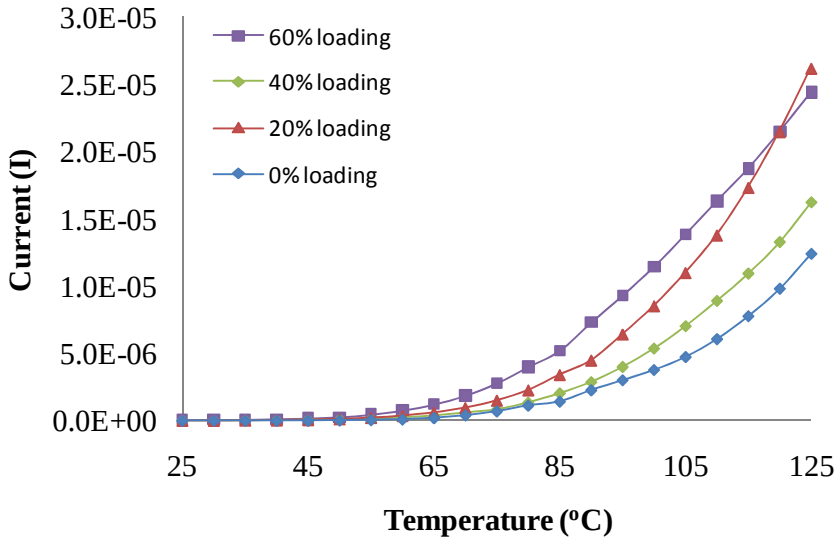


***Figure 8-7.*** *Current versus temperature plots (at 50V) at various $BaTiO_3$ loading conditions (vol %) for one capacitor.*

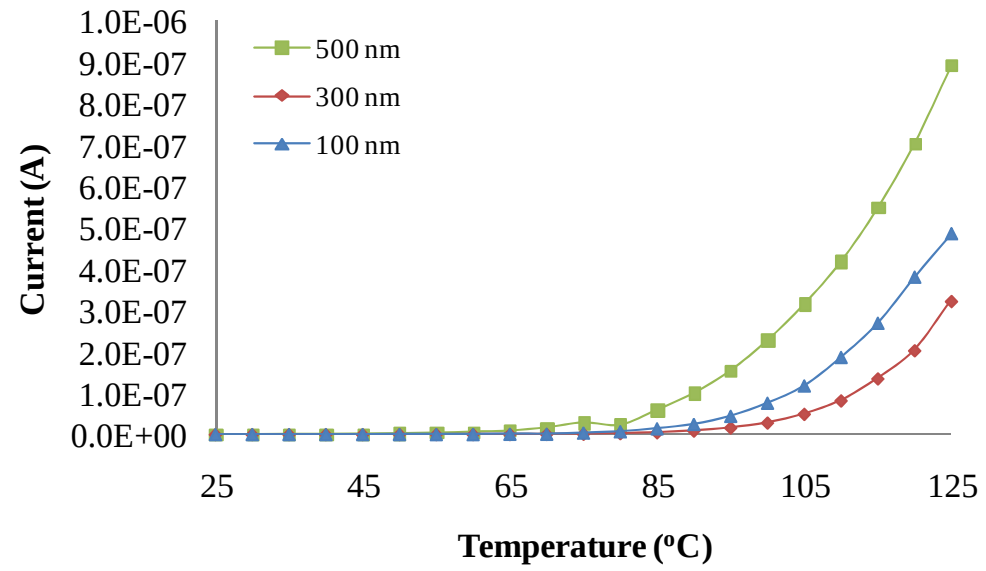


***Figure 8-8.*** *Current versus temperature plots (at 1V) for various diameters of $BaTiO_3$ particles for one capacitor.*

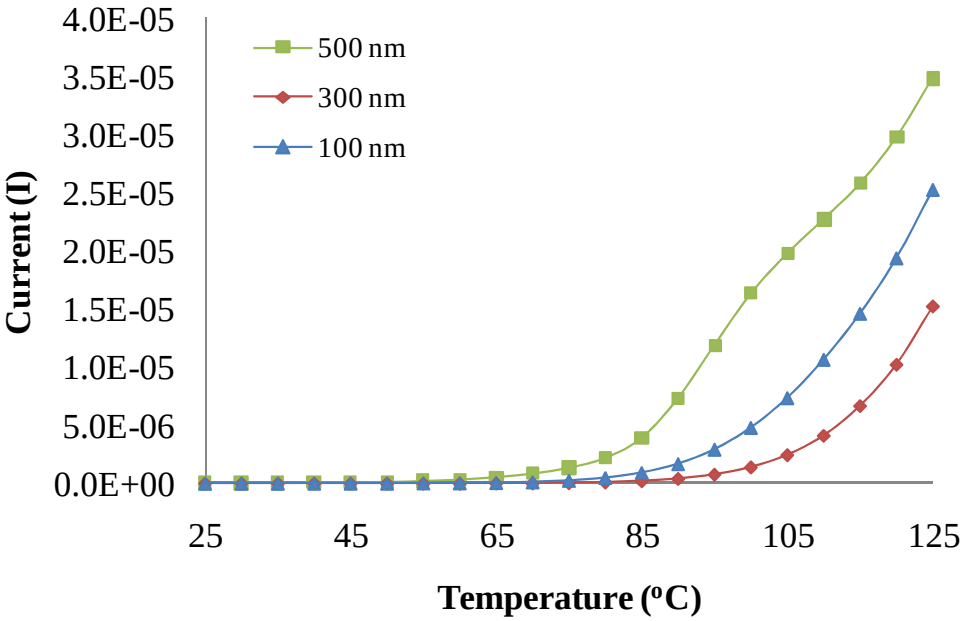


***Figure 8-9.*** *Current versus temperature plots (at 50 V) for various diameters of $BaTiO_3$ particles for one capacitor.*

## 8.2 Evaluation of Ohmic behavior

The conduction of current at a constant temperature is checked for Ohmic behavior. A plot of logarithm of current density versus logarithm of electric field should produce straight lines (at a constant temperature) with a slope (electric field exponent) of 1 if the current follows Ohm's law.

A plot of logarithm of current density versus logarithm of electric field produced straight lines under most of the loading and temperature conditions as shown in Figure 8-10, Figure 8-11, Figure 8-12, and Figure 8-13. However, some deviations from straight line were observed at high temperatures when the ceramic loading was high. Deviations from straight line in this plot imply that the value of electric field exponent (*p*) is changing with voltage.

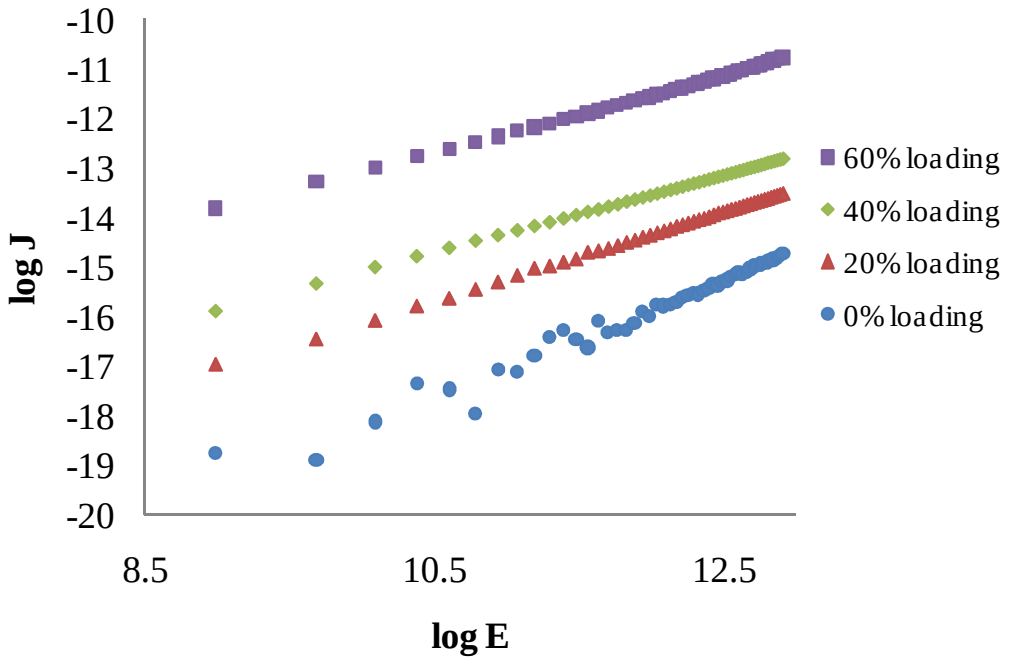


***Figure 8-10.*** *Logarithm of current density versus logarithm of electric field (at 25 $^{o}$C) at various $BaTiO_3$ loading conditions (vol. %) for one capacitor.*

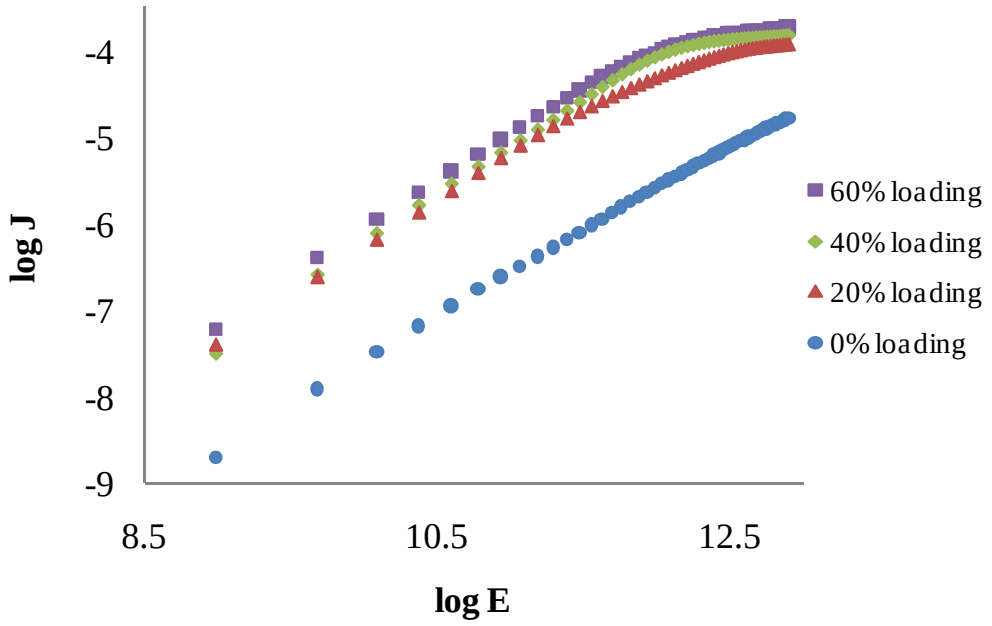


***Figure 8-11.*** *Logarithm of current density versus logarithm of electric field (at 125 $^{o}$C) at various $BaTiO_3$ loading conditions (vol. %) for one capacitor.*

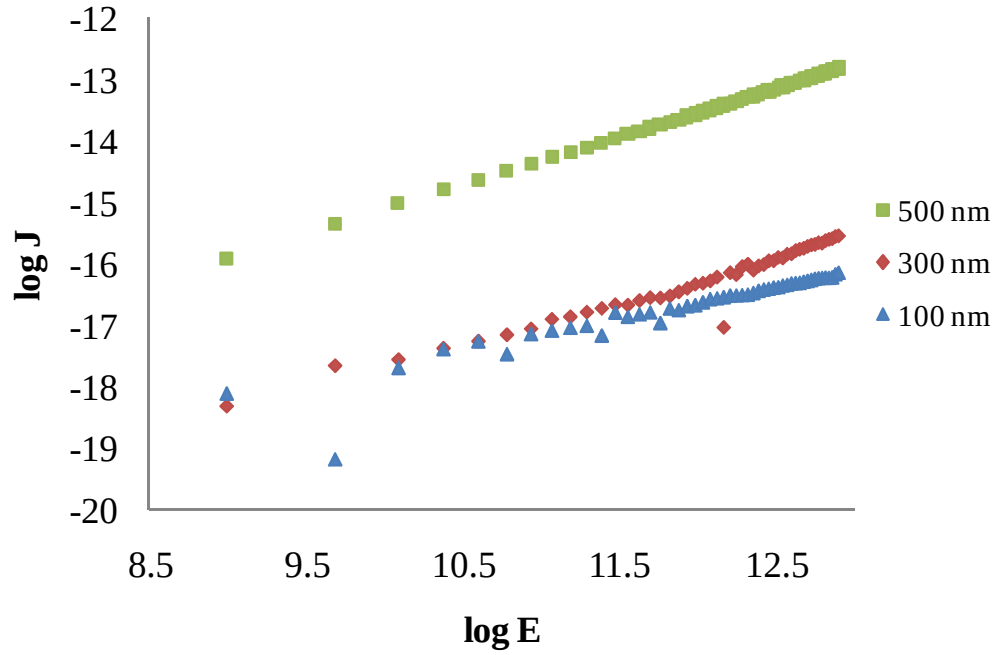


***Figure 8-12.*** *Logarithm of current density versus logarithm of electric field (at 25 $^{o}$C) for various diameters of $BaTiO_3$ particles for one capacitor.*

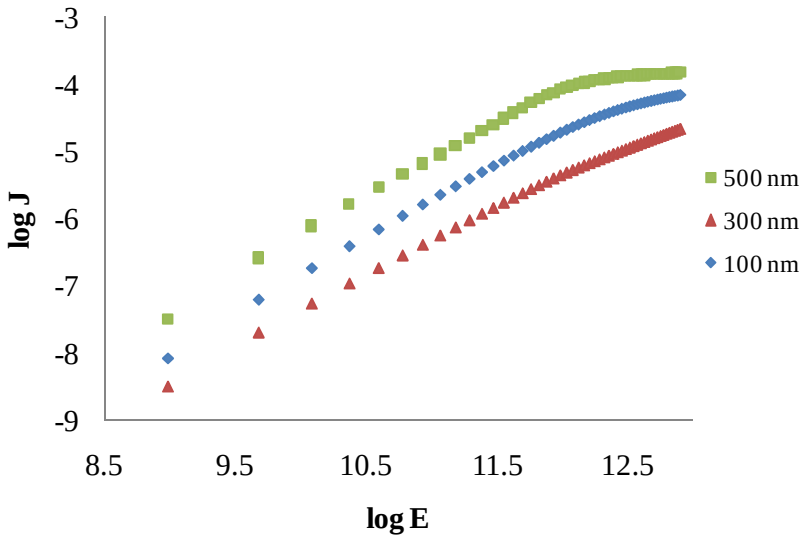


***Figure 8-13.*** *Logarithm of current density versus logarithm of electric field (at 125 $^{o}C$) for various diameters of $BaTiO_3$ particles for one capacitor.*

Linear regression was performed to obtain the value of the electric field exponent (*p*) at all temperatures and loading conditions. The mean values of *p* are shown in Figure 8-14 and Figure 8-15. Since the values of *p* are close to 1 it can be said that the current follows the Ohm's law.

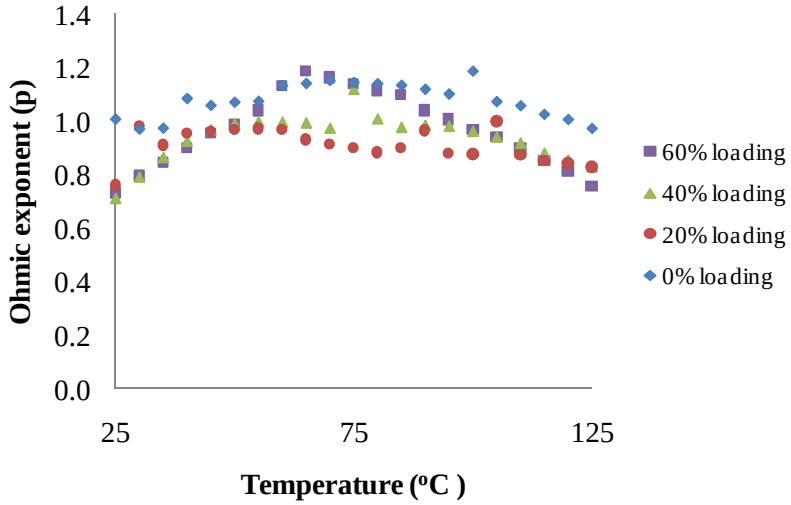


***Figure 8-14.*** *Mean value of the electric field exponent (p) at various loading conditions of $BaTiO_3$ (vol. %) at different temperatures.*

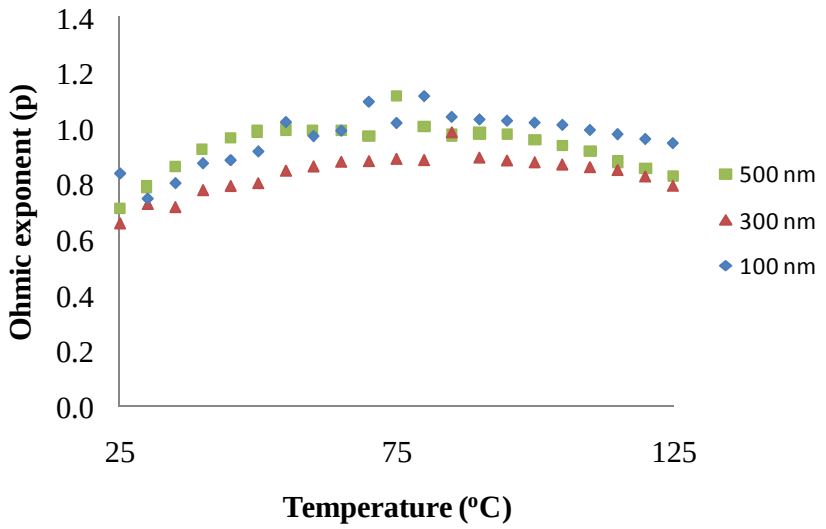


***Figure 8-15.*** *Mean value of the electric field exponent (p) for various diameters of $BaTiO_3$ particles at different temperatures.*

## 8.3 Evaluation of Schottky and Poole-Frenkel mechanism

For the conduction of current to follow Schottky or Poole-Frenkel mechanism, a plot of logarithm of current density ($J$) versus square root of electric field (E) should produce straight lines at all temperatures. The slope ($m$) of this straight line can be used to calculate the dielectric constant ($\varepsilon$) of the material and compared with the actual dielectric constant of the material.

$$\varepsilon_{SE} = \frac{e^3}{4\pi\varepsilon_o (kTm)^{0.5}} \tag{20.1}$$

$$\varepsilon_{PF} = \frac{e^3}{\pi\varepsilon_o (kTm)^{0.5}} \tag{20.1}$$

where $\varepsilon_{SE}$ is the dielectric constant if Schottky emission is assumed, $\varepsilon_{PF}$ is the dielectric constant if Poole-Frenkel emission is assumed, $e$ is the charge on an electron, $\varepsilon_o$ is the permittivity of the free space, $k$ is the Boltzmann constant, and $T$ is the absolute temperature. Plots of logarithm of current density ($J$) versus square root of electric field ($E$) were found to be curved lines at 25°C and 125°C as shown in Figure 8-16, Figure 8-17, Figure 8-18, and Figure 8-19. Similar behavior was observed at other temperatures also.

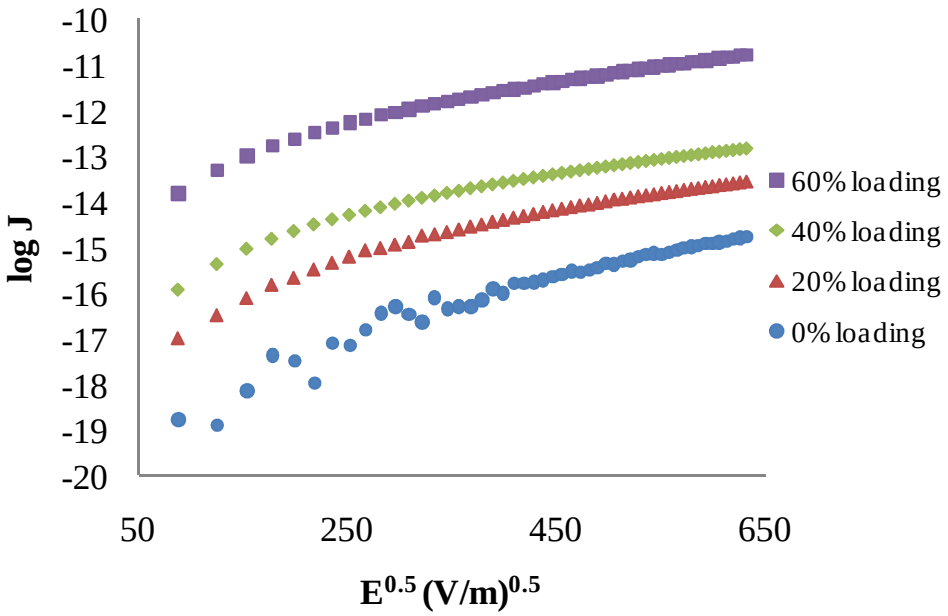


***Figure 8-16.*** *Logarithm of current density versus square root of electric field (at 25 °C) at various $BaTiO_3$ loading conditions (vol. %) for one capacitor.*

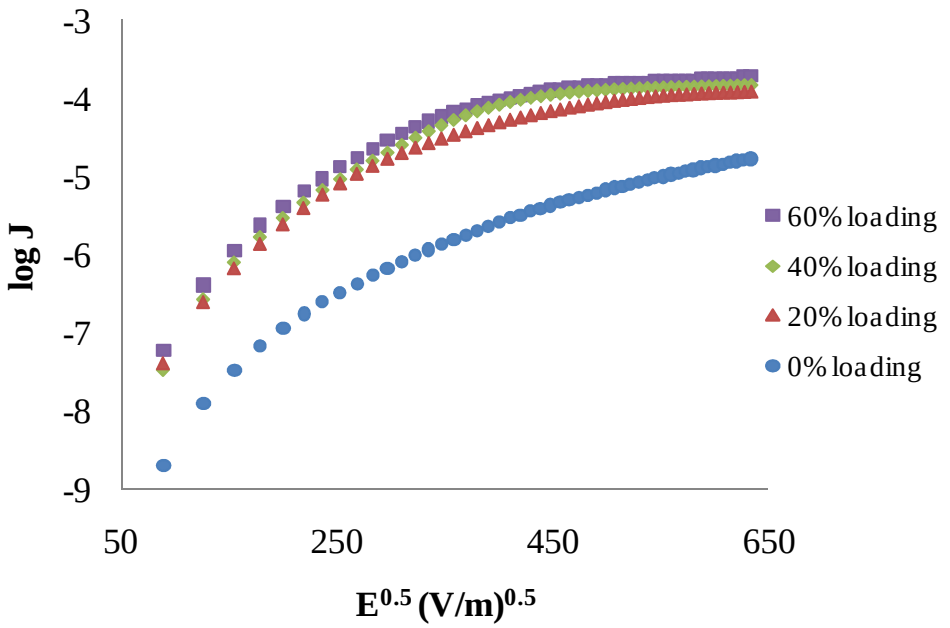


***Figure 8-17.*** *Logarithm of current density versus square root of electric field (at 125 $^{o}$C) at various $BaTiO_3$ loading conditions (vol. %) for one capacitor.*

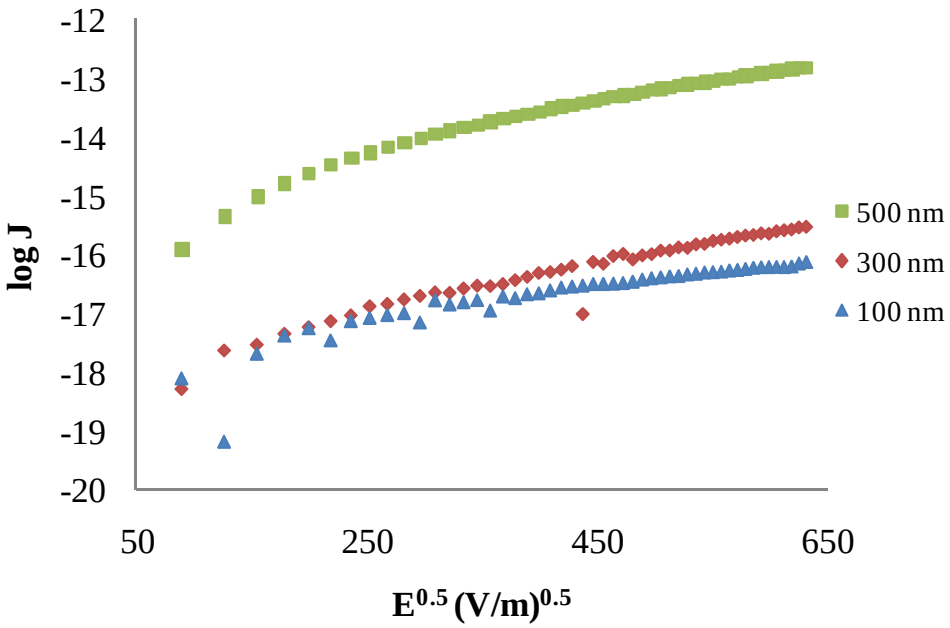


***Figure 8-18.*** *Logarithm of current density versus square root of electric field (at 25 $^{o}$C) for various diameters of $BaTiO_3$ particles for one capacitor.*

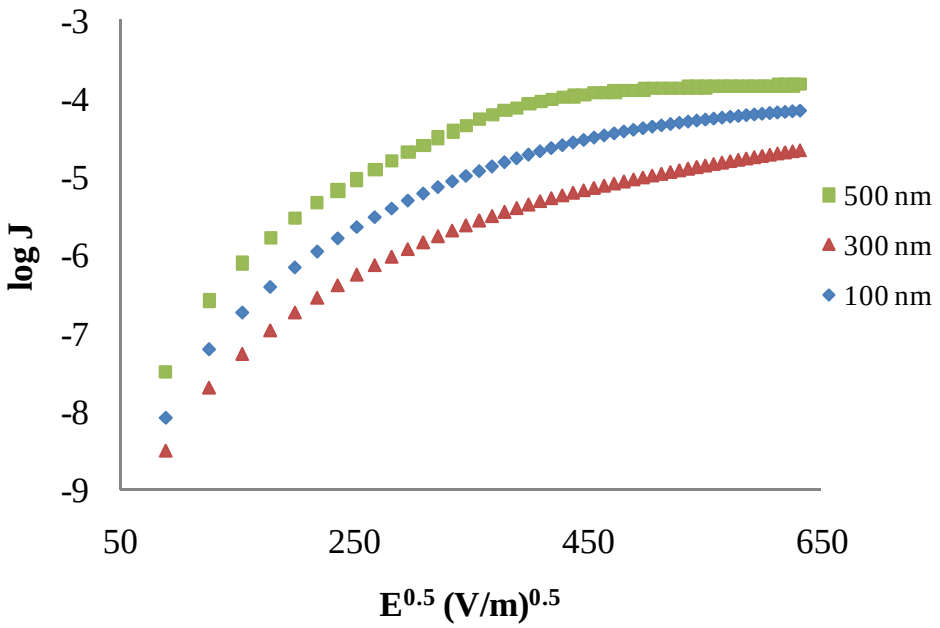


***Figure 8-19.*** *Logarithm of current density versus square root of electric field (at 125 $^{o}$C) for various diameters of $BaTiO_3$ particles for one capacitor.*

The values of dielectric constant assuming Schottky emission and Poole Frenkel were calculated for all loading conditions and at all temperatures and is shown in Figure 8-20, Figure 8-21, Figure 8-22, and Figure 8-23. It was observed that the calculated values of dielectric constant was about 1-2 orders of magnitude lower than the actual dielectric constant of the material. This implies that the conduction of current does not follow either Schottky or Poole-Frenkel in these materials.

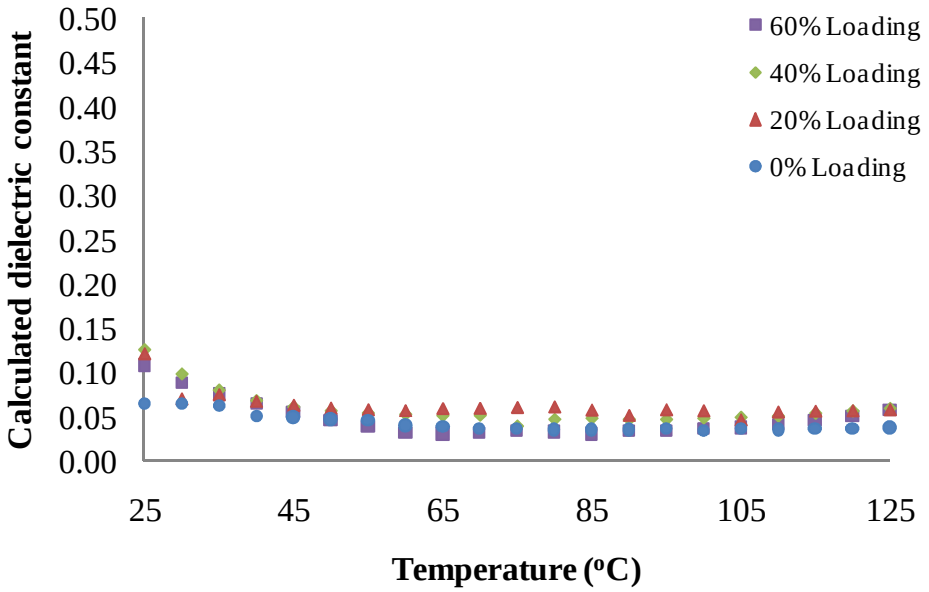


***Figure 8-20.*** *Calculated mean dielectric constant assuming Schottky emission for various loading conditions of $BaTiO_3$.*

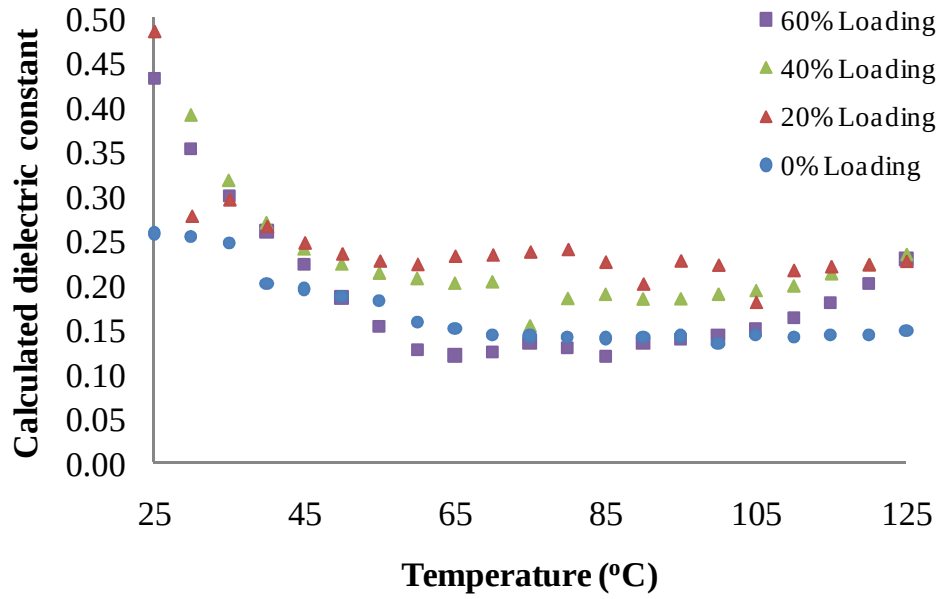


***Figure 8-21.*** *Calculated mean dielectric constant assuming Poole-Frenkel emission for various loading conditions of $BaTiO_3$.*

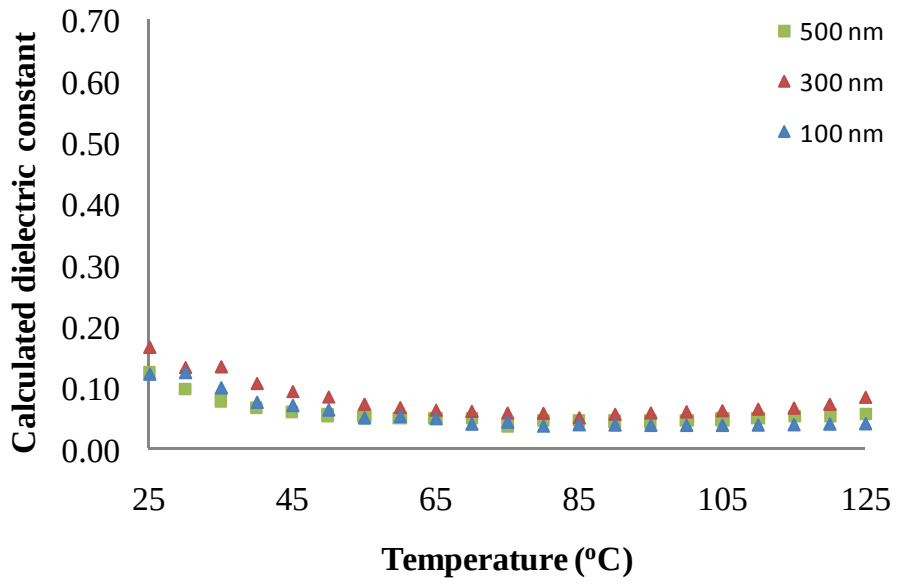


***Figure 8-22.*** *Calculated mean dielectric constant assuming Schottky emission for various diameters of $BaTiO_3$ particles.*

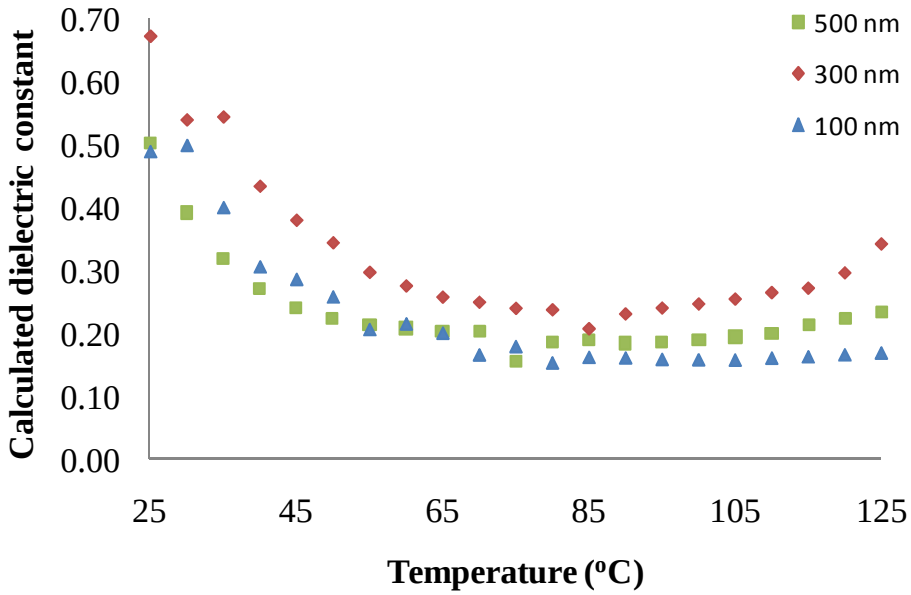


***Figure 8-23.*** *Calculated mean dielectric constant assuming Poole-Frenkel emission for various diameters of $BaTiO_3$ particles.*

## 8.4 Evaluation of hopping mechanism

The mechanism of conduction can be hopping since Ohmic conduction can lead to hopping under certain conditions. This happens at low electric field when the hyperbolic sine term in the hopping equation becomes insignificant (i.e. sinh(x) ~ x). When this condition is satisfied, hopping may lead to Ohmic conduction or vice versa as shown in the following equation:

$$J = 2nd\nu \exp\left(-\frac{E_a}{kT}\right)\sinh\left(\frac{eEd}{2kT}\right) \approx \left[\left(\frac{ne\nu d^2}{k}\right)\frac{1}{T}\exp\left(-\frac{E_a}{kT}\right)\right]E = \sigma E \qquad (21)$$

In the current case, the maximum value of the term inside the hyperbolic sine term is equal to 0.0078 hence the above approximation seems to hold here.

$$\sinh\left(\frac{eEd}{2kT}\right) = \left(\frac{1.6\times10^{-19}\times50\times10^{-9}}{2\times1.38\times10^{-23}\times298\times125\times10^{-6}}\right) = \sinh(0.0078) = 0.0078$$

where the charge on an electron ($e$) is equal to $1.6\times10^{-19}$, the maximum electric field ($E$) is equal to $50/125\times10^{-6}$ V/m, the hopping distance is of the order of nanometers, the value of the Boltzmann constant ($k$) is equal to $1.38\times10^{-23}$, and the minimum temperature ($T$) is equal to 298 K. Using the above approximation the modified equation of hopping is:

$$J \approx C\left(\frac{E}{T}\right)\exp\left(-\frac{E_a}{kT}\right) \qquad (22)$$

where $C$ is a constant. For the current to follow hopping conduction plots of logarithm of $JT$ (product of current density and absolute temperature) versus $1/T$ (reciprocal of absolute temperature) should produce straight lines at constant electric field. These plots produced nearly straight lines at 1 V and 50V and are shown in Figure 8-24, Figure 8-25,

Figure 8-26, and Figure 8-27. Similar behavior was observed at other voltages also implying that the conduction mechanism is hopping in these materials.

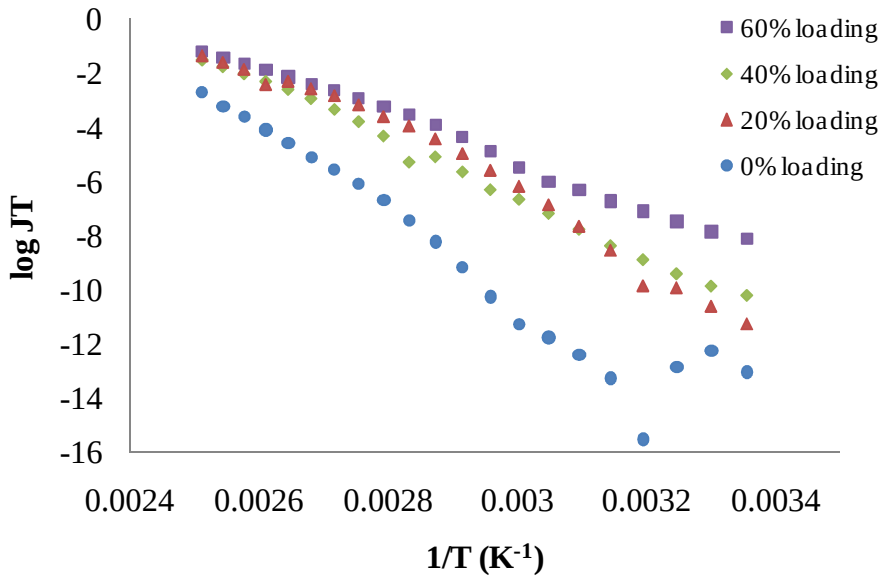


***Figure 8-24.*** *Log JT versus (1/T) at 1V for various loading conditions of $BaTiO_3$ (vol. %) for one capacitor.*

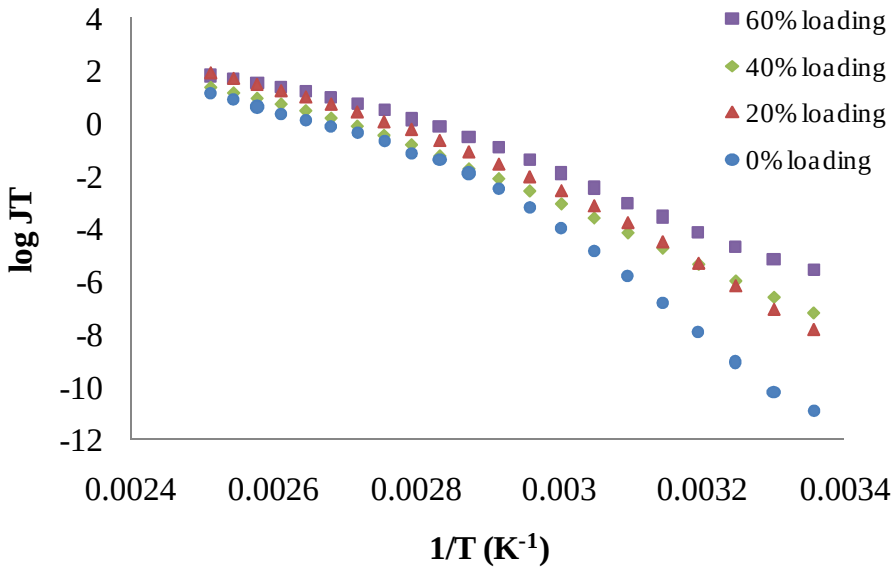


***Figure 8-25.*** *Log JT versus (1/T) at 50 V for various loading conditions of $BaTiO_3$ (vol. %) for one capacitor.*

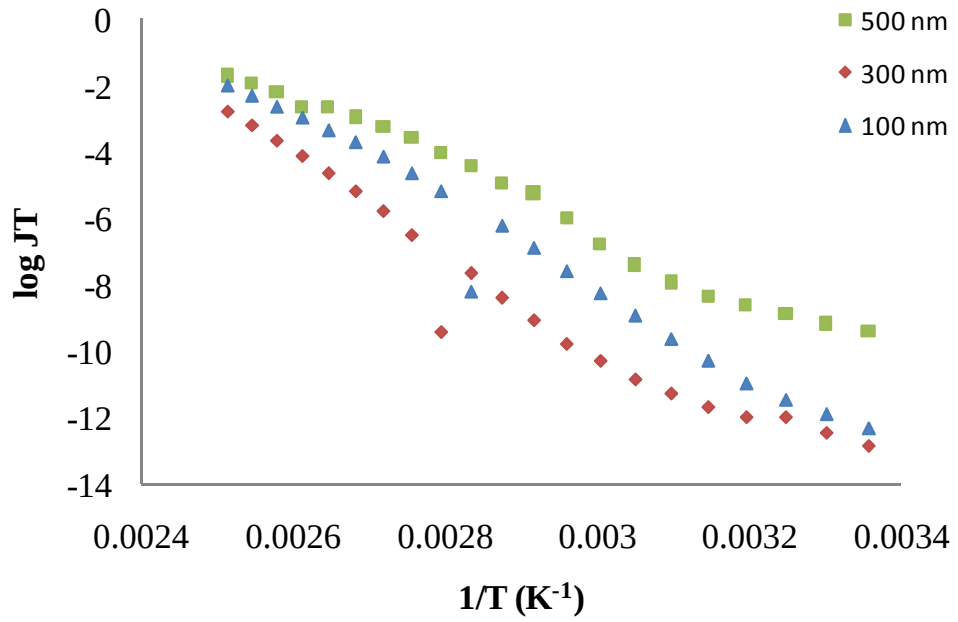


***Figure 8-26.*** *Log JT versus (1/T) at 1 V for various diameters of $BaTiO_3$ particles for one capacitor.*

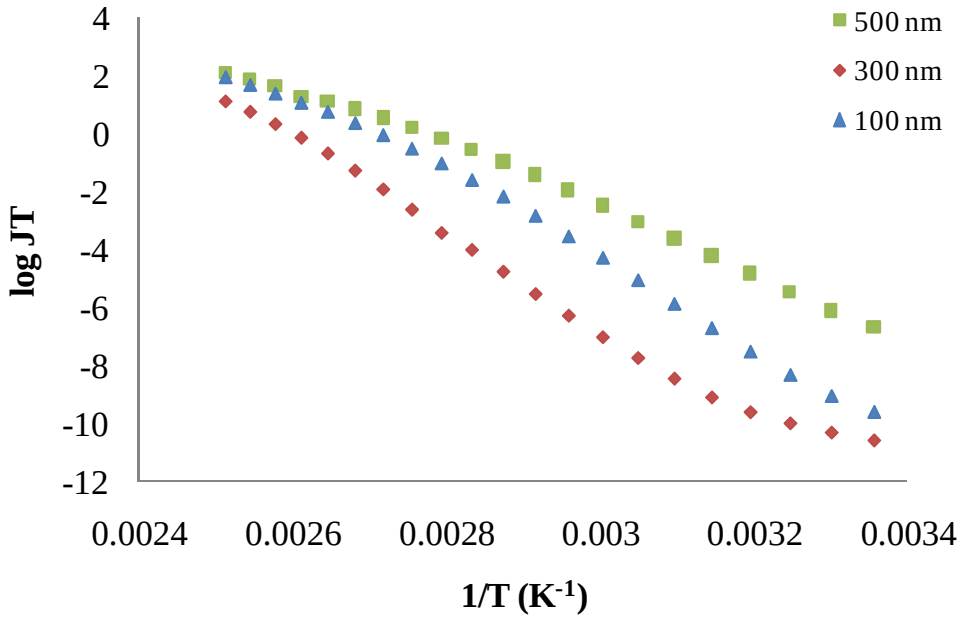


***Figure 8-27.*** *Log JT versus (1/T) at 50 V for various diameters of $BaTiO_3$ particles for one capacitor.*

### 8.4.1 Activation energy of hopping

The value of activation energy ($E_a$) of the hopping mechanism was computed for all loading conditions by performing 3D regression of the leakage current data as shown in Figure 8-28. It was observed that $E_a$ decreased with an increase in the ceramic loading and with an increase in the ceramic particle diameter as shown in Figure 8-29 and Figure 8-30 respectively. The goodness of fit ($R^2$) and the activation energy ($E_a$) of the hopping mechanism are shown in Table 8-1 and Table 8-2 respectively. The goodness of fit and the activation energy for the dielectric material with 0% loading of $BaTiO_3$ was found to be 0.96 and 0.94 eV respectively.

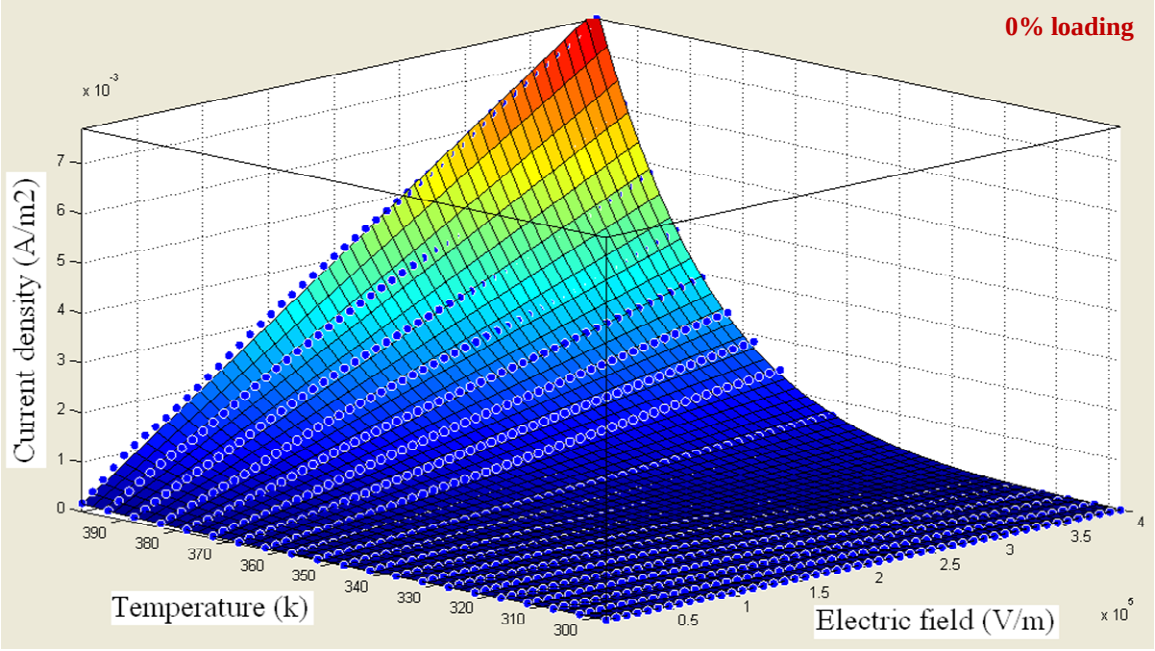


***Figure 8-28.*** *3D regression of the leakage current data to calculate the activation energy of the hopping mechanism for one capacitor with 0% loading.*

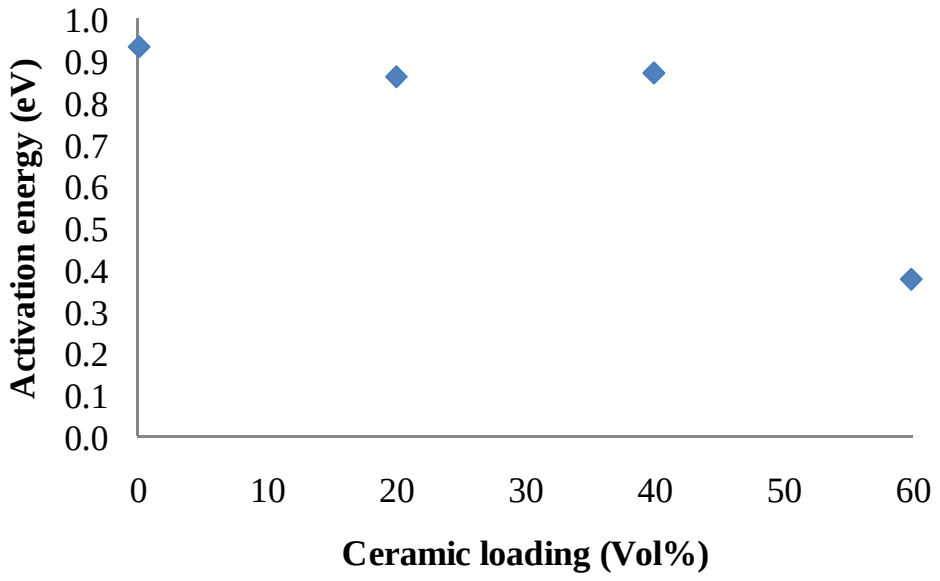


***Figure 8-29.*** *Mean activation energy of hopping as a function of $BaTiO_3$ loading (for diameter of $BaTiO_3$ particles equal to 500 nm).*

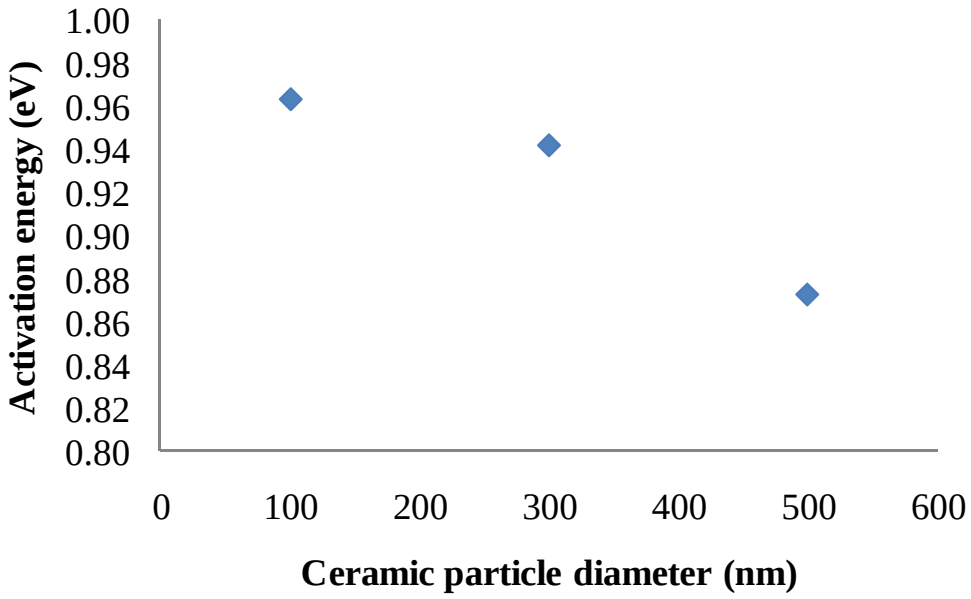


***Figure 8-30.*** *Mean activation energy of hopping as a function of diameter of $BaTiO_3$ particles (at 40% loading of $BaTiO_3$ particles by volume).*

***Table 8-1.*** *Goodness of fit ($R^2$ ) of regression*

| | | $BaTiO_3$ particle diameter (nm) | | |
|---|---|---|---|---|
| | | 100 | 300 | 500 |
| $BaTiO_3$ loading (Vol.%) | 20 | | | 0.99 |
| | 40 | 0.97 | 0.93 | 0.99 |
| | 60 | | | 0.92 |

***Table 8-2.*** *Activation energy ($E_a$ ) of the hopping mechanism in electron volts (eV)*

| | | $BaTiO_3$ particle diameter (nm) | | |
|---|---|---|---|---|
| | | 100 | 300 | 500 |
| $BaTiO_3$ loading (Vol.%) | 20 | | | 0.86 |
| | 40 | 0.96 | 0.94 | 0.87 |
| | 60 | | | 0.38 |

## *8.5 Calculating the theoretical trend of activation energy*

### 8.5.1 As a function of ceramic loading

When two materials with different electrical conductivity ($\sigma$) are mixed together to form a composite material, the equivalent resistivity is given by the general mixing rule [78]. The most appropriate form of mixing rule for a composite (epoxy and $BaTiO_3$ in the current case) can be written as follows:

$$\sigma_{eq}^{\alpha} = v\sigma_c^{\alpha} + (1-v)\sigma_p^{\alpha} \tag{23}$$

where $\sigma_{eq}$ is the equivalent conductivity of the composite, $\sigma_c$ is the conductivity of the ceramic ($BaTiO_3$), $\sigma_p$ is the conductivity of the polymer (epoxy), $v$ is the loading fraction

by volume of the ceramic ($BaTiO_3$), and α is a constant. For ideal parallel arrangement of the components in the composite the value of $\alpha$ is equal to +1. For ideal series arrangement of the components in the composite the value of $\alpha$ is equal to -1. For real systems, the value of α lies between -1 and +1. A special case when the value of $\alpha$ is equal to 0, transforms the above equation into the Lichtenecker formula. The Lichtenecker formula is commonly used for two component composites and is given as:

$$\log \sigma_{eq} = v \log \sigma_c + (1 - v) \log \sigma_p \tag{24}$$

The applicability of the Lichtenecker equation at different voltages and temperature was investigated and is shown in Figure 8-31-Figure 8-34. It was observed that the equation was valid at all voltages (from 0 to 50 V) in the lower temperature region. But in the higher temperature region (~125$^o$C) some deviations were observed. The goodness of fit of regression is given in Table 8-3.

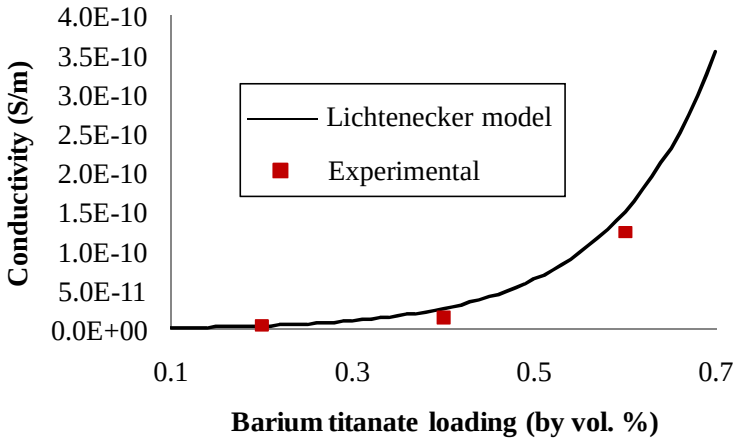


***Figure 8-31.*** *Applicability of Lichtenecker model at 25$^o$C and 1 V.*

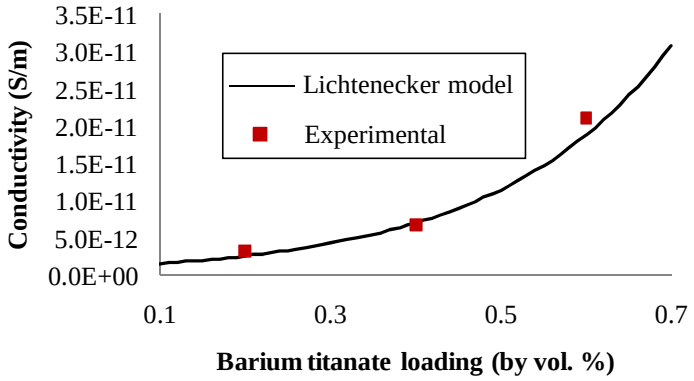


***Figure 8-32.*** *Applicability of Lichtenecker model at 25$^{o}$C and 50 V.*

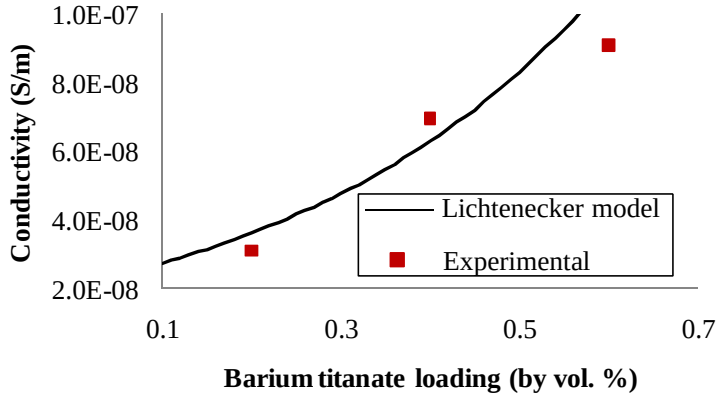


***Figure 8-33.*** *Applicability of Lichtenecker model at 125 $^{o}$C and 1 V.*

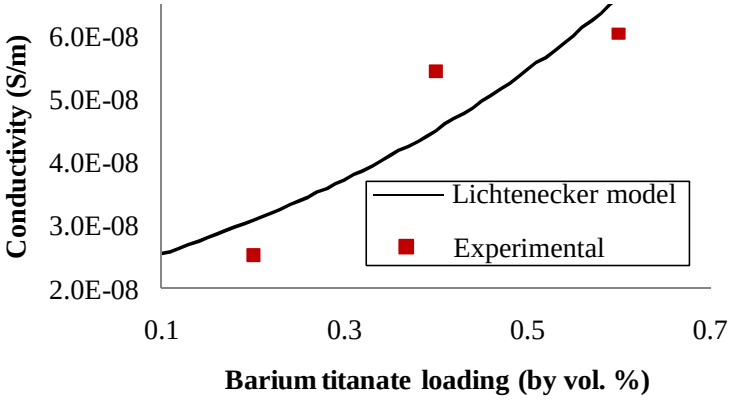


***Figure 8-34.*** *Applicability of Lichtenecker model at 125 $^{o}$C and 50 V.*

***Table 8-3.*** *Applicability of Lichtenecker model*

| Temperature and voltage conditions | R-square value |
|---|---|
| 25°C, 1V | 1.00 |
| 25°C, 50V | 0.96 |
| 125°C, 1V | 0.72 |
| 125°C, 50V | 0.87 |

The conductivity (σ) for the hopping mechanism as a function of temperature is given by:

$$\sigma(T) = \left(\frac{C}{T}\right)\exp\left(-\frac{E_a}{kT}\right) \tag{25}$$

where $C$ is a constant, $T$ is the temperature, $E_a$ is the activation energy, and $k$ is the Boltzmann constant. The lichtenecker formula for the conductivity of 0-3 composites is given by:

$$\sigma^{eff} = \left[\sigma^{c}\right]^{\nu}\left[\sigma^{p}\right]^{(1-\nu)} \tag{26}$$

where $\sigma^{eff}$, $\sigma^{c}$, and $\sigma^{p}$ are the conductivities of composite, ceramic and polymer respectively and $\nu$ is the ceramic loading by volume. Combining equations 25 and 26:

$$\left(\frac{C^{eff}}{T}\right)\exp\left(-\frac{E_a^{eff}}{kT}\right) = \left[\left(\frac{C^{c}}{T}\right)\exp\left(-\frac{E_a^{c}}{kT}\right)\right]^{\nu}\left[\left(\frac{C^{p}}{T}\right)\exp\left(-\frac{E_a^{p}}{kT}\right)\right]^{(1-\nu)}$$

where $C^{eff}$ , $C^{c}$ , and $C^{p}$ are constants and $E_a{}^{eff}$, $E_a{}^{c}$, and $E_a{}^{p}$ are the activation energies of hopping for the composite, ceramic, and polymer respectively. Simplifying the above equation:

$$\frac{C^{eff}}{\left[C^{c}\right]^{\nu}\left[C^{p}\right]^{(1-\nu)}}\frac{T^{\nu}T^{(1-\nu)}}{T}\exp\left(-\frac{E_a^{eff}}{kT}\right)=\left[\exp\left(-\frac{E_a^{c}}{kT}\right)\right]^{\nu}\left[\exp\left(-\frac{E_a^{p}}{kT}\right)\right]^{(1-\nu)}$$

$$\frac{C^{eff}}{\left[C^{c}\right]^{\nu}\left[C^{p}\right]^{(1-\nu)}}\exp\left(-\frac{E_a^{eff}}{kT}\right)=\left[\exp\left(-\frac{E_a^{c}}{kT}\right)\right]^{\nu}\left[\exp\left(-\frac{E_a^{p}}{kT}\right)\right]^{(1-\nu)}$$

$$\ln\left[\frac{C^{eff}}{\left[C^{c}\right]^{\nu}\left[C^{p}\right]^{(1-\nu)}}\right]-\frac{E_a^{eff}}{kT}=-\nu\frac{E_a^{c}}{kT}-(1-\nu)\frac{E_a^{p}}{kT}$$

$$E_a^{eff}=\nu E_a^{c}+(1-\nu)E_a^{p}+kT\ln\left[\frac{C^{eff}}{\left[C^{c}\right]^{\nu}\left[C^{p}\right]^{(1-\nu)}}\right]$$

$$when\ \nu=0,\ E_a^{eff}=E_a^{p}\Rightarrow\frac{C^{eff}}{\left[C^{c}\right]^{\nu}\left[C^{p}\right]^{(1-\nu)}}=1,\ as\ kT\neq 0$$

$$E_a^{eff}=\nu E_a^{c}+(1-\nu)E_a^{p} \qquad (27)$$

This implies that the activation energy of hopping mechanism for the composite will decrease linearly with an in increase in the loading of barium titanate as shown in Figure 8-35.

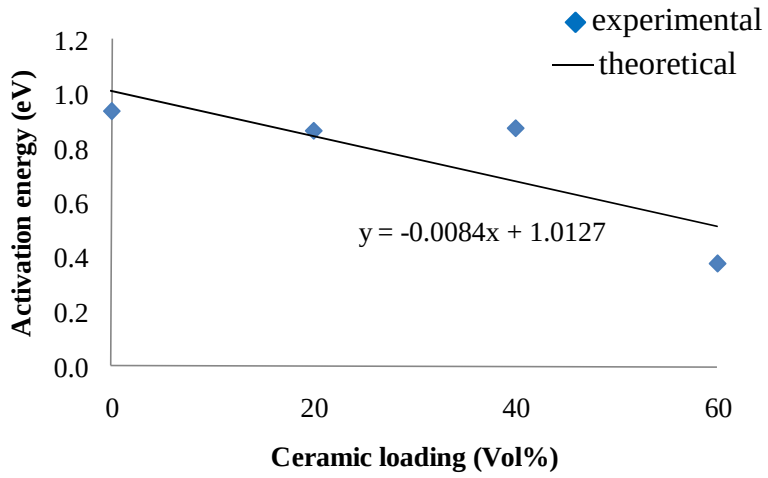


***Figure 8-35.*** *Trend of activation energy as a function of ceramic loading*

It can be seen in Figure 8-35 that all the points do not lie along the theoretical straight line. The activation energy of samples with 20% and 40% ceramic particles was found to be higher than the predicted values (using theoretical models). This can be due to improper mixing in the composite with 20% and 40% ceramic loading.

The manufacturability of the composite with 0% and 60% loading is not challenging since it is pure polymer and polymer fully packed with ceramic particles respectively. There are no issues such as improper mixing or agglomeration in the composite at these loadings. But when the loading of ceramic is 20% and 40%, some phenomenon such as non-uniform distribution, agglomeration and percolation of ceramic particles is also expected to take place. Non-uniform distribution or agglomeration of ceramic particles is expected to increase the activation energy since leakage current will have to travel through packets of pure epoxy. Percolation of ceramic particles is expected to decrease the activation energy since leakage current will get low resistivity path through ceramic particles. However a different phenomenon was observed when samples with 20% and 40% ceramic loading were cross sectioned. The ceramic particles were found to settle down in the direction of gravity and the region of the dielectric at top was almost pure epoxy that acted as a high resistance series path. Because of this phenomenon, samples with 20% and 40% loading of ceramic had higher activation energy as compared to the predicted activation energy from theoretical models. The settling of ceramic particles is expected to be taken during the $150^{o}$ C heating step for 15 minutes. This temperature was high enough to lower the viscosity of the epoxy (leading to sedimentation of ceramic) but not sufficiently high to cure the epoxy.

### 8.5.2 As a function of ceramic particle diameter

It was observed that the conductivity of the composite decreases with a decrease in the diameter of the ceramic particles. This observation can be explained if the path of the leakage current in this composite is analyzed. Since the conductivity of $BaTiO_3$ is higher than epoxy, $BaTiO_3$ acts as a low resistance path to the leakage current. But for the same volume loading if the $BaTiO_3$ particle size is reduced, the number of contacts between adjacent $BaTiO_3$ particles increases as shown in Figure 8-36 [79]. The electrical resistance of the contact is governed by the conductivity of the epoxy matrix. So with an increase in the number of contacts, the conductivity of the composite decreases. It is to be noted that at a microscopic level the conductivity of $BaTiO_3$ is a constant but in a composite its conductivity varies when measured macroscopically.

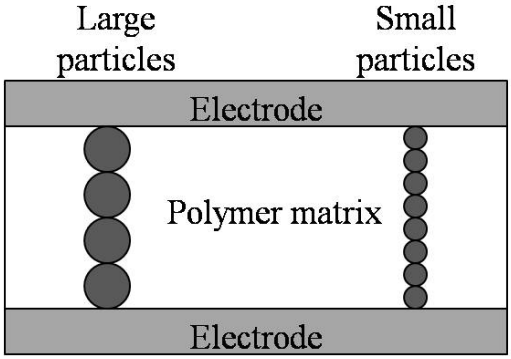


***Figure 8-36.*** *Increase in the number of contacts with a decrease in the particle size (at a constant loading).*

The conductivity of the composite as a function of the ceramic particle diameter at different temperature and voltage is shown in Figure 8-37-Figure 8-40. Some

inconsistencies were observed in the data of the composite with 100 nm ceramic particles. This might be due to increased agglomeration in the 100 nm ceramic particles.

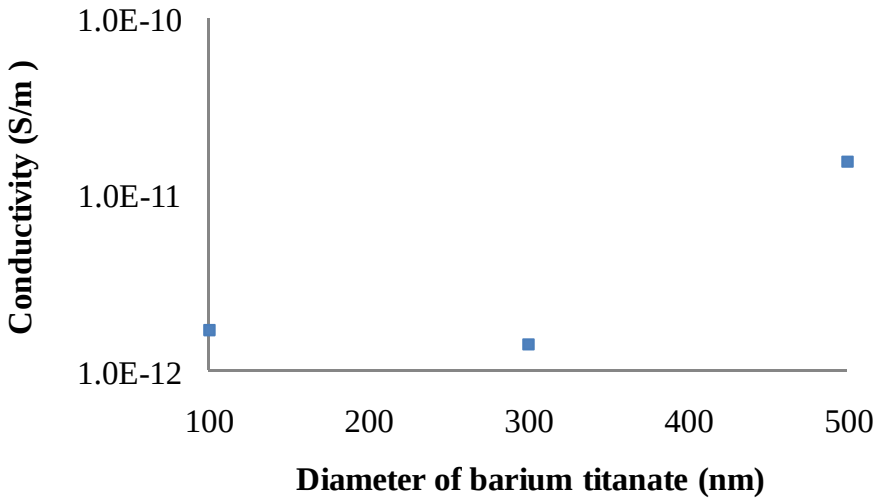


***Figure 8-37.*** *Conductivity of the composite as a function of ceramic diameter (1 V and 25$^{o}$C)*

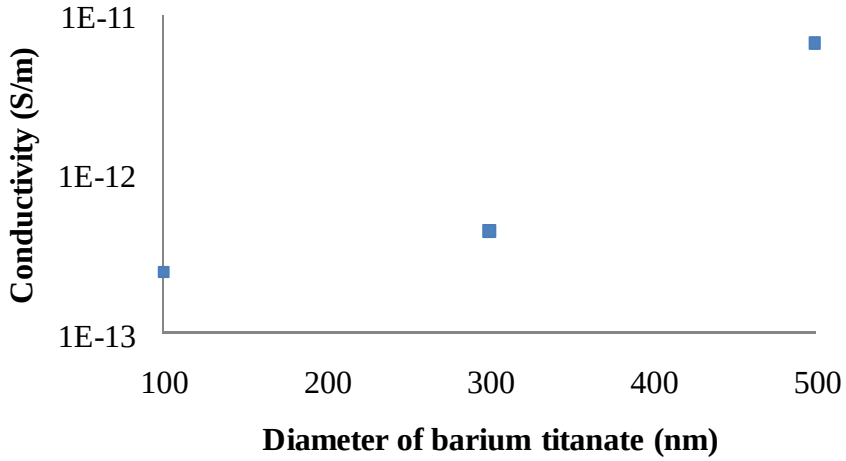


***Figure 8-38.*** *Conductivity of the composite as a function of ceramic diameter (50 V and 25$^{o}$C)*

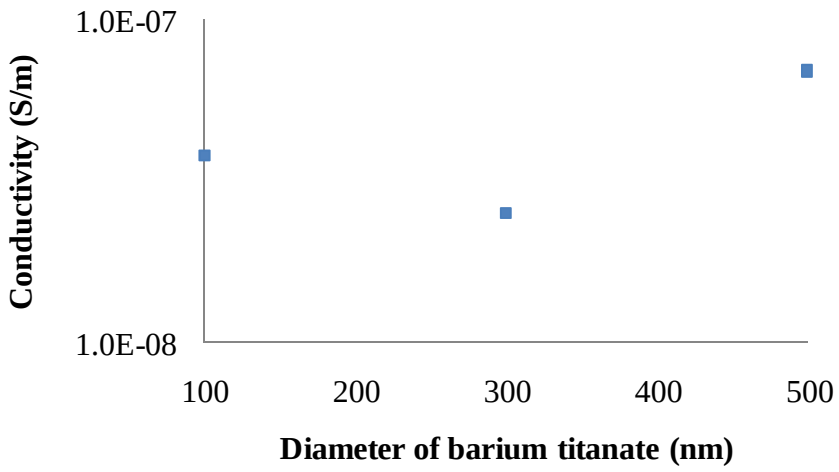


***Figure 8-39.*** *Conductivity of the composite as a function of ceramic diameter (1 V and 125$^{o}$C)*

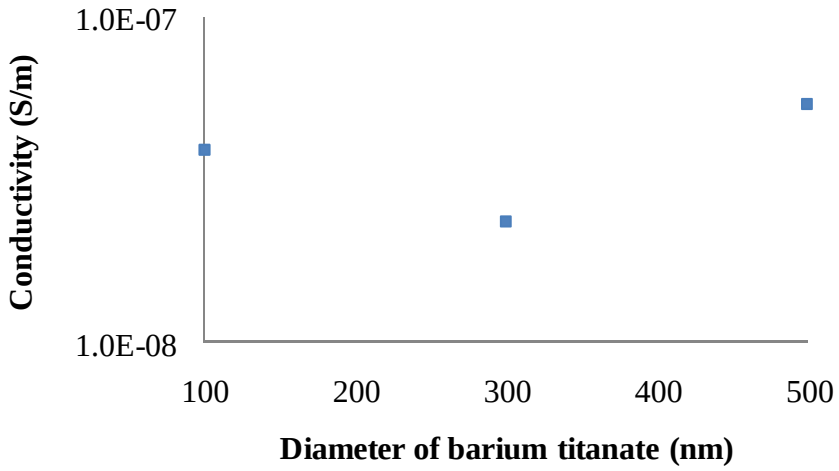


***Figure 8-40.*** *Conductivity of the composite as a function of ceramic diameter (50 V and 125$^{o}$C)*

It is not possible to derive the functional dependence of conductivity on the ceramic diameter using the given data. However in literature it was observed that in a polymer-Ni composite the dependence of conductivity on the filler size was exponential [80]. It is assumed that the exponential behavior will be valid in the current set of

materials also. This behavior can be expressed by the following equation at a constant temperature (T=constant):

$$\sigma(d) = \sigma_o \exp(C_o d) \tag{28}$$

where $\sigma(d)$ is the conductivity, $\sigma_o$ is a constant, $C_o$ is a constant, and $d$ is the diameter of ceramic particles. Comparing equation 25 and 28 at a constant temperature ($T=T_o$):

$$\left(\frac{C}{T_o}\right)\exp\left(-\frac{E_a}{kT_o}\right) = \sigma_o \exp(C_o d)$$

$$\ln\left(\frac{C}{T_o}\right) - \frac{E_a}{kT_o} = \ln\sigma_o + C_o d$$

$$E_a = kT_o\left[\ln\left(\frac{C}{T_o}\right) - \ln\sigma_o - C_o d\right]$$

$$E_a = kT_o\left[\ln\left(\frac{C}{T_o}\right) - \ln\sigma_o\right] - (kT_o C_o)d$$

$$E_a = A - Bd \tag{29}$$

where $A$ and $B$ are constants. This implies that with an increase in the diameter of the ceramic particles, the activation energy of the hopping mechanism will decrease linearly as shown in Figure 8-41.

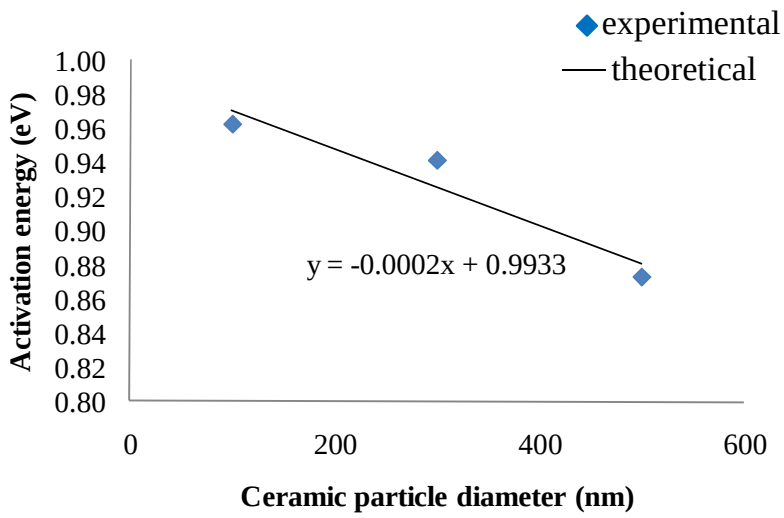


***Figure 8-41.*** *Trend of activation energy as a function of ceramic particle diameter*

## *8.6 Application of the Lichtenecker equation*

The Lichtenecker equation can be used to calculate the conductivity of Barium titanate which can't be measured directly in this composite material. The Lichtenecker equation was used to calculate the conductivity of Barium titan ate (particle diameter = 500nm) as a function of temperature and voltage.

The effect of temperature on the conductivity of epoxy and barium titanate ($d_c$=500 nm) is shown in Figure 8-42 and Figure 8-43 at 1 V and 50 V respectively. It was observed that the conductivity values at 1 V had some fluctuations which may be due to some errors during measurement of low current at lower voltages. Further it was observed that as the temperature was increased the difference in the conductivity values of epoxy and barium titanate reduced. Similar behavior was observed at other voltages also (between 1 V and 50 V).

This implies that addition of a particular volume fraction of Barium titanate will affect the conductivity more at lower temperatures as compared to higher temperatures. This behavior can be seen in the IV plots at 25°C and 125°C (Figure 8-2 and Figure 8-3). At 25°C addition of barium titanate (from 0 to 0.6 volume fraction) at a constant voltage increased the leakage current with an increasing rate. However at 125°C addition of barium titanate (from 0 to 0.6 volume fraction) at a constant voltage increased the leakage current with a decreasing rate.

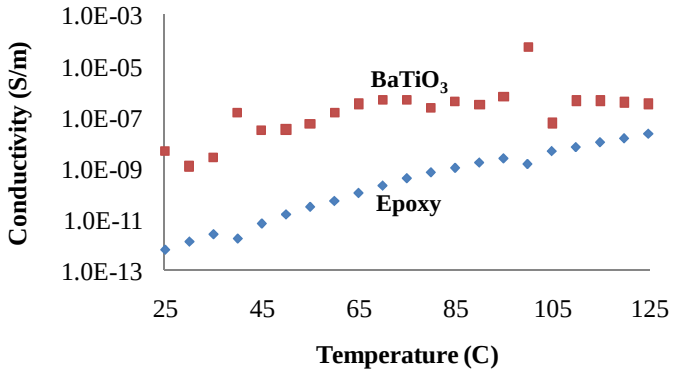


***Figure 8-42.*** *Mean conductivity of epoxy and $BaTiO_3$ (particle diameter=500 nm) as a function of temperature at 1 V.*

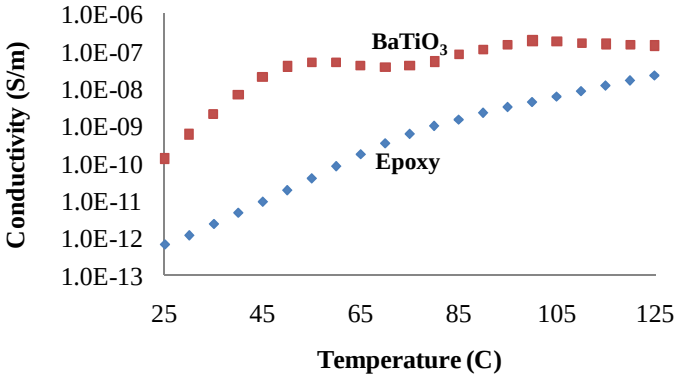


***Figure 8-43.*** *Mean conductivity of epoxy and $BaTiO_3$ (particle diameter=500 nm) as a function of temperature at 50 V.*

The effect of voltage on the conductivity of $BaTiO_3$ ($d_c$=500 nm) is shown in Figure 8-44 and Figure 8-45 at 25°C and 125°C respectively. It was observed that the conductivity of epoxy was almost constant with a change in voltage at both temperatures. But the conductivity of $BaTiO_3$ ($d_c$=500 nm) was found to decrease with an increase in the voltage at both temperatures. Similar behavior was observed at other temperatures also (between 25°C and 125°C).

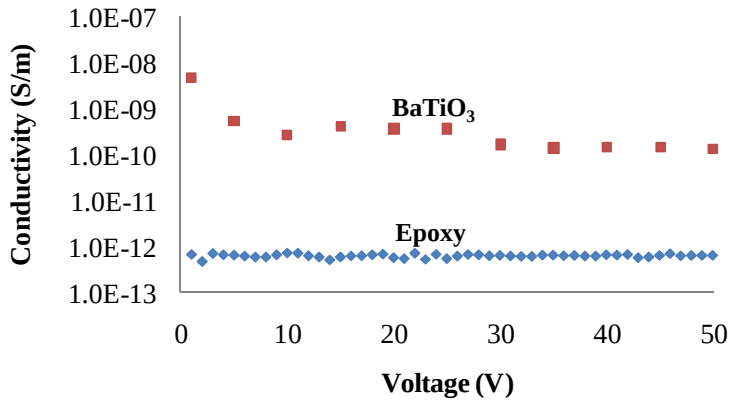


***Figure 8-44.*** *Mean conductivity of epoxy and $BaTiO_3$ (particle diameter=500 nm) as a function of voltage at 25°C.*

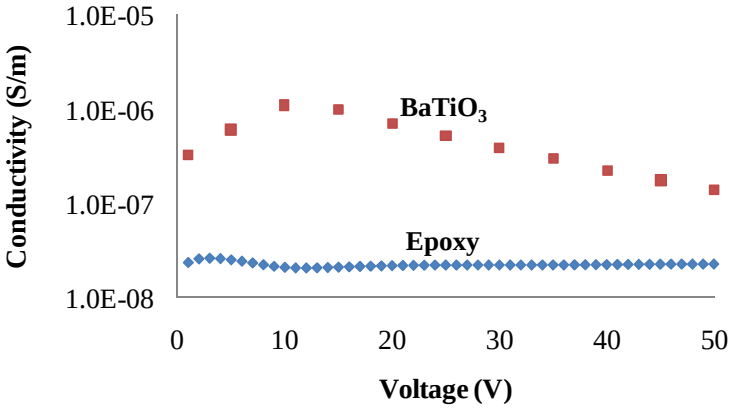


***Figure 8-45.*** *Mean conductivity of epoxy and $BaTiO_3$ (particle diameter=500 nm) as a function of voltage at 125°C.*

A change in the conductivity of $BaTiO_3$ with voltage leads to deviation from Ohmic behavior. This can be seen in the IV plots at 25°C and 125°C (Figure 8-2 and Figure 8-3). It was observed that pure epoxy exhibited an Ohmic behavior however as the loading of $BaTiO_3$ was increased in this composite, deviations from Ohmic behavior were observed. As the resistivity of $BaTiO_3$ increases with an increase in the voltage, the resistivity of the composite also increases. The increase in the resistivity of the composite leads to an increase in the slope of the IV curve as explained in Figure 8-46.

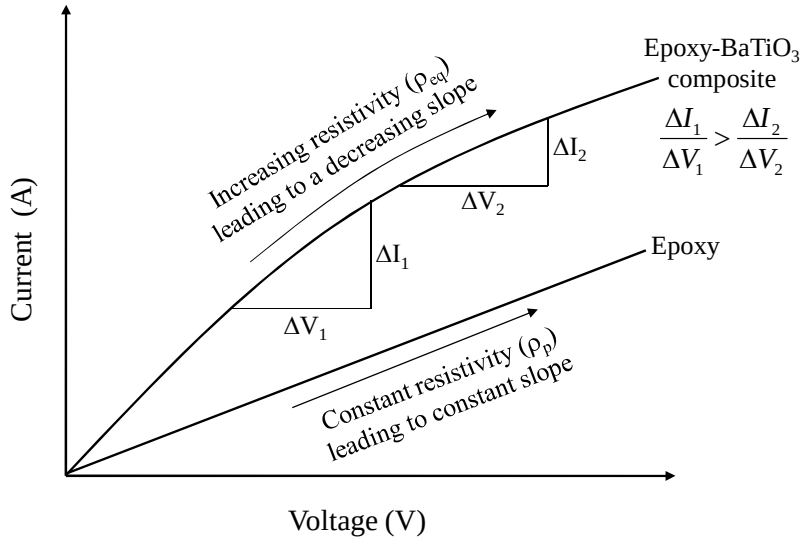


***Figure 8-46.*** *Deviations from Ohmic behavior in the composite.*

# 9. Conclusions

In this work the reliability of embedded planar capacitors has been investigated under temperature-humidity-bias (THB) tests and highly accelerated life tests. Further the mechanism of high leakage current in the epoxy-$BaTiO_3$ composite dielectric of embedded planar capacitors has also been investigated. Since epoxy-$BaTiO_3$ composite dielectric is widely used, this dissertation deals with this dielectric material only.

## *9.1 Temperature humidity bias (THB) tests*

Under THB conditions, the value of capacitance and dissipation factor was observed to increase due to moisture absorption in the dielectric. The average increase in capacitance and dissipation after 2000 hours at 85$^{o}$C and 85% RH was about 20%. The time required for the capacitance and dissipation factor to stabilize under these conditions increased with an increase in the area of the capacitor, since moisture had to diffuse over a greater length of the large capacitor.

Failures as a result of a sharp drop in the insulation resistance were observed in embedded planar capacitors that were biased at 5 V under 85$^{o}$C and 85% RH conditions. These failures seem to have been driven by defects in the dielectric, such as porosity and voids that can favor the formation of a conducting path under THB conditions. The increase in capacitance and dissipation factor were found to be reversible and returned to its pre-THB value within 20 hours after a high temperature bake at 125$^{o}$C. The insulation resistance failures also healed during baking at 125$^{o}$C.

## 9.2 Lifetime modeling

The failure mode during highly accelerated life tests was found to be a sharp increase in the value of leakage current, implying avalanche breakdown and a logarithmic decrease in the value of capacitance. The reason for avalanche breakdown was expected to be due to defects in the dielectric and some wearout degradation taking place in the dielectric. The logarithmic decrease in the capacitance was expected to be due to aging in $BaTiO_3$.

The time-to-failure as a result of avalanche breakdown was modeled using the Prokopowicz model. The values of constants of the Prokopowicz model, $n$ and $E_a$, were found to be 6.55 and 1.11 eV, respectively, for the epoxy-$BaTiO_3$ composite dielectric. Regression analysis was performed to model the logarithmic degradation of capacitance.

## 9.3 Conduction mechanisms in epoxy-$BaTiO_3$ composite dielectric

Embedded capacitors with epoxy-$BaTiO_3$ composite dielectric were fabricated with varying $BaTiO_3$ loading (0% to 60% by volume) and with varying $BaTiO_3$ particle diameter (100 nm to 500 nm). The mechanism of current conduction in all the fabricated dielectric was found to be governed by the hopping mechanism.

The activation energy of the hopping mechanism was found to decrease with an increase in the loading of $BaTiO_3$ particles. This happens because the resistivity of $BaTiO_3$ is lower than epoxy and hence $BaTiO_3$ acts as a low resistance path to the leakage current. The activation energy of hopping decreased with an increase in the

diameter of $BaTiO_3$ particles. This happens because when the particle size is reduced, the number of high resistivity contacts between adjacent $BaTiO_3$ particles increases. Activation energy was found to decrease linearly for both cases.

# 10. Contributions

Embedded planar capacitors have many advantages and will be crucial in next generation electronic circuits for communication, automotive, military, medical, and space applications. This dissertation filled some of the gaps in the existing research on embedded planar capacitors and will aid in wider commercialization of these capacitors. This section presents the contributions to the research community and industry resulting from the advances reported as a part of this dissertation. Since epoxy-$BaTiO_3$ composite dielectric is widely used, this dissertation deals with this dielectric material only.

## *10.1 Temperature humidity bias (THB) tests*

This dissertation investigated the reliability of embedded planar capacitors during temperature-humidity-bias (THB) tests. The failure modes and mechanisms under THB conditions were determined. It was observed that failures as a result of drop in insulation resistance can take place at voltages as low as 5 V under elevated temperature and humidity conditions ($85^oC$ and 85% RH). These failures were expected to be driven by factors such as defects in the dielectric, moisture, ionic contaminants, and a voltage bias that favors the formation of a low resistance leakage path. Further it was observed that the capacitance and dissipation factor increased by almost 20% under these conditions. A methodology was developed using finite element methods to model these drift in electrical parameters. These failures and parametric drifts can affect the system where embedded planar capacitors are used. Hence these capacitors should be protected from moisture while use in humid conditions.

## 10.2 Lifetime modeling

This dissertation investigated the reliability of embedded planar capacitors during highly accelerated life tests. The failure modes and mechanisms were found to be avalanche breakdown of the dielectric and a logarithmic decrease in the value of capacitance. The time-to-failure as a result of avalanche breakdown was modeled using the Prokopowicz model by performing highly accelerated life tests at multiple stress levels. The values of constants of the Prokopowicz model, $n$ and $E_a$, were found to be 6.55 and 1.11 eV respectively. The logarithmic decrease in capacitance was modeled by performing regression of the capacitance data using the aging equation. These failure/degradation models can be used for the qualification of embedded planar capacitors, for the development of new composite dielectric materials, and to improve the manufacturing processes of these capacitors. Further, a novel technique was developed that can be used to analyze the failure site of avalanche breakdown. In this technique similar failures were induced in a healthy capacitor at a predetermined site.

## 10.3 Conduction mechanisms in epoxy-$BaTiO_3$ composite dielectric

This dissertation investigated the mechanism of conduction in the epoxy-$BaTiO_3$ composite dielectric used in embedded planar capacitors. The mechanism of conduction in epoxy-$BaTiO_3$ composites was found to be governed by the hopping mechanism. Further, the functional dependence of leakage current on temperature ($T$), voltage ($V$), $BaTiO_3$ loading ($n$) and $BaTiO_3$ particle diameter ($d_c$) was modeled in these composites.

The functional dependence of the leakage current on these factors can be used in designing new materials with a low value of leakage current.

# 11. Limitations of this Research and Future work

In this section the limitations of this dissertation are discussed. Further possible future work in this area is also discussed.

## *11.1 Temperature humidity bias (THB) tests*

In this work after the THB test the PWB was baked at 125$^{o}$C to drive away the absorbed moisture. Since moisture absorption and desorption is taking place at different temperatures (85$^{o}$C and 125$^{o}$C respectively), temperature can also play a role in the disappearance of insulation resistance failures. It is possible that the conduction path is simply destroyed due to a mismatch in the coefficient of thermal expansion of the conduction path and the dielectric material. In future, the moisture desorption should be performed at the same temperature, in order to eliminate the effect of temperature in the disappearance of these failures. Further, a voltage bias reversal (at the same temperature and humidity) should also be performed after the THB test to see if these failures disappear.

During THB test, the insulation resistance failures were expected to be driven by factors such as defects in the dielectric, moisture, voltage bias, and ionic contaminants that favor the formation of a low resistance leakage path. A quantitative effect of these factors on the time-to-failure can be determined by performing a carefully designed THB test. For this, failure terminated THB test needs to be conducted at multiple stress levels (at least three) for the above factors. The first factor is the number of defects in the dielectric. Selecting a test vehicle with capacitors of different area (with significant population) will simulate capacitors with different number of defect in the dielectric. The

second factor is the absorbed moisture level in the dielectric that can be varied by changing the environmental temperature and the humidity levels.

In the modeling of moisture diffusion in capacitor dielectric, the diffusion of moisture in the FR-4 was ignored in this study to simplify calculations. A more scientific way of modeling diffusion in this structure is by considering the diffusion of moisture in FR-4 also. If we carefully observe the whole process, we see that the diffusion of moisture in the capacitor dielectric is taking place at all times (even before the saturation of FR-4 with moisture). It implies that the boundary condition is not a constant. The concentration of moisture at the boundary is also increasing and getting saturated as the FR-4 is getting saturated with moisture. The diffusion of moisture in this structure with a variable boundary condition is a possible future work direction in this area.

## *11.2 Lifetime modeling*

During highly accelerated life tests, statistical analysis of time-to-failure was performed only on the data of small capacitors. In future, these tests can be performed on embedded planar capacitors with different area to develop an area scaling factor and modify the Prokopowicz model. Further, these tests can also be performed on other commercially available embedded capacitors to compare materials from different manufacturers.

## 11.3 Conduction mechanisms in epoxy-$BaTiO_3$ composite dielectric

It was observed that the actual value of activation energy of the leakage current did not match the theoretical values in the region of intermediate loading, i.e. 20% and 40% by volume. This was attributed to various reasons such as non-uniform distribution and agglomeration of ceramic particles at these loading. Because of this we cannot use the theoretical models to predict the activation energy accurately.

After investigating the mechanism of conduction in epoxy-$BaTiO_3$ composites, it was observed that $BaTiO_3$ acts as a low resistance path for the leakage current. The bulk polymer matrix and contacts between adjacent $BaTiO_3$ particles act as resistance to the leakage current. Very small sized $BaTiO_3$ particles (<100 nm) should not be used to lower the leakage current due to problems of agglomeration and low dielectric constant. Another approach that can be explored in future is the surface modification of $BaTiO_3$ particles which includes coating it with a material of high resistivity. Capacitor with epoxy-$BaTiO_3$ composite dielectric can be fabricated with different surface modifications of $BaTiO_3$ followed by the measurements of leakage current.

# 12. References


[1]. Y. Rao, J. Yue, and C. Wong, "Material Characterization of High Dielectric Constant Polymer-Ceramic Composite for Embedded Capacitor to RF Application," *Journal of Applied Polymer Science*, pp. 2228 – 2231, Vol. 92, Issue 4, 2004.

[2]. J. Rector, J. Dougherty, V. Brown, J. Galvagni, and J. Prymak, "Integrated and Integral Passive Components: A Technology Roadmap", *Electronic Components and Technology Conference*, pp. 713-723, San Jose, CA, 1997.

[3]. M. A. Alam, M. H. Azarian, M. Osterman, and M. Pecht, "Effectiveness of Embedded Capacitors in Reducing the Number of Surface Mount Capacitors for Decoupling Applications," *Circuit World*, Vol. 36, Issue 1, 2010.

[4]. A. Madou and L. Martens, "Electrical Behavior of Decoupling Capacitors Embedded in Multilayered PCBs", *IEEE Transactions on Electromagnetic Compatibility*, pp. 549-556, Vol. 43, No. 4, 2001.

[5]. J. Peiffer, "Using Embedded Capacitance to Improve Electrical Performance and Reduce Board Size in High Speed Digital and RF Applications", *IPC Printed Circuits Expo*, Los Angeles, CA, 2007.

[6]. P. Muthana, A. Engin, M. Swaminathan, R. Tummala, V. Sundaram, B. Wiedenman, D. Amey, K. Dietz, and S. Banerji, "Design, Modeling and Characterization of Embedded Capacitor Networks for Core Decoupling in the Package", *IEEE Transactions on Advanced Packaging*, pp. 809-822, Vol. 30, Issue 4, 2007.

[7]. G. Lei, R. Techentin, and B. Gilbert, “High-Frequency Characterization of Power/Ground-Plane Structures”, *IEEE Transactions on Microwave Theory and Techniques*, pp. 562-569, Vol. 47, No. 5, 1999.

[8]. R. Ulrich and L. Schaper, Integrated Passive Component Technology, Wiley- IEEE Press, 2003.

[9]. Swartz, “Topics in Electronic Ceramics,” *IEEE Transactions on Electrical Insulation*, pp. 935-987, Vol. 25, No. 5, 1990.

[10]. M. Keimasi, M. H. Azarian, and M. Pecht, “Flex Cracking of Multilayer Ceramic Capacitors Assembled with Pb-Free and Tin-Lead Solders”, *IEEE Transactions on Device and Materials Reliability*, Vol. 8, No. 1, 2008.

[11]. J. Xu, S. Bhattacharya, P. Pramanik, and C. Wong, “High Dielectric Constant Polymer-Ceramic (Epoxy-Varnish-Barium Titanate) Nanocomposites at Moderate Filler Loadings for Embedded Capacitors,” *Journal of Electronic Materials*, pp. 2009-2015, Vol. 35, No. 11, 2006.

[12]. S. Wada, T. Hoshina, H. Yasuno, S. Nam, H. Kakemoto, T. Tsurumi, and M. Yashima, “Size Dependence of Dielectric Properties for nm-Sized Barium Titanate Crystallites and its Origin,” *Journal of Korean Physical Society*, pp. 303-307, Vol. 46, No. 1, 2005.

[13]. Y. Chiang, D. Birnie II and W. Kingery, Physical Ceramics-Principles for Ceramic Science and Engineering, John Wiley and Sons, 1997.

[14]. D. Yoon, J. Zhang, and B. Lee, “Dielectric Constant and Mixing Model of $BaTiO_3$ Composite Thick Films”, *Materials Research Bulletin*, pp. 765-772, Vol. 38, 2003.

[15]. Y. Rao, J. Qu, T. Marinis, and C. Wong, "A Precise Numerical Prediction of Effective Dielectric Constant for Polymer-Ceramic Composite based on Effective-Medium Theory", *IEEE Transactions on Components and Packaging Technologies*, pp. 680-683, Vol. 23, No. 4, 2000.

[16]. J. Xu, S. Bhattacharya, K. Moon, J. Lu, B. Englert, and C. Wong, "Large-Area processable High K Nanocomposite-Based Embedded Capacitors", *Electronic Components and Technology Conference*, pp. 1520-1532, San Diego, CA, 2006.

[17]. N. Jayasundere and B. Smith, "Dielectric Constant of Binary Piezo-electric 0-3 Composites", *Journal of Applied Physics*, pp. 2462-2466, Vol. 73, 1993.

[18]. K. Paik, J. Hyun, S. Lee, and K. Jang, "Epoxy/$BaTiO_3$ ($SrTiO_3$) Composite Films and Pastes for High Dielectric Constant and Low Tolerance Embedded Capacitors in Organic Substrates," *Electronics System Integration Technology Conference*, pp. 794-801, Vol. 2, 2006. Dresden, Germany.

[19]. J. Peiffer, "The History of Embedded Distributed Capacitance", *Printed Circuit Design and Manufacture*, pp. 32-37, August, 2004.

[20]. J. Savic, R. Croswell, A. Tungare, G. Dunn, T. Tang, R. Lempkowski, M. Zhang, and T. Lee, "Embedded Passives Technology Implementation in RF Applications", *IPC Printed Circuits Expo*, Long Beach, CA, 2002.

[21]. T. Kamgaing, K. Ichikawa, X. Zeng, K. Hwang, Y. Min, and J. Kubota, "Future Package technologies for Wireless Communication Systems", *Intel Technology Journal*, pp. 353-364, Vol. 9, Issue 4, 2005.

[22]. C. Weng, P. Wei, C. Wu, C. Chen, U. Jow, and Y. Lai, "Embedded Passives Technology for Bluetooth Application in Multi-layer Printed Wiring Board (PWB)", *Electronic Components and technology Conference*, pp. 1124-1128, Las Vegas, NV, 2004.

[23]. W. Jillek and W. Yung, "Embedded Components in Printed Circuit Boards: A Processing Technology Review", *International Journal of Advanced Manufacturing Technology*, pp. 350-360, Vol. 25, 2005.

[24]. C. Zou, J. Fothergill, and S. Rowe, "The Effect of Water Absorption on the Dielectric Properties of Epoxy Nanocomposites," *IEEE Transactions on Dielectrics and Electrical Insulation*, pp. 106-117, Vol. 15, No. 1, 2008.

[25]. C. Zou, J. Fothergill, ans S. Rowe, "A Water Shell Model for the Dielectric Properties of Hydrated Silica-Filled Epoxy Nano-Composites," *International Conference on Solid Dielectrics*, pp. 389-392, Winchester, UK, 2007.

[26]. S. Simamoto, Y. Sakata, J. Kojima, N. Kume, and Y. Tsujimoto, "Lacquered Polymer-Ceramic Composite Dielectric Film for Capacitors," *IEEE International Symposium on Electrical Insulation*, pp. 140-143, Baltimore, MD, 1992.

[27]. H. Windlass, P. Raj, D. Balaraman, S. Bhattacharya, and R. Tummala, "Colloidal Processing of Polymeric Ceramic Nanocomposite Integral Capacitors," *IEEE Transactions on Electronics Packaging Manufacturing*, pp. 100-105, Vol. 26, No. 2, 2003.

[28]. J. Andresakis, T. Yamamoto, and N. Biunno, "New Non-Reinforced Substrates for use as Embedded Capacitors," *Circuit World*, pp. 36-41, Vol. 30, Issue 1, 2003.

[29]. T. Prokopowicz and A. Vaskas, “Research and Development, Intrinsic Reliability, Subminiature Ceramic Capacitors,” Final Report, ECOM-90705-F, pp. 175, NTIS AD-864068, 1969.

[30]. K. Paik, S. Cho, and J. Hyun, “Novel Epoxy/$BaTiO_3$ Composite Embedded Capacitor Films Embedded in Organic Substrates”, *IEEE International Conference on Asian Green Electronics*, pp. 68-73, 2004.

[31]. K. Lee, S. Bhattacharya, M. Varadarajan, L. Wan, I. Abothu, V. Sundaram, P. Muthana, D. Balaraman, P. Raj, M. Swaminathan, S. Sitaram, R. Tummala, P. Viswanadham, S. Dunford, and J. Lauffer, “Design, Fabrication, and Reliability Assessment of Embedded Resistors and Capacitors on Multilayered Organic Substrates”, *International Symposium on Advanced Packaging Materials: Processes, Properties and Interfaces*, pp. 249-254, Irvine, CA, 2005.

[32]. R. Das, M. Poliks, J. Lauffer, and V. Markovich, “High Capacitance, Large Area, Thin film, Nanocomposite Based Embedded Capacitors”, *Electronic Components and Technology Conference*, pp. 1510-1515, San Diego, California, USA, 2006.

[33]. S. Lee, J. Hyun, J. Pak, H. Lee, H. Jeon, and K. Paik, “Fabrication and Characterization of Embedded Capacitors in Printed Circuit Boards Using B-Stage Epoxy/$BaTiO_3$ Composite Embedded Capacitor Films (ECFs)”, *Electronic Components and Technology Conference*, pp. 742-746, Lake Buena Vista, Florida, USA, 2008.

[34]. C. Park, B. Han, and H. Bair, “Humidity Effects on Adhesion Strength between Solder ball and Epoxy Underfills”, *Polymer*, pp. 3811-3818, Vol. 38, 1997.

[35]. S. Lee, J. Jang, W. Lee, and K. Paik, "Reliability Enhancement of Embedded Capacitors in Printed Circuit Boards using B-Stage Epoxy/ $BaTiO_3$ Composite Embedded Capacitor Films (ECFs)", *Electronic Components and Technology Conference*, pp. 771-776, San Diego, CA, 2009.

[36]. K. Jang and K. Paik, "Screen Printable Epoxy/$BaTiO_3$ Embedded Capacitor Pastes with High Dielectric Constant for Organic Substrate Applications," *Journal of Applied Polymer Science*, pp. 798-807, Vol. 110, 2008.

[37]. R. Gerke and D. Ator, "Embedded Resistors and Capacitors in Organic and Inorganic Substrates", *IEEE Aerospace Conference*, Big Sky, MT, 2006.

[38]. M. Pecht, L. Nguyen, and E. Hakim, Plastic Encapsulated Microelectronics, John Wiley & Sons, New York, NY, 1994.

[39]. J. Xu, K. Moon, P. Pramanik, S. Bhattacharya, and C. Wong, "Optimization of Epoxy-Barium Titanate Nanocomposites for High Performance Embedded Capacitor Components," *IEEE Transactions on Components and Packaging Technologies*, pp. 248-253, Vol. 30, No. 2, 2007.

[40]. W. Mason, "Ageing of the Properties of Barium Titanate and Related Ferroelectric Ceramics", *The Journal of the Acoustical Society of America*, pp. 73-85, Vol. 27, No. 1, 1955.

[41]. D. Donahoe, M. Pecht, I. Lloyd, and S. Ganesan, "Moisture Induced Degradation of Multilayer Ceramic Capacitors", *Microelectronics Reliability*, pp. 400-408, Vol. 46, 2006.

[42]. L. Mitoseriu, V. Tura, M. Curteanu, D. Popovici, and A. Anghel, "Aging Effects in Pure and Doped Barium Titanate Ceramics", *IEEE Transactions on Dielectrics and Electrical Insulation*, pp. 500-506, Vol. 8, No. 3, 2001.

[43]. H. Cho, S. Cho, J. Jo, H. Seo, B. Kim, and J. Yoo, "Highly Reliable Processes for Embedding Discrete Passive Components into Organic Substrates", *Microelectronics Reliability*, pp. 739-743, Vol. 48, Issue 5, 2008.

[44]. K. Jang and K. Paik, "A Study on Epoxy/$BaTiO_3$ Embedded Capacitor Pastes for Organic Substrates," *Electronic Components and Technology Conference*, pp. 1504-1509, 2006, San Diego, CA.

[45]. H. Lee and L. Burton," Charge Carriers and Time Dependent Currents in $BaTiO_3$-Based Ceramic," *IEEE Transactions on Components, Hybrids, and Manufacturing Technology*, pp. 469-474, Vol. CHMT-9, No.4, 1986.

[46]. B. Rawal and N. Chan, "Conduction and Failure Mechanisms in Barium Titanate Based Ceramics under Highly Accelerated Conditions," AVX Technical Report, Myrtle Beach, SC.

[47]. W. Minford, "Accelerated Life Testing and Reliability of High K Multilayer Ceramic Capacitors," *IEEE Transactions on Components, Hybrids, and Manufacturing Technology*, pp. 297-300, Vol. CHMT-5, No. 3, 1982.

[48]. J. Paulsen and E. Reed, "Highly Accelerated Life Testing of Base-Metal-Electrode Ceramic Chip Capacitors," *Microelectronics Reliability*, pp. 815-520, Vol. 42, 2002.

[49]. G. Maher, T. Prokopowicz, and V. Bheemineni, “High Volumetric Capacitance Low Fired X7R MLC Capacitor,” *Electronics Components and Technology Conference*, pp. 280-284, Orlando, FL, 1993.

[50]. M Randall, A Gaurav, D Skamser, and J Beeson, “Lifetime Modeling of Sub 2 Micron Dielectric Thickness BME MLCC,” *Capacitor and Resistor Technology Symposium*, Scottsdale, AZ, 2003

[51]. H. Kishi, Y. Mizuno, and H. Chazono, “Base-Metal Electrode-Multilayer Ceramic Capacitors: Past, Present and Future Perspectives,” *Japanese Journal of Applied Physics*, pp. 1-15, Vol. 42, No. 1, 2003.

[52]. H. Lee, K. Lee, J. Schunke, and L. Burton, “Leakage Currents in Multilayer Ceramic Capacitors,” *IEEE Transactions on Components, Hybrid and Manufacturing Technology*, pp. 443-453, Vol. CHMT-7, No. 4, 1984.

[53]. I. Yoo, L. Burton, and F. Stephenson, “Electrical Conduction Mechanisms of Barium-Titanate-Based Thick-Film Capacitors,” *IEEE Transactions on Components, Hybrids, and Manufacturing Technology*, pp. 274-282, Vol. CHMT-10, No. 2, 1987.

[54]. R. Bartnikas and R. Eichhorn, *Engineering Dielectrics-Volume II A,* ASTM Special Technical Publication, Philadelphia, PA, 1983.

[55]. N. Andonovska, S. Rendevski, and S. Prendzov, “Temperature Dependence of Electrical Conductivity of Polyvinyl Chloride-Barium Titanate Composite,” *Bulletin of the Chemists and Technologists of Macedonia*, pp. 17-22, Vol. 21, No. 1, 2002.

[56]. J. Robertson and B. Varlow, "The DC Conductivity Characteristics of Barium Titanate Filled Acrylic Resin," *Annual Report Conference on Electrical Insulation and Dielectric Phenomenon*," pp. 79-83, Albuquerque, NM, 2003.

[57]. S. Ogitani, S. Allen, and P. Kohl, "Factors Influencing the Permittivity of Polymer/Ceramic Composites for Embedded Capacitors", *IEEE Transactions on Advanced Packaging*, pp. 313-322, Vol. 23, No. 2, 2000.

[58]. V. Agrawal, P. Chahal, R. Tummala, and M. Allen, "Improvements and Recent Advances in Nanocomposite Capacitors using a Colloidal Technique", *Electronics Component and Technology Conference*, pp. 165-170, Seattle, WA, 1998.

[59]. L. Fan, Y. Rao, C. Tison, K. Moon, S. Pothukuchi, and C. Wong, "Use of Dispersant in High K Polymer-Ceramic Nano-Composite to Improve Manufacturability and Performance of Integral Capacitors", *Electronic Components and Technology Conference*, pp. 936-940, San Diego, CA, 2002.

[60]. H. Windlass, P. Raj, D. Balaraman, S. Bhattacharya, and R. Tummala, "Colloidal Processing of Polymeric Ceramic Nanocomposite Integral Capacitors", *IEEE Transactions on Electronics Packaging Manufacturing*, pp. 100-105, Vol. 26, No. 2, 2003.

[61]. L. Chu, K. Prakash, M. Tsai, and I. Lin, "Dispersion of Nano-Sized $BaTiO_3$ Powders in Nonaqueous Suspension with Phosphate Ester and their Applications for MLCC", *Journal of European Ceramic Society*, pp. 1205-1212, Vol. 28, 2008.

[62]. U. Paik, V. Hackley, S. Choi, and Y. Jung, "The Effect of Electrostatic Repulsive Forces on the Stability of $BaTiO_3$ Particles Suspended in Non-Aqueous Media",

*Colloids and Surfaces A: Physicochemical and Engineering Aspects*, pp. 77-88, Vol. 135, 1998.

[63]. L. Fan, Y. Rao, C. Tison, K. Moon, S. Pothukuchi, and C. Wong, "Processability and Performance Enhancement of High K Polymer-Ceramic Nano-Composites", *International Symposium on Advanced Packaging Materials*, pp. 120-126, Stone Mountain, GA, 2002.

[64]. K. Paik, J. Hyun, and K. Jang, "Epoxy/$BaTiO_3$ Composite Films and Pastes for High Dielectric Constant and Low Tolerance Embedded Capacitors Fabrication in Organic Substrates", *IEEE Transactions on Electronics Packaging Manufacturing*, pp. 297-303, Vol. 28, No. 4, 2005.

[65]. P. Bowles and R. Charbonneau, "An overview of the NCMS/StorageTek embedded decoupling capacitance project," *International Symposium on Advanced Packaging Materials: Process, Properties, and Interfaces*, pp. 191-196, Braselton, GA, 1999.

[66]. S. Lee, J. Hyun, H. Kim, K. Paik, "A Study on Dielectric Constants of Epoxy/$SrTiO_3$ Composite for Embedded Capacitor Films (ECFs)," *IEEE Transactions on Advanced Packaging*, pp. 428-433, Vol. 30, No.3, 2007.

[67]. M. Leonard and A. Safari, "Crystallite and Grain Size Effects in $BaTiO_3$," *IEEE International Symposium on Applications of Ferroelectrics*, pp. 1003-1005, Vol. 2, East Brunswick, NJ, 1996.

[68]. M. Pecht, H. Ardebili, A. Shukla, J. Hagge, and D. Jennings, "Moisture Ingress into Organic Laminates", *IEEE Transactions on Components and Packaging Technologies*,, pp. 104-110, Vol.22, No.1, 1999.

[69]. M. A. Alam, M. H. Azarian, M. Osterman, and M. Pecht, "Reliability of Embedded Planar Capacitors under Temperature and Voltage Stress", *Capacitor and Resistor Technology Symposium (CARTS)*, Jacksonville, FL, 2009.

[70]. M. Roy, J. Nelson, R. MacCrone, L. Schadler, C. Reed, R. Keefe, and W. Zenger, "Polymer Nanocomposite Dielectrics-The Role of the Interface," *IEEE Transactions on Dielectrics and Electrical Insulation*, pp. 629-643, Vol. 12, No. 4, 2005.

[71]. M. A. Alam, M. H. Azarian, M. Osterman and M. Pecht, "Effect of Environmental Stress and Bias Conditions on Reliability of Embedded Planar Capacitors", *IPC Apex Expo*, Las Vegas, NV, 2010.

[72]. M. A. Alam, M. H. Azarian, M. Osterman, and M. Pecht, "Early Detection of Avalanche Breakdown in Embedded Planar Capacitors using SPRT", *Machinery Failure and Prevention Technology*, Virginia Beach, VA, 2011.

[73]. M. A. Alam, M. H. Azarian, M. Osterman, and M. Pecht, "Prognostics of Embedded Capacitors under Temperature and Voltage Aging", *ASME Conference on Smart Materials, Adaptive Structures and Intelligent Systems*, Philadelphia, PA, 2010.

[74]. M. A. Alam, M. H. Azarian, M. Osterman, and M. Pecht, "Failure Mechanisms in Embedded Planar Capacitors during High Temperature Operating Life (HTOL) Testing", *IPC Apex Expo*, Las Vegas, NV, 2011.

[75]. M. A. Alam, M. H. Azarian, M. Osterman, and M. Pecht, "Temperature and Voltage Stress Effects on Leakage Current Mechanism in Epoxy-Barium Titanate Composite Dielectric Used in Embedded Capacitors", *Microelectronics Reliability*, pp. 946-952, Vol. 51, Issue 5, 2011.

[76]. M. Ieda, “Electrical Conduction and Carrier Traps in Polymeric Materials,” *IEEE Transactions on Electrical Insulation*, pp. 162-178, Vol. EI-19, No. 3, 1984.

[77]. Y. Chiang, D. Birnie II, and W. Kingery, Physical Ceramics-Principles for Ceramic Science and Engineering, John Wiley and Sons, 1997.

[78]. N. Uvarov, “Estimation of Composites Conductivity using a General Mixing Rule”, *Solid State Ionics*, pp. 1267-1272, Vol. 136-137, 2000.

[79]. S. Cho, J. Lee, and K. Paik, “Effects of Particle Size on Dielectric Constant and Leakage Current of Epoxy/Barium Titanate ($BaTiO_3$) Composite Films for Embedded Capacitors”, *International Symposium on Electronic Materials and Packaging*, pp. 63-68, Jeju Island, 2001.

[80]. H. Vladimir and L. Karel, “New Mixing Rule of Polymer Composite Systems”, *WSEAS Transactions on Electronics*, pp. 181-185, Vol. 4, Issue 9, 2007.